Studying Polar cusp dynamics: future plans at KHO

John Meriwether
Matt Cooper
Andrew Gerrard

Seminar 13 October 2022

New Jersey Institute of Technology

Many collaborators over the years.

Will talk generally about 15 cm FPI (HODI) results obtained at JJO in July, August, and September 2022 and then pivot to discuss future collaborative plans for 2022-2023 winter at KHO working with Anasuya Aruliah, Mike Kosch, and Ian McWhirter.

Had intended a few introductory slides regarding the aeronomy of the polar cusp to go here but to avoid going on too long, I will move these slides to the end of the presentation. They will be available for review if we have time at the end of the talk.

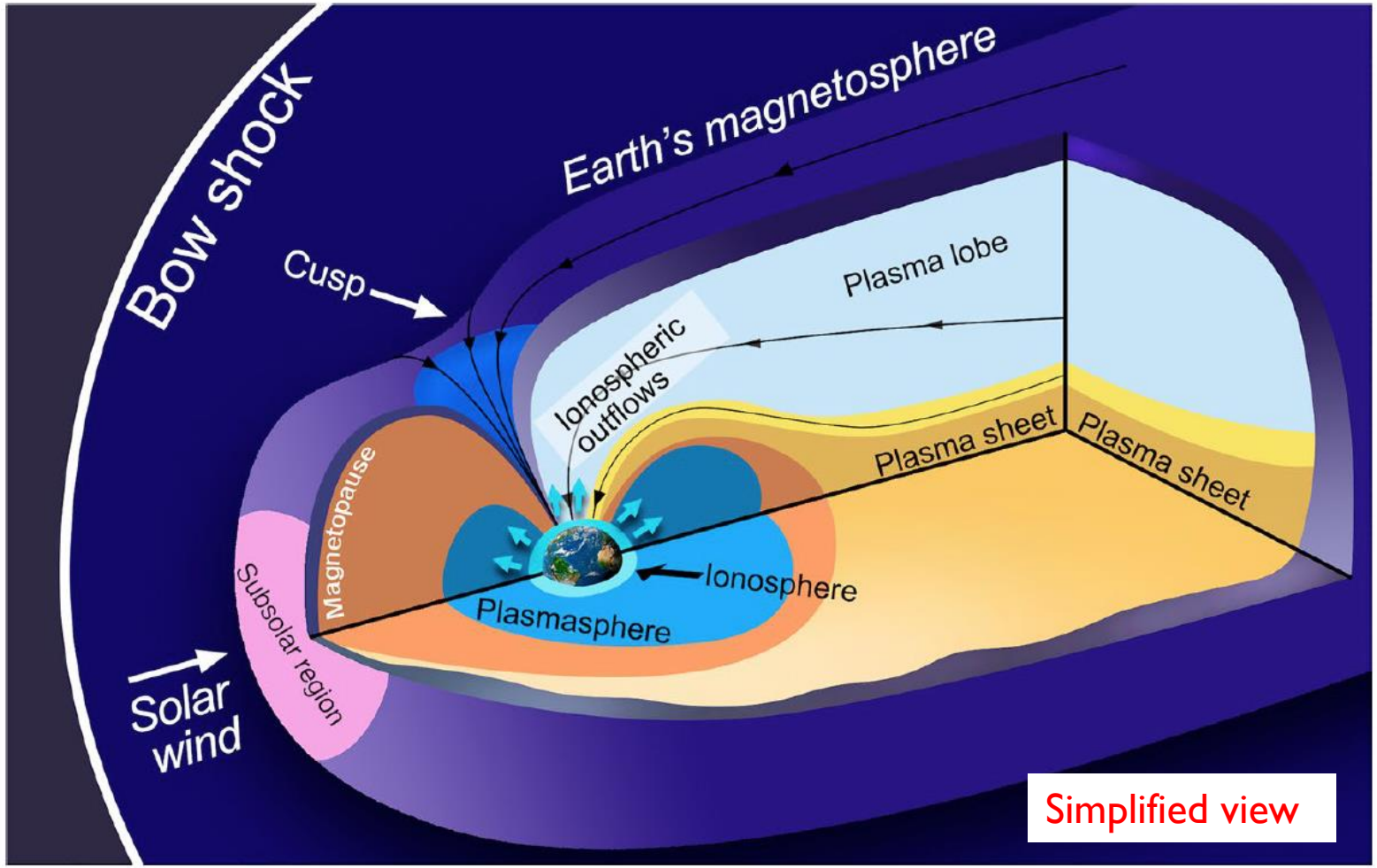

Figure 1. Main regions of the Earth's magnetosphere. Ionospheric ions are continuously escaping along magnetic field lines, and end up in different magnetospheric regions depending on their initial geomagnetic location. Credit: J. M. Domínguez, adapted from Pollock et al. (2003).

Where is the polar cusp?

Obviously, in the polar region but this is more specific in the sense of a particular latitude where the soft particle flux of the solar wind plasma has a direct access to the Earth's ionosphere along the geomagnetic field lines.

Alternative name of "cleft"

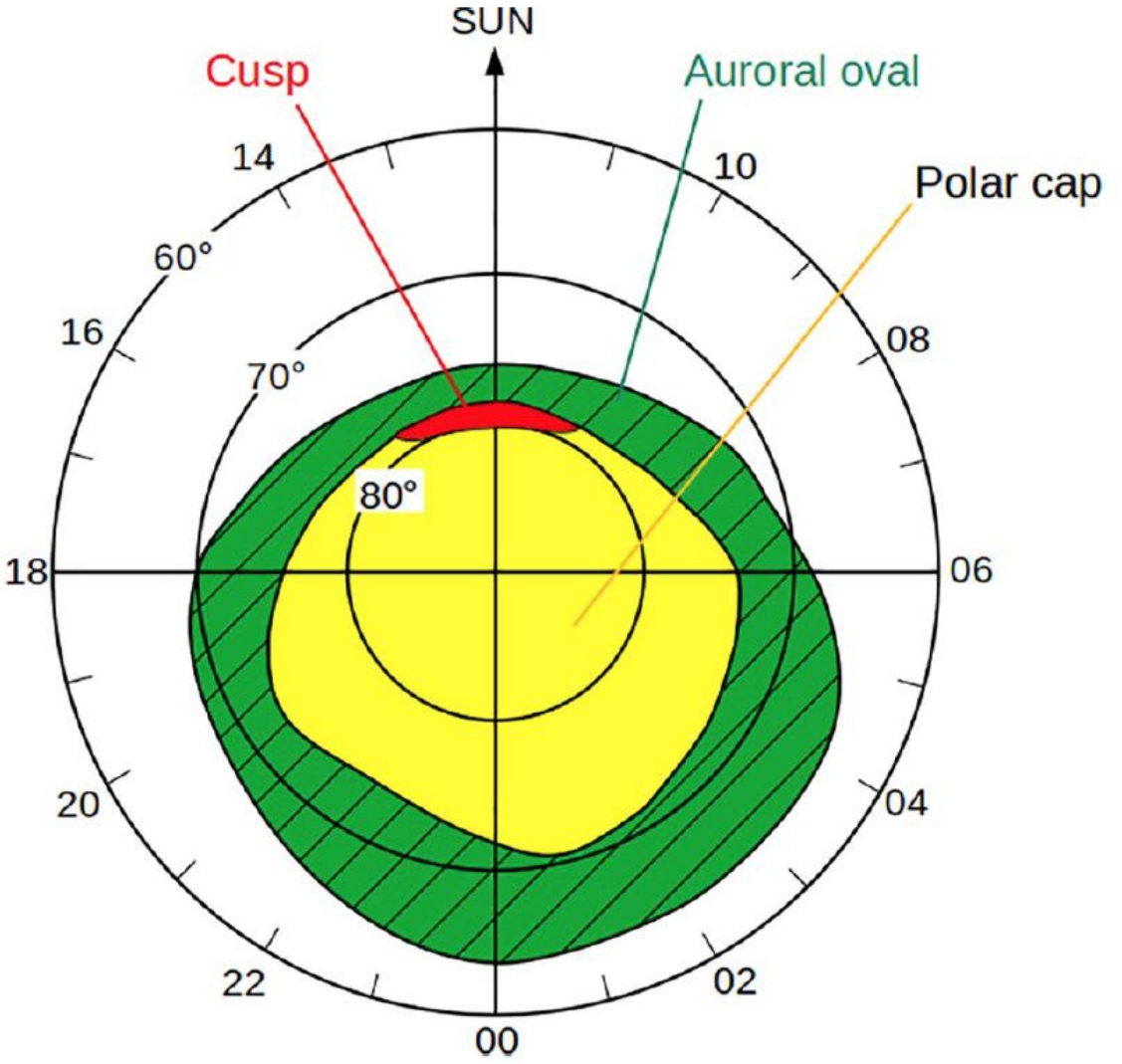

Figure 2. Top view of the Earth's ionosphere in geomagnetic latitude and local magnetic time coordinates, indicating typical locations of the auroral oval (green color), the cusp (red) and the polar cap (yellow). Poleward of the auroral oval, magnetic field lines are open, with the polar cap mapping to the tail lobes, and the cusp mapping to the dayside. Adapted from Akasofu (2015).

Soft particle precipitation generates cusp aurora characterized by enhanced 630 nm emission

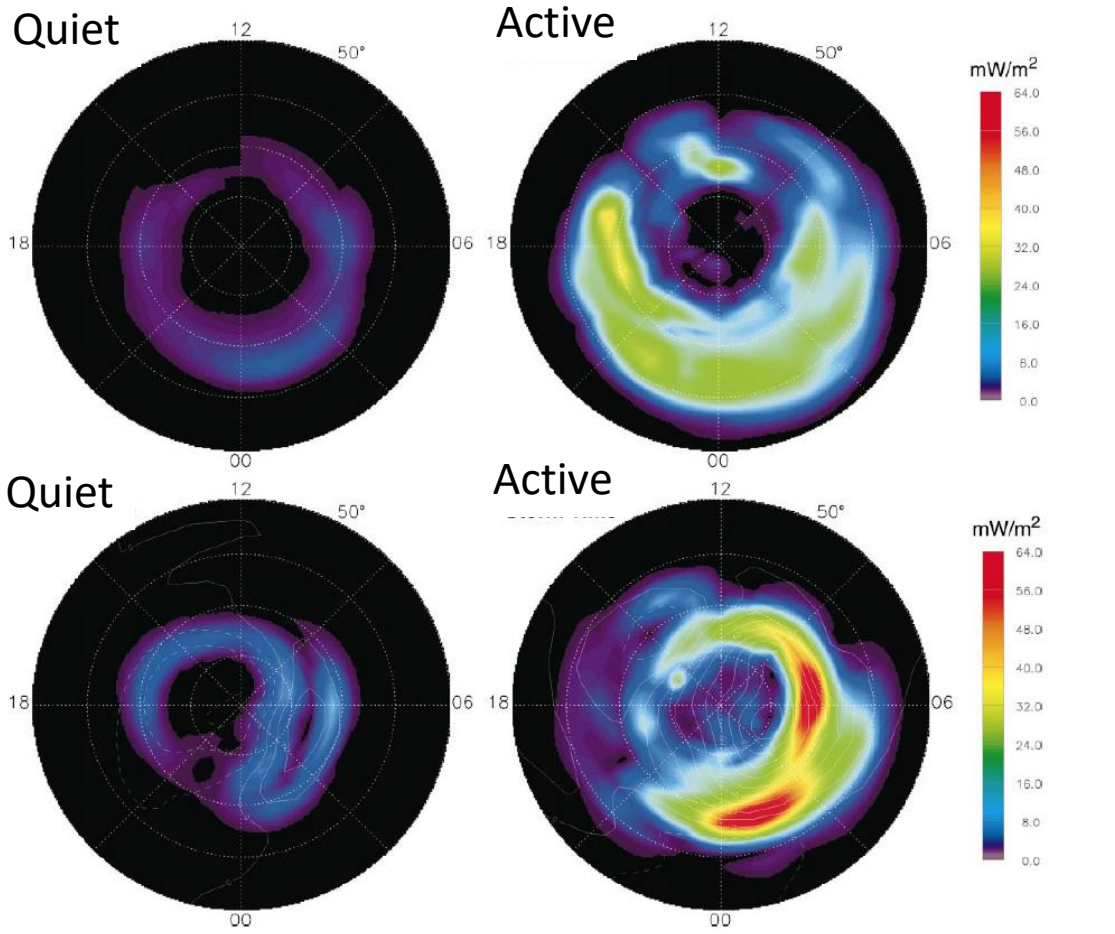

Fig. 3. Distributions in magnetic latitude and magnetic local time of the estimated auroral electron energy flux (top), the height-integrated Joule heating rate (bottom, colors), and the electric potential (bottom, overlain contours) above 50° magnetic latitude in the northern hemisphere for two times on 1997 January 10: 0255 UT (left), a quiet period, and 1105 UT (right), an active time. The electric-potential contour interval is 10 kV.

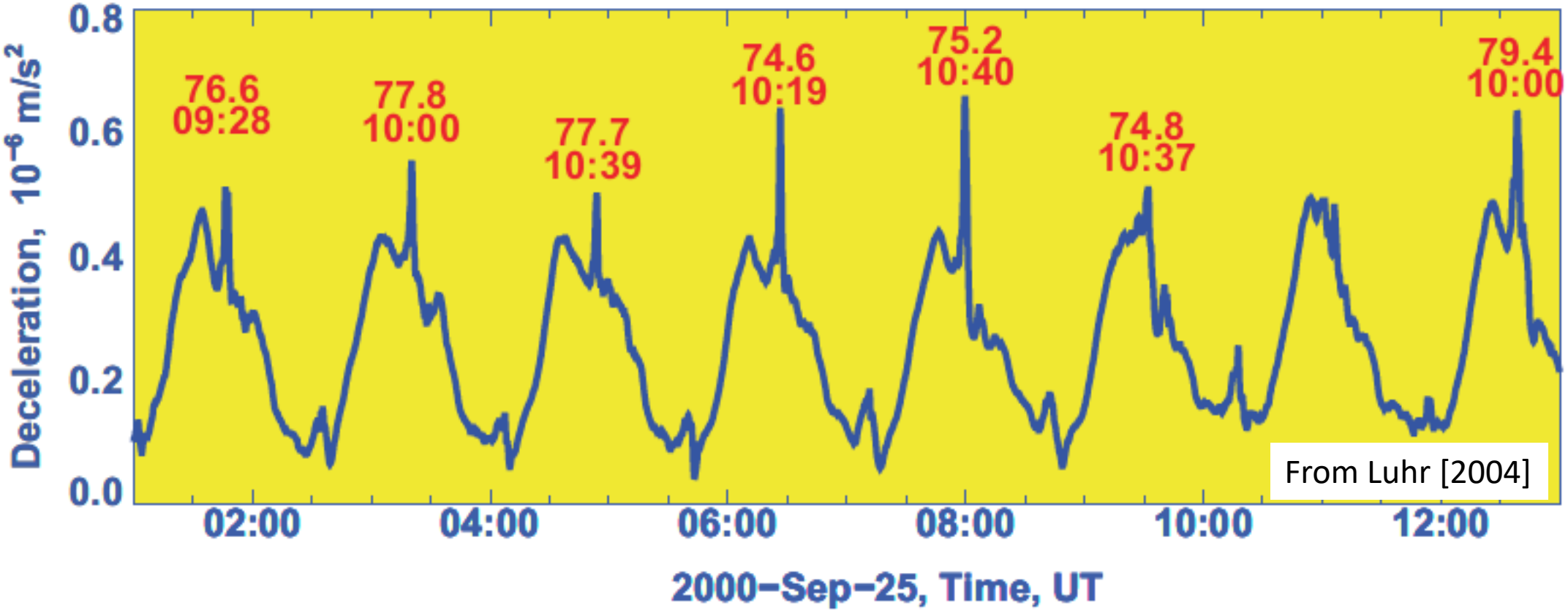

What makes this location especially interesting is the density spike that is observed when the CHAMP satellite passed over the polar cusp region.

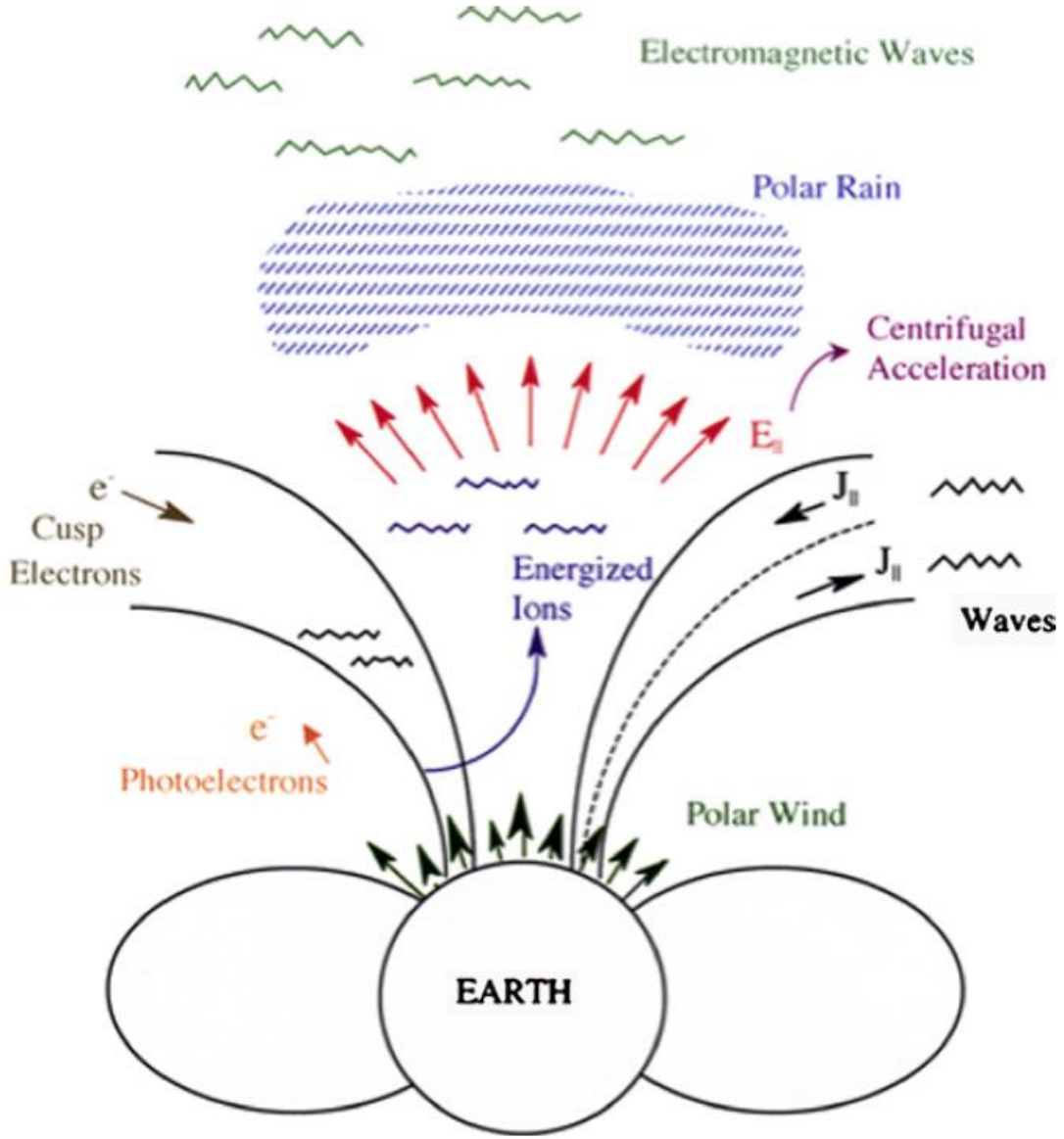

Fig. 16. Schematic diagram showing the near-Earth space environment of the polar wind (from Schunk and Sojka, 1997).

Schunk and Zhu [2008]

75 degree circle marks typical location of the mid-day aurora

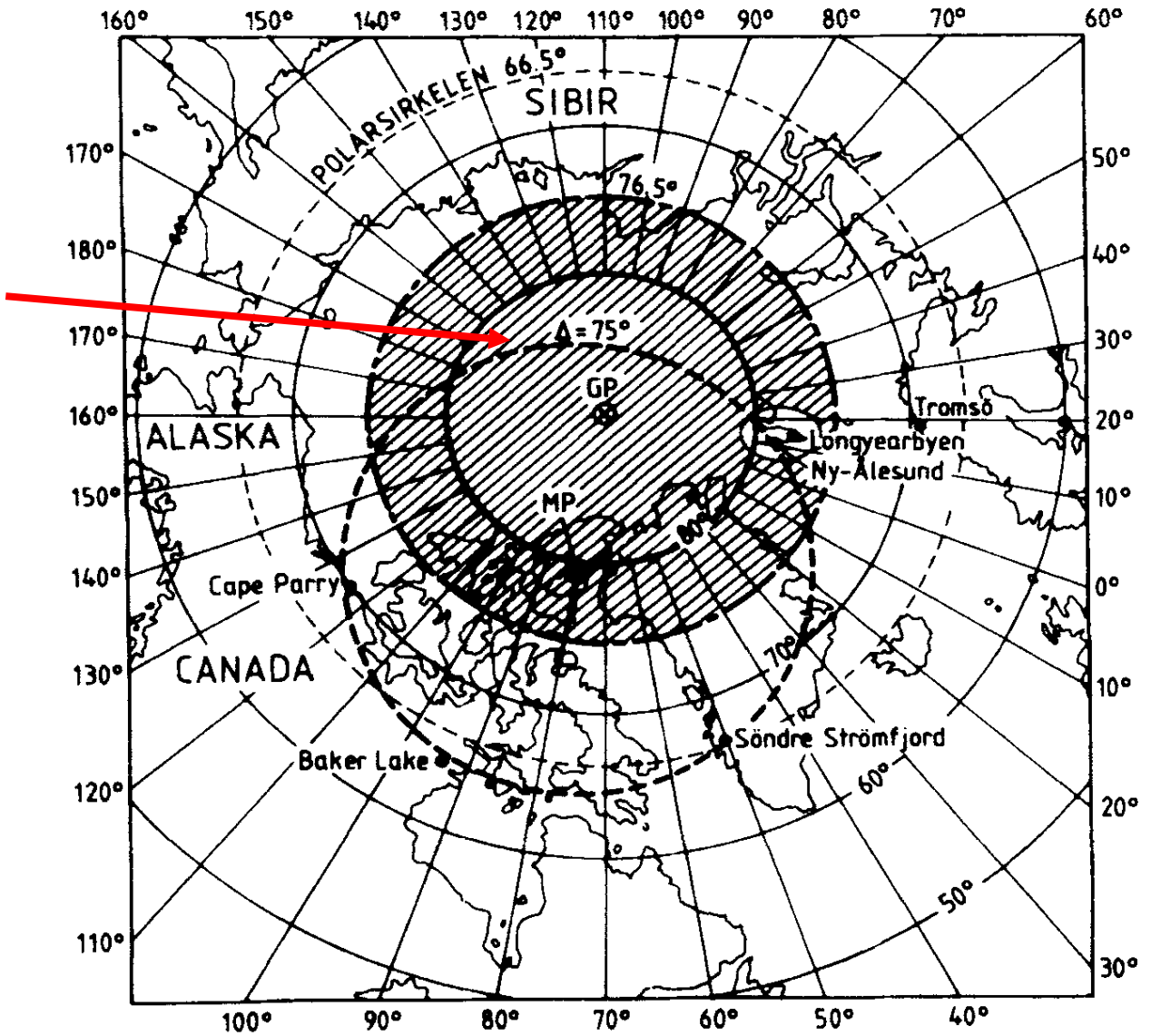

FIGURE 2a. Map showing the northern polar cap where the sun is more than 10° below horizon during midwinter (shaded). The 75° magnetic latitude circle (dotted) indicates the typical location of the midday aurora.

Longyearbyen is ideal for observing the cusp in an optical sense

There, a period of 24 hour continual darkness exists in the months of December and January

The molecular bands in cusp auroras are strongly suppressed compared with the nightside aurora. The main reason for this is that the energy of cusp electrons are well below 1 keV compared to several keV electrons at night. Thus, the cusp electrons are stopped above 200 km compared to 100 km at night. The dayside auroral spectrum clearly reflects the fact that the main atmospheric constituent above 200 km is atomic oxygen. Furthermore, the collision frequency above 200 km is very low.

Hence, atomic emissions—in particular from metastable atmospheric species—dominate the midday optical spectrum which is opposite to the nighttime aurora. The most pronounced emissions besides the red oxygen doublet at 630.0 and 636.4 nm are the [OI] line at 557.7, the [OII] lines at 372.7–2.9 and 732–3 nm, as well as [NI] lines

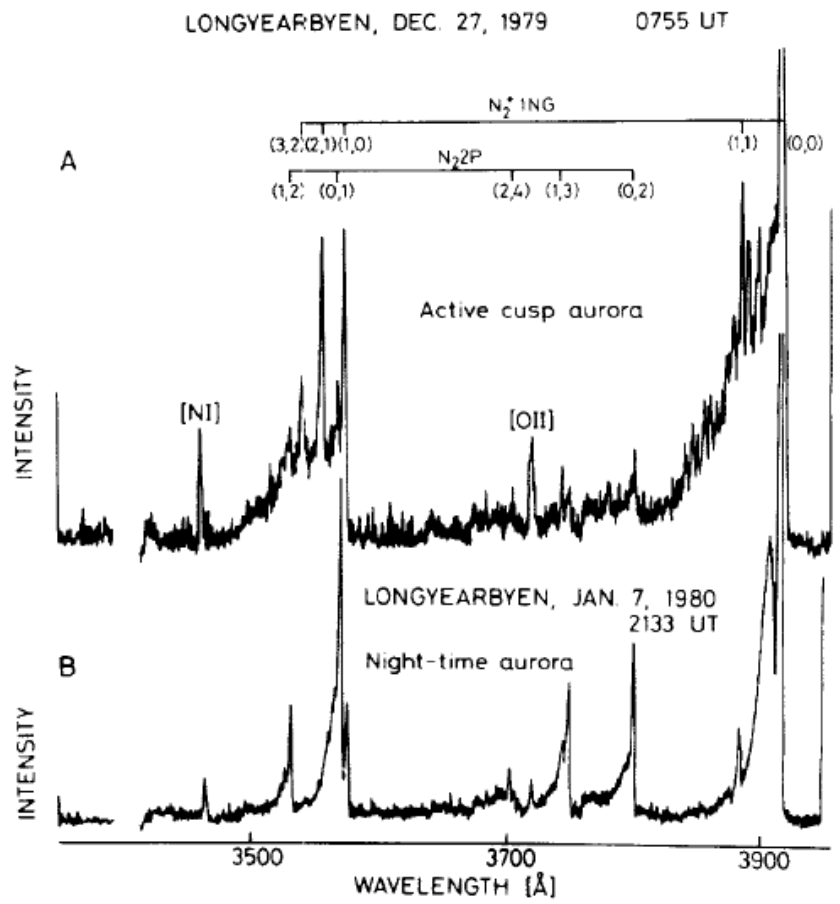

FIGURE 4. Comparison of the spectrum of an active noontime cusp aurora and a nighttime auroral arc observed in the zenith, both from Longyearbyen, Svalbard. Notice the enhanced N_2^+ vibrational distribution and the strong atomic emissions (NI and OII) in the cusp aurora.

A very appealing aspect favoring collection of 732 nm observations at Svalbard is the lack of auroral molecular 1PG emission of N_2.

Otherwise, the O^+ emission is overridden by the many rotational lines of the 27 branches of the First Positive Group bands of N_2 evident in this region.

Plans for KHO in the fall-winter, 2022-2023

My visit to KHO in January 2012 was very impressive such that I became interested in the idea of fielding a 15 cm imaging FPI to KHO.

The focus would be to use the high sensitivity of this instrument to observe both the O 630 nm and the O^+ 732 nm doublet emissions in sequence by using a 15 cm filter wheel.

Such an instrument would take advantage of the general absence of auroral N_2 molecular emissions

The line shape of the O^+ would allow the measurement of the ion temperature Ti. Doppler shifts would also be measurable.

The instrument would be very sensitive, capable of observing 11 rings. Would be able to observe 630 nm wave structures with an accuracy approaching 1 ms^{-1}.

Issue regarding 15 cm objective lens

Tried using achromatic objective lens ($1000) but this did not work because the image was out of focus in the corners of the focal plane. Normally, a long focal length lens is used, such as 75 cm, but this would have meant only one 630 nm ring. This is the setup for the narrow field 15 cm FPI that Anasuya Aruliah was operating at KHO.

I wanted to work at shorter focal lengths so that I could get multiple rings, as many as eleven. This is equivalent to broadening the field of view from 0.2 deg full angle to 2.0 degrees full angle. However, the problem is that the focal plane is then curved. This explains why the image was out of focus in the corners but in focus at the center.

It proved to be possible to design a multiple element objective lens assembly where a corrector lens is added to produce an image In the focal plane that would be flat.

Will show results from JJO illustrating the instrument and both 630 nm nightglow and 732/OH nm twilight-nighttime observations

Full

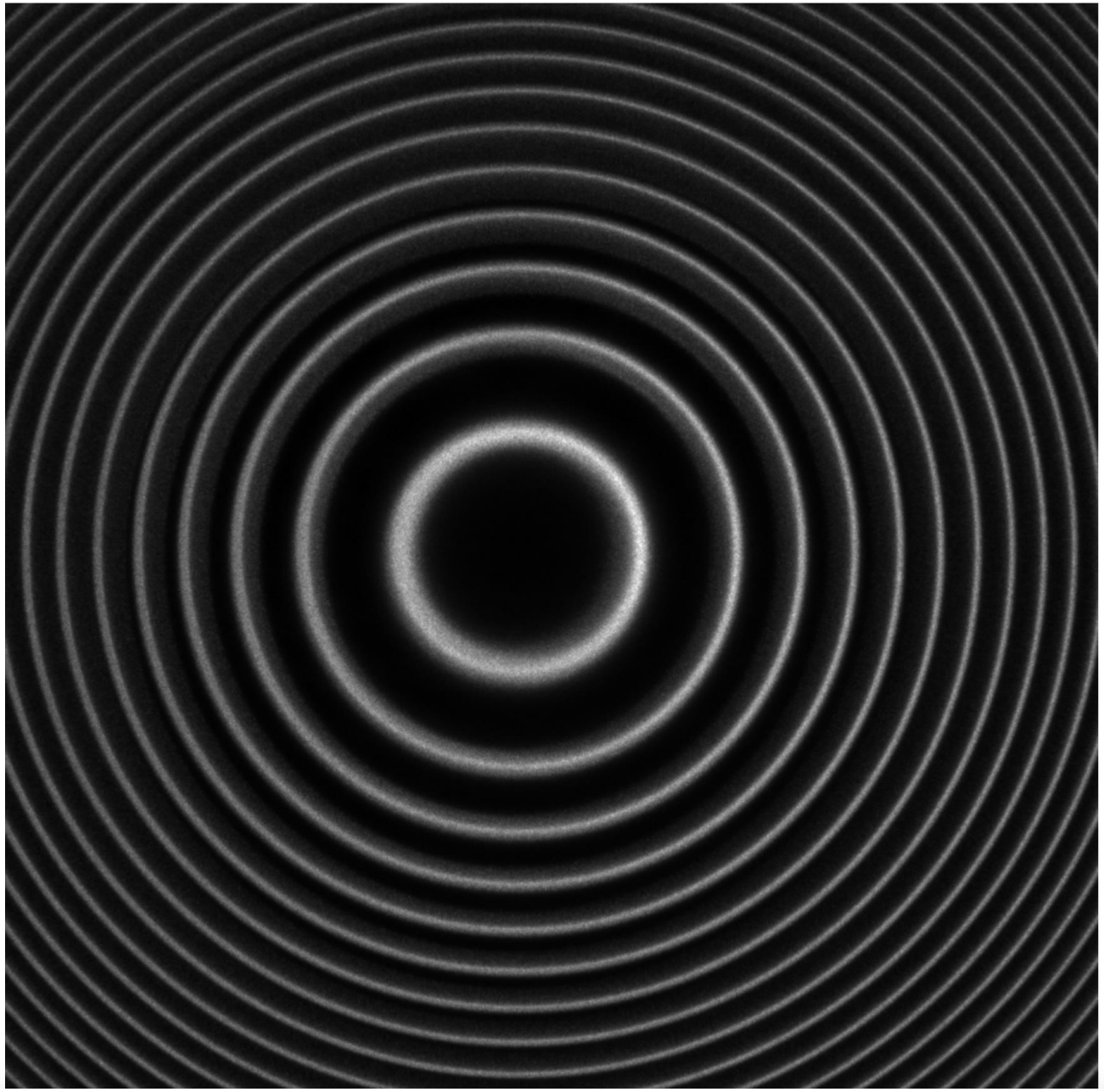

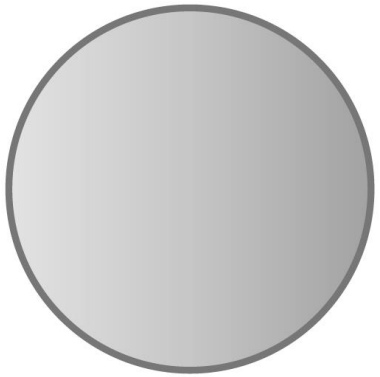

Aperture at Center (r0)

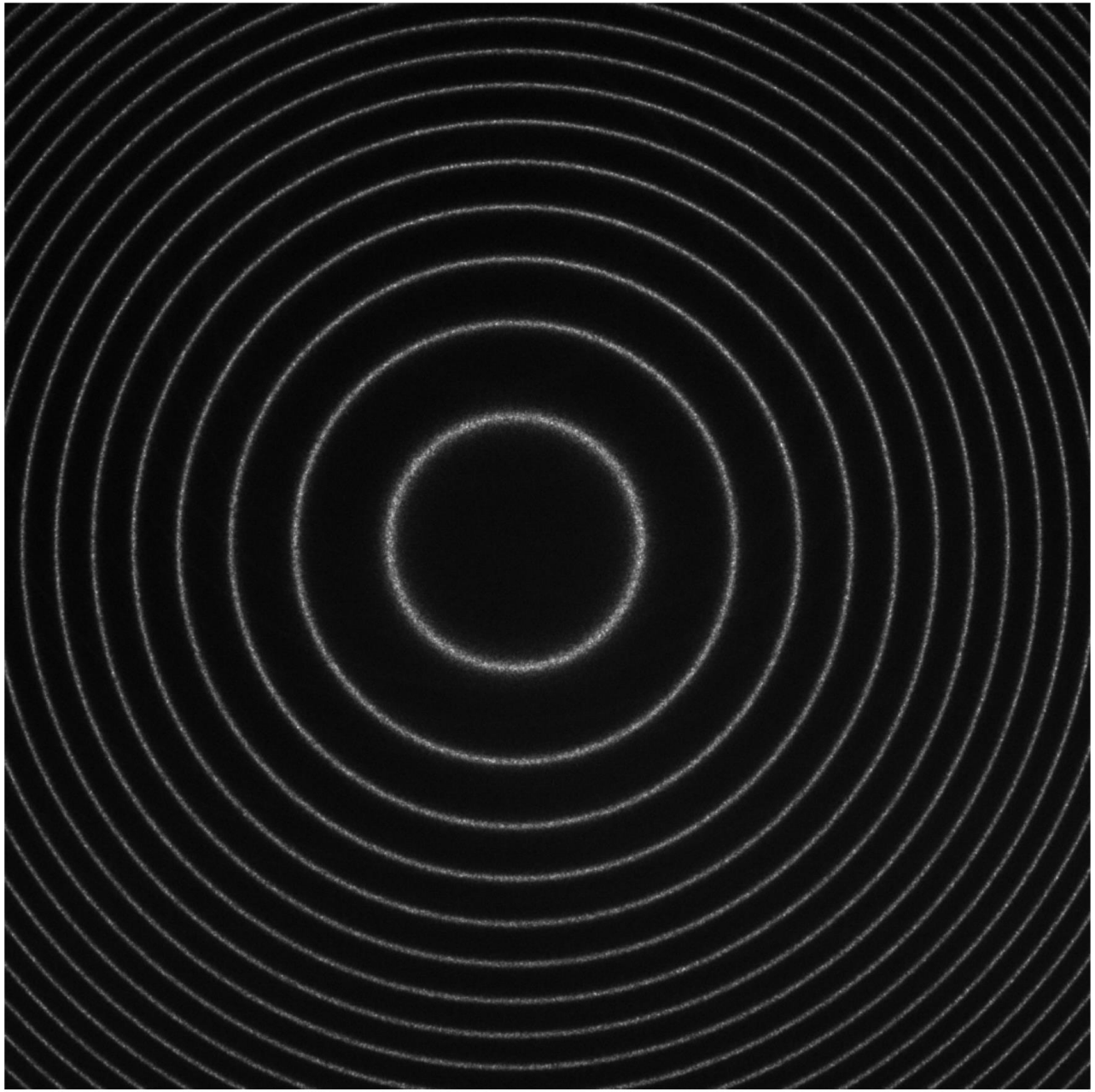

Aperture at Center (r0)

Cross hair target

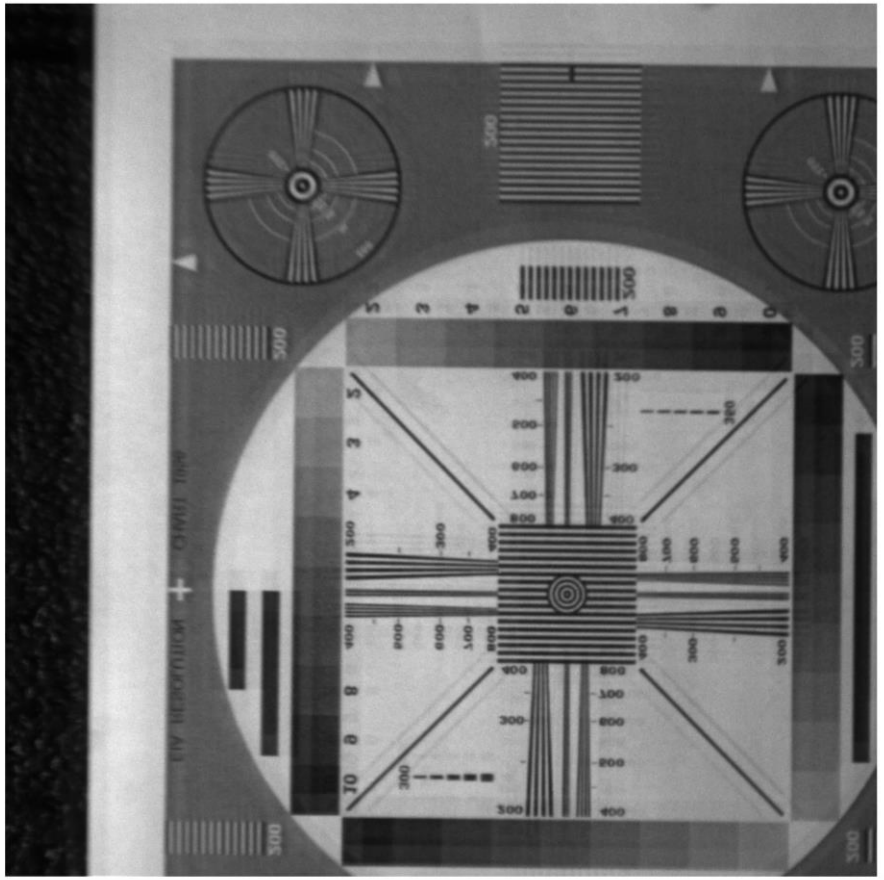

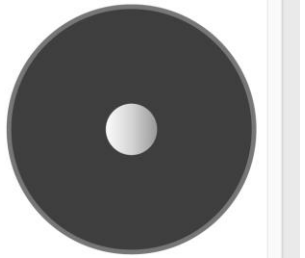

No etalon in optical axis

Focus is obvious

Aperture at Edge, 2:00 (r1o02)

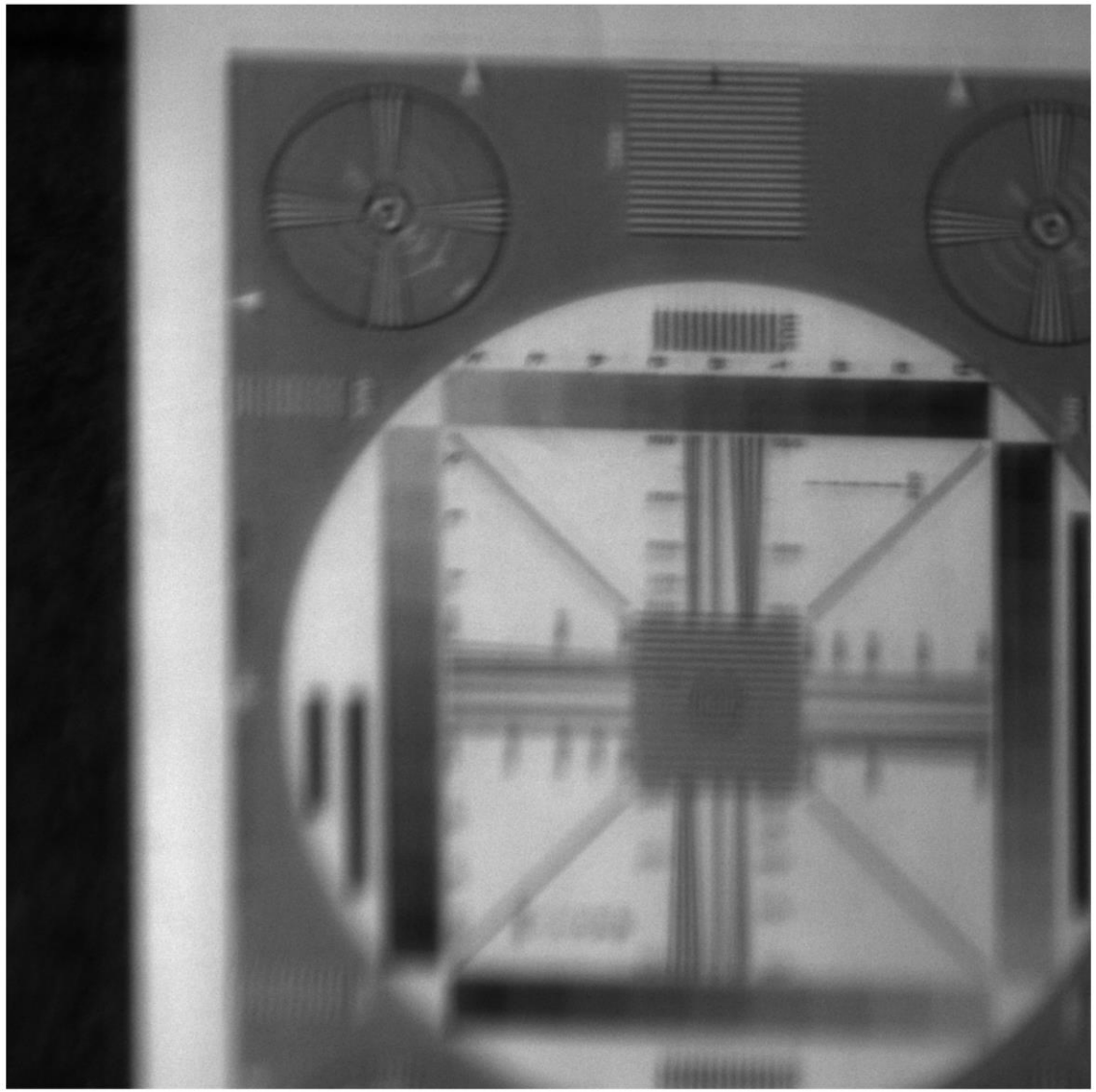

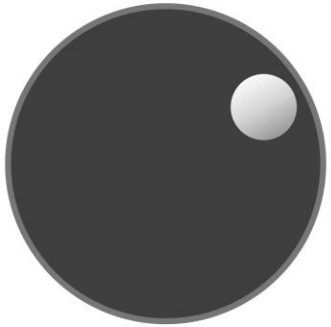

Out of focus

Characteristics of the JJO Fabry-Perot interferometer

- 15 cm aperture diameter – as big as they come – the MaxFPI instrument would be 20 cm
- Apochromatic lens assembly designed to flatten focal plane so the whole field is in focus
- Highly sensitive low noise CCD camera as detector
- Double axis SkyScanner provides flexibility for observing in any direction
- Two filter capability using a four position filter wheel constructed in Clemson machine shop
  - 630 nm and 732 nm filters with 1 nm band width and 55-60 % transmission

Home of the Jenny Jump FPI observatory (40.92 N, 74.9 W)

SkyScanner – az and zenith independent axes

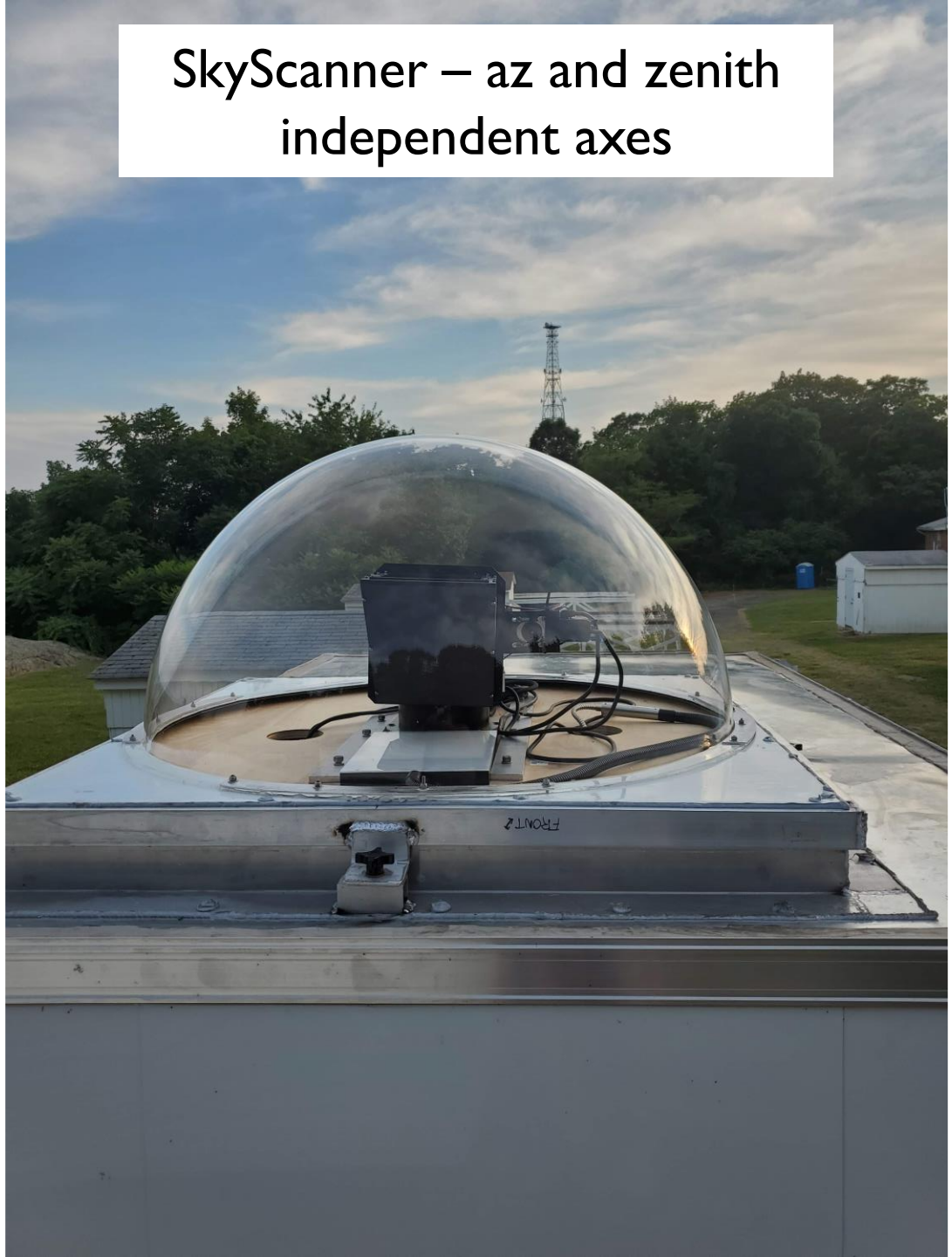

FPI assembly at the laboratory test table

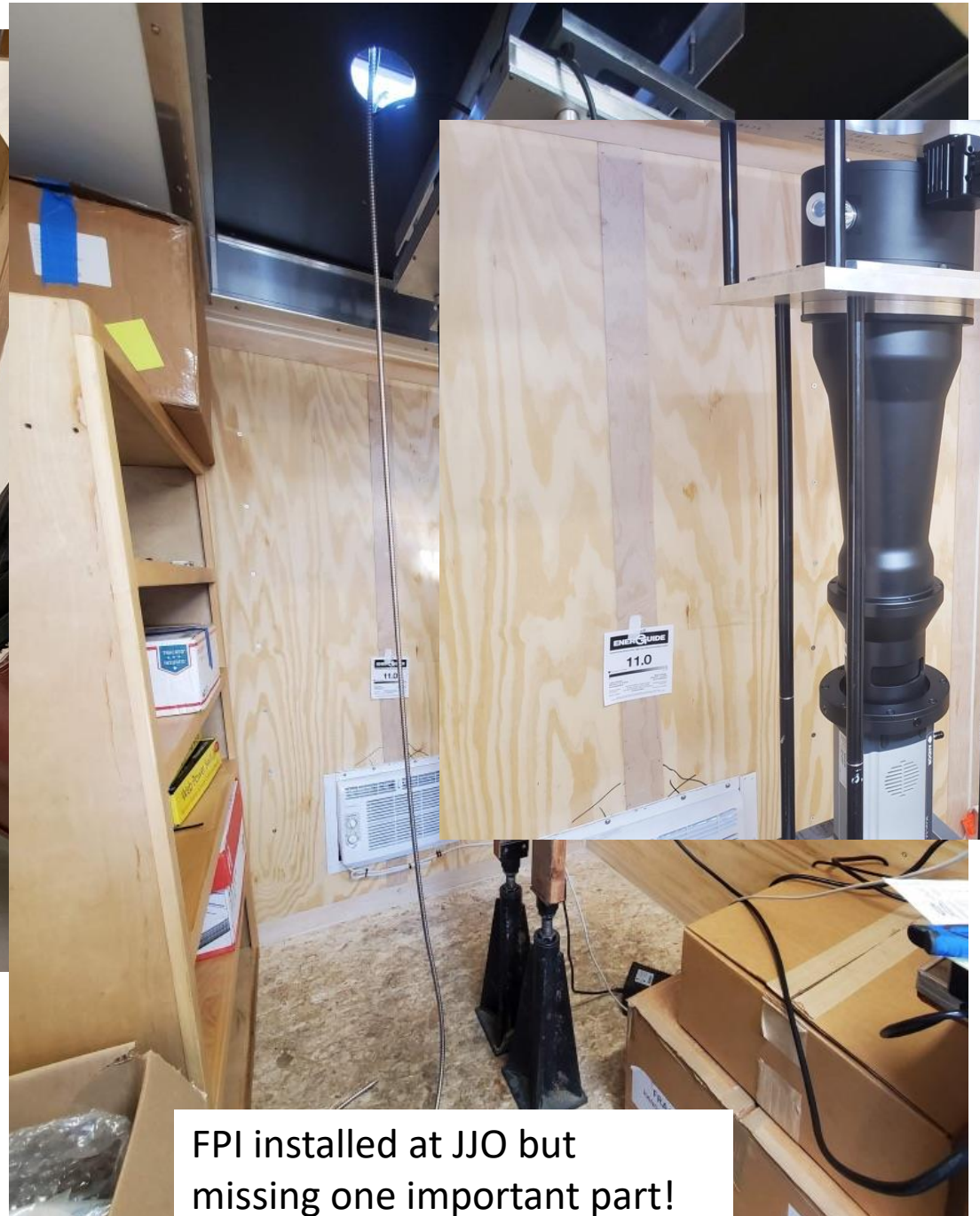

FPI installed at JJO but missing one important part!

View with etalon mounted aligned with the optical axis

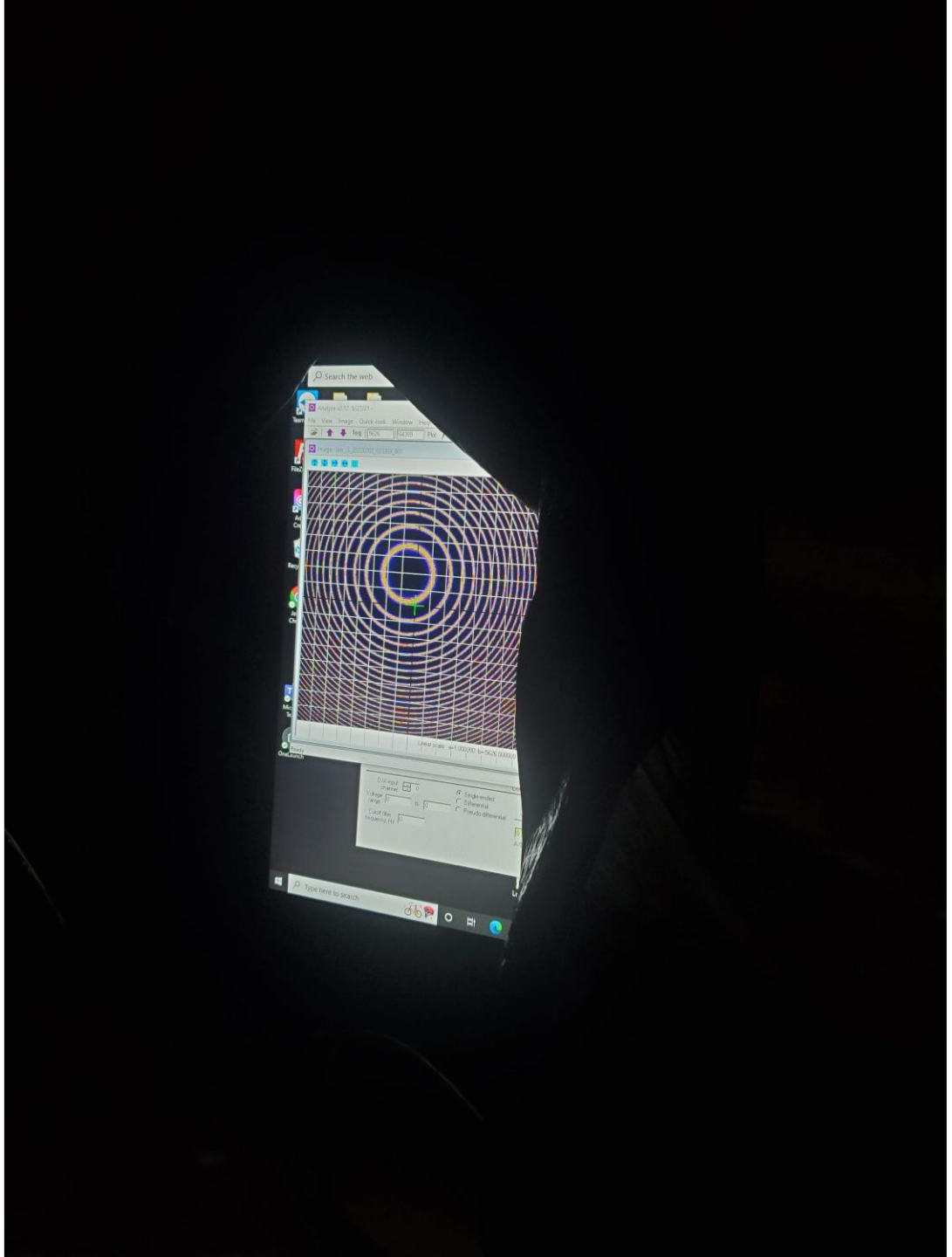

First light!

2 July 2022

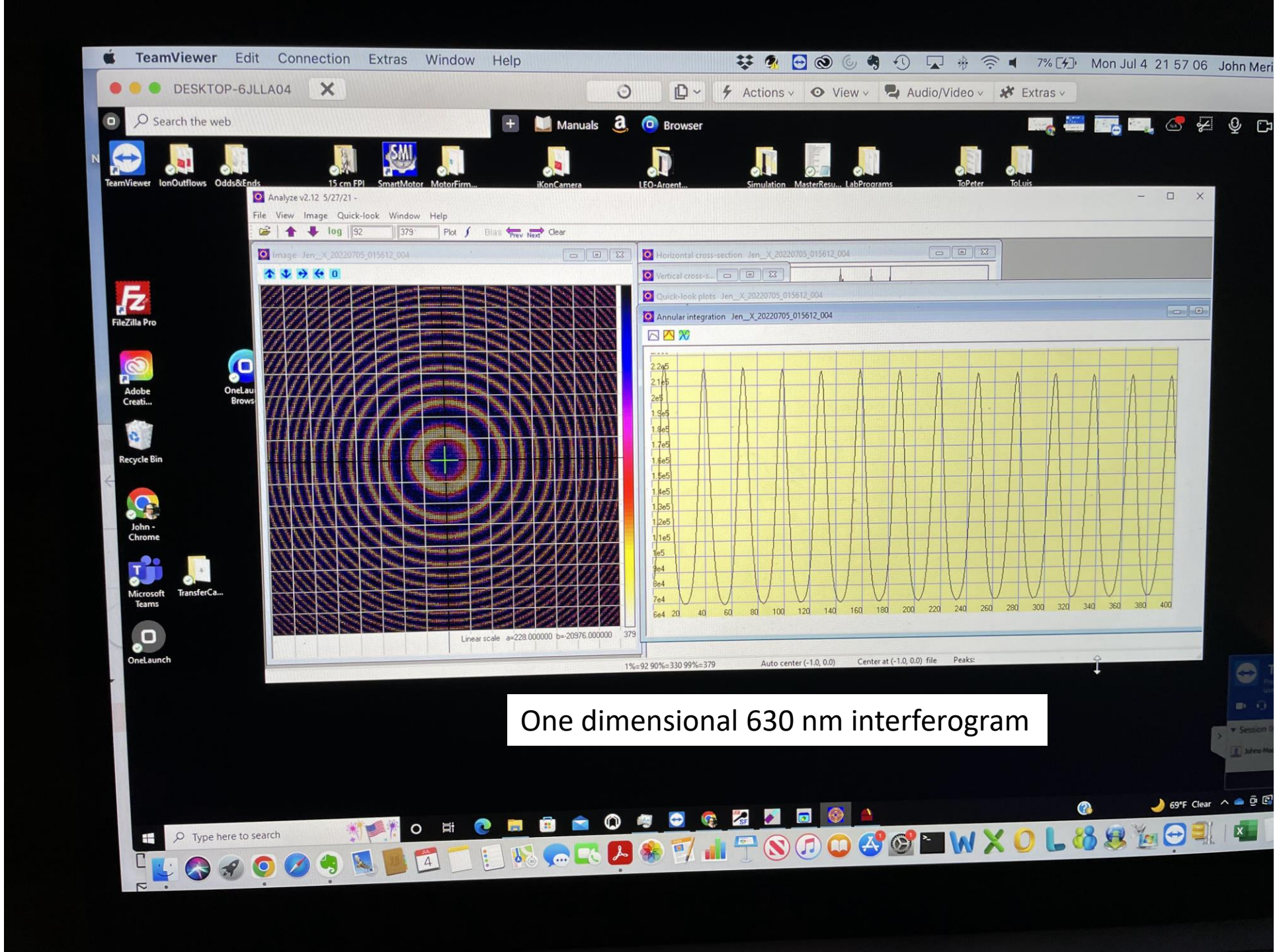

One dimensional 630 nm interferogram

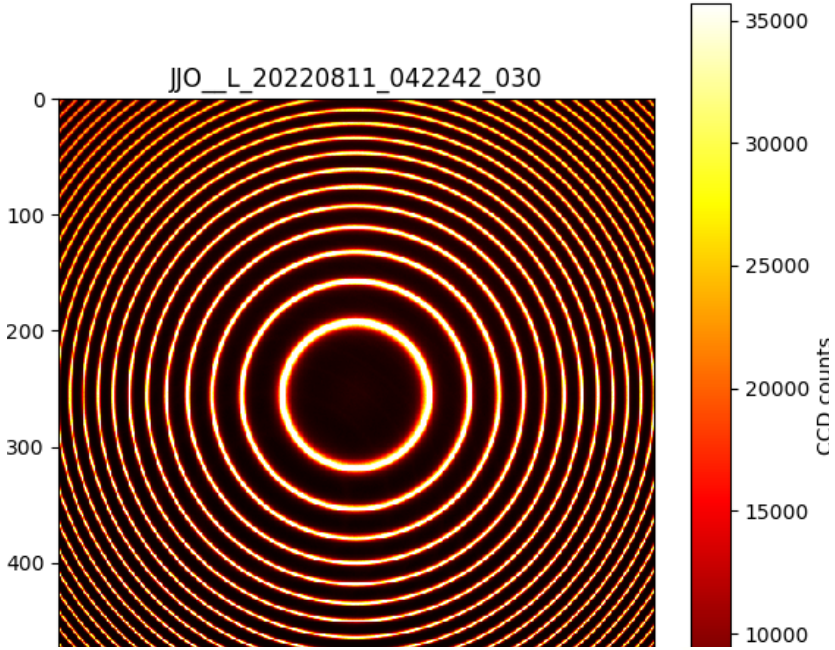

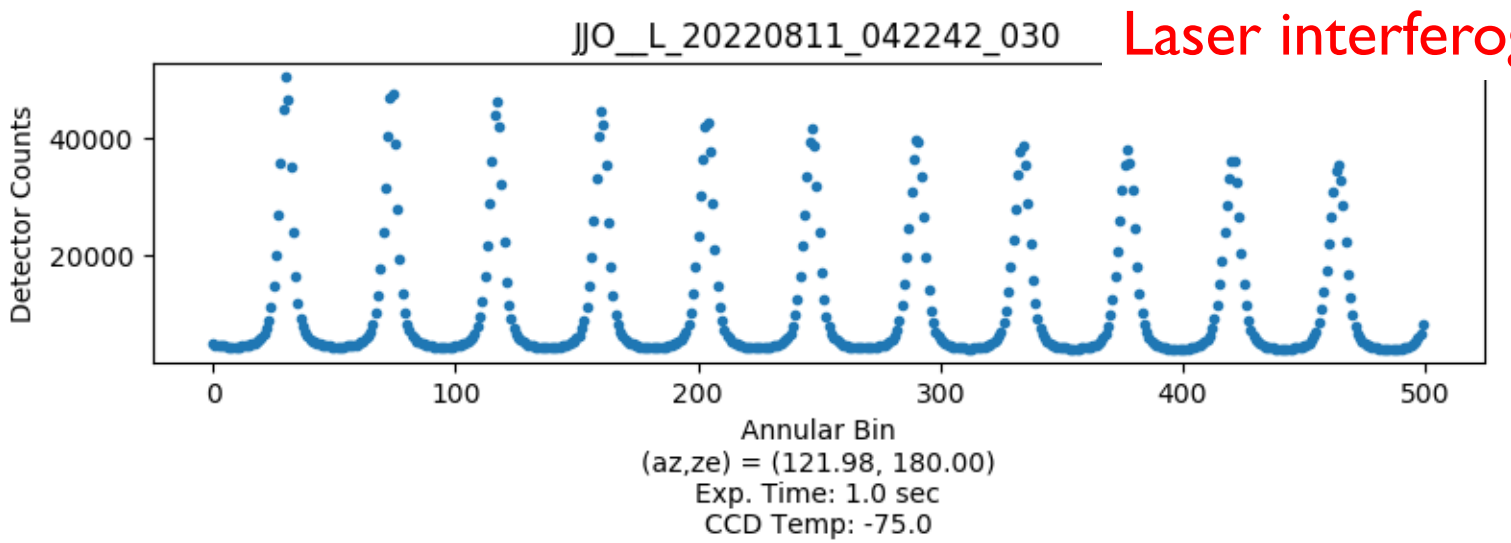

Laser interferogram

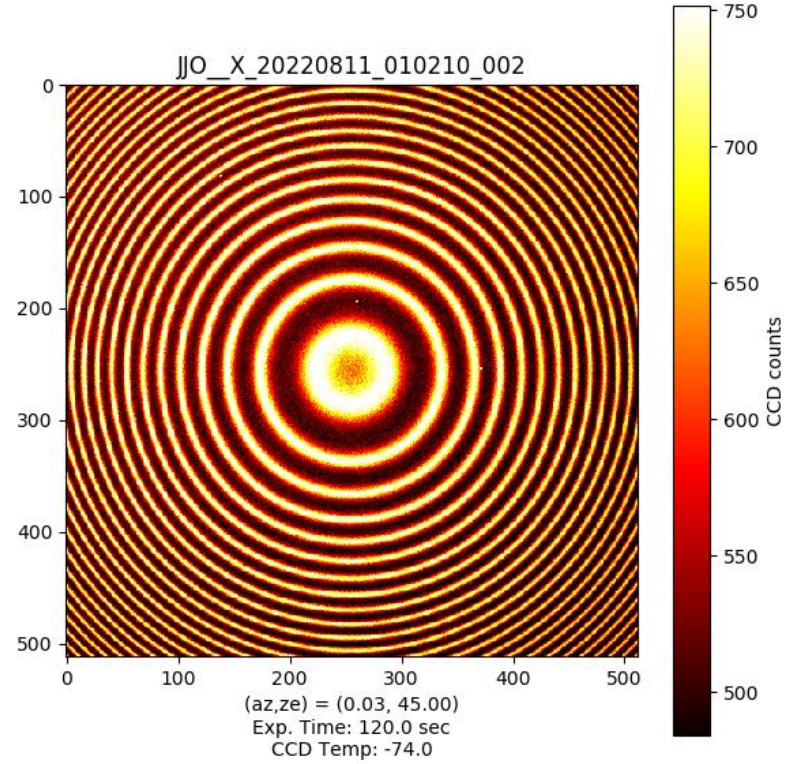

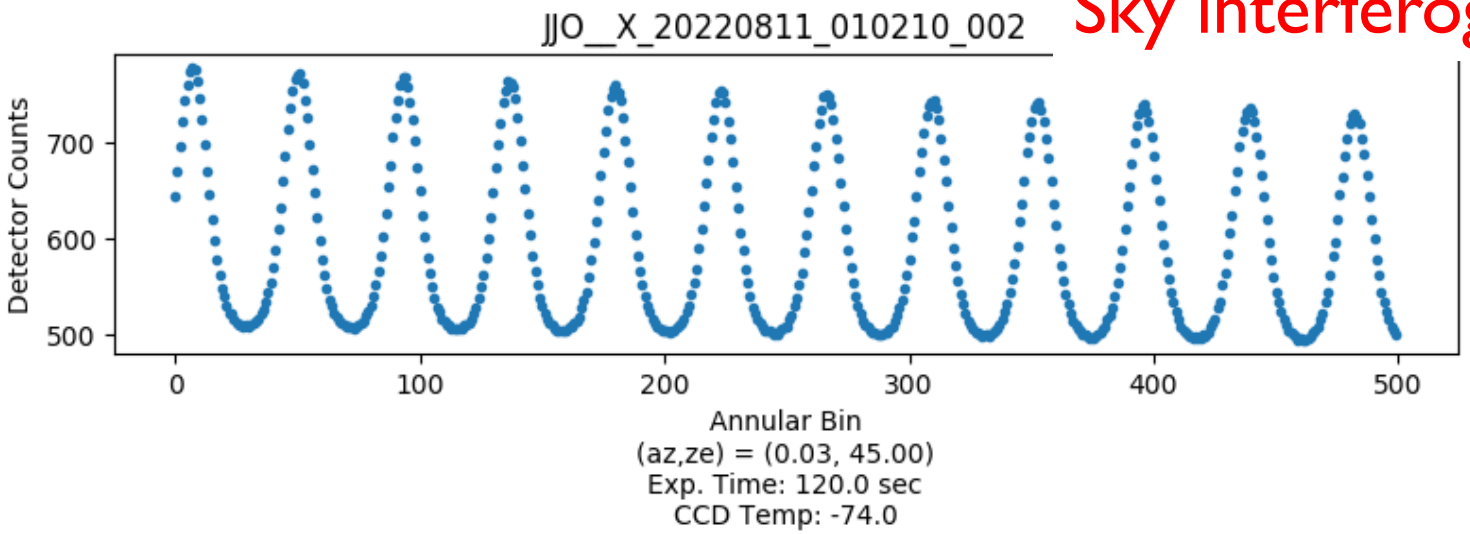

Sky interferogram

These are independent orders so this is like having 11 separate FPIs, each with a slightly different field of view

Data analysis

Just a brief description of the data analysis processing that is applied (based upon Harding analysis algorithm).

Image will show signs of vignetting effects but the amount of energy per order is the same. So, slightly lower resolution near the edge due to broadening.

- Find ring center. Use many laser cals (~70) for this purpose to track behavior during the night.
- Conversion of 2D image to 1D by annular summing around ring center
- Apply a modified version of the Airy function as a model that includes Doppler broadening and Doppler shifts.
- Assume source emission is Gaussian in speed distribution of moving O^1D atoms
- Relative intensity determined from the area of the 1 D interferogram order
- Apply a nonlinear least square model fit to get the best determination of the Doppler profile deconvolved from the sky spectral profile. Estimates of Doppler broadening and Doppler shifts can then be obtained.

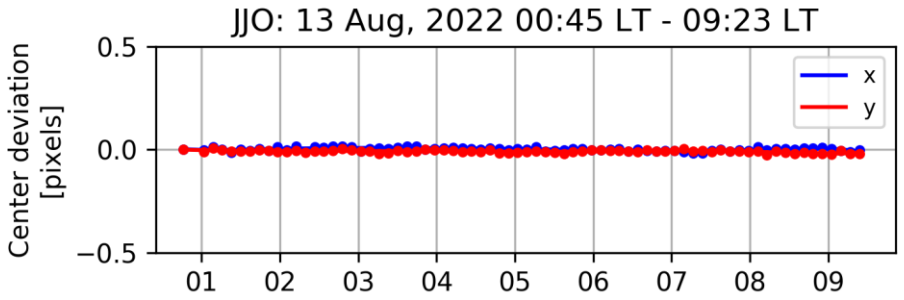

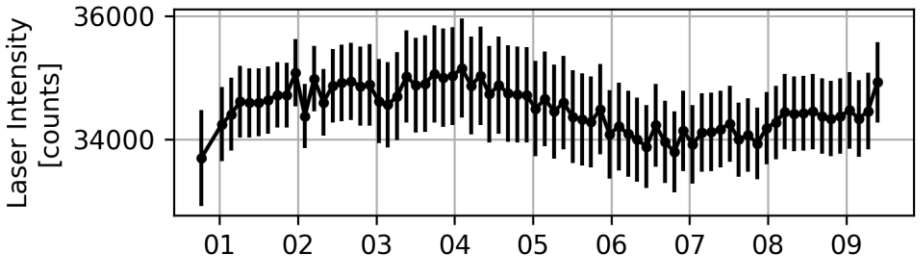

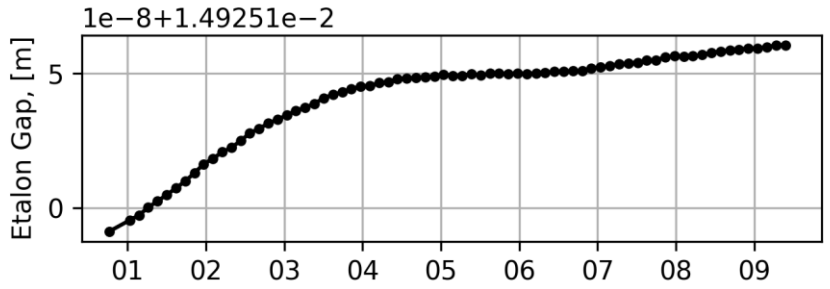

Examples of ring centering, variation of laser intensity with time, etalon spacer gap drift due to thermal changes in trailer,

and 630 nm sky intensity variation through the night.

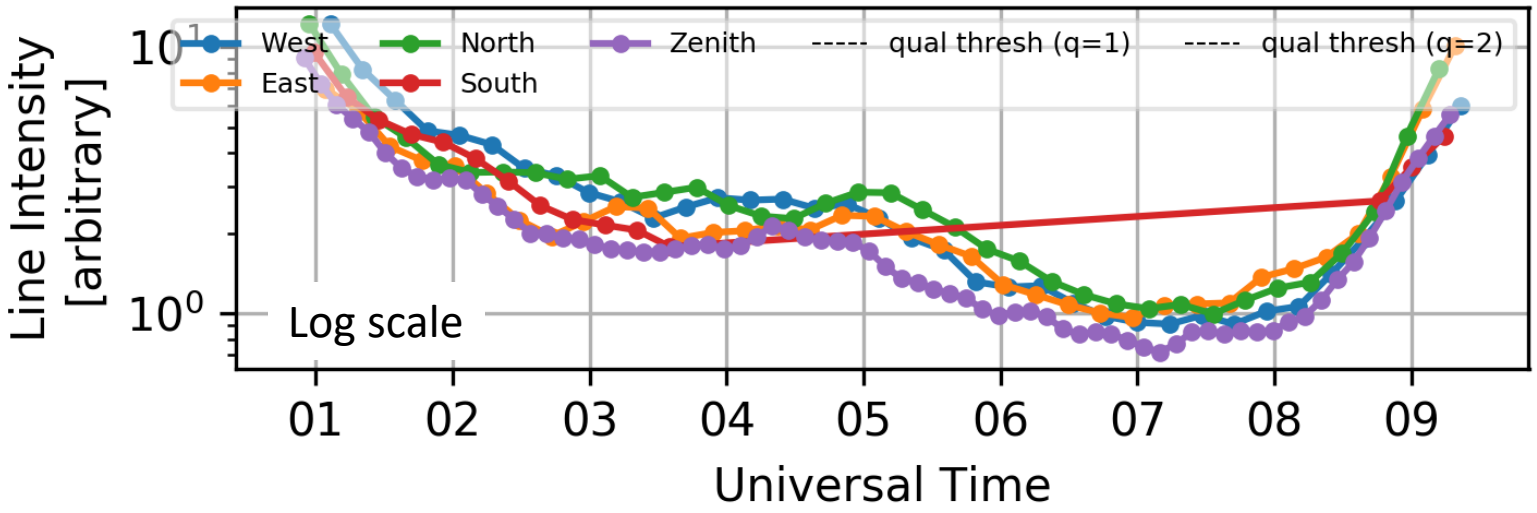

Results for 13 August 2022

JJO__L_20220712_012209_001.img 13 Jul 2022 01:22:01 Laser(122.0,180.0)

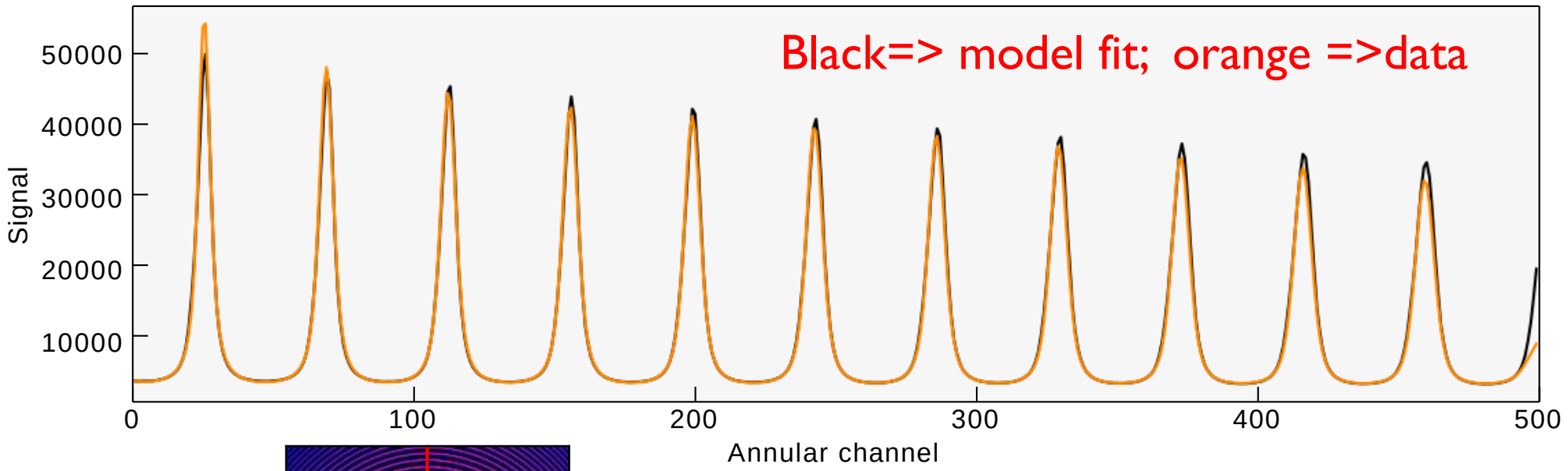

Illustration of model fit with data and residuals

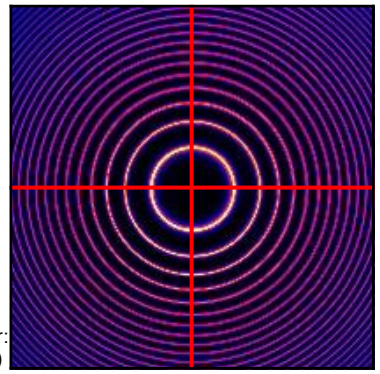

t	0.015 ± 1.73e-10(0.00%)
R	0.76 ± 0.00259(0.34%)
alpha	8.7e-05 ± 4.29e-09(inf %)
I	6.8e+04 ± 1.19e+03(1.74%)
B	2.3e+03 ± 16.8(0.74%)
a1	-0.043 ± 0.0113(26.14%)
a2	-0.012 ± 0.00331(27.69%)
b0	1.5 ± 0.0651(4.42%)
b1	0.52 ± 0.0463(8.86%)
b2	-0.19 ± 0.0564(30.39%)

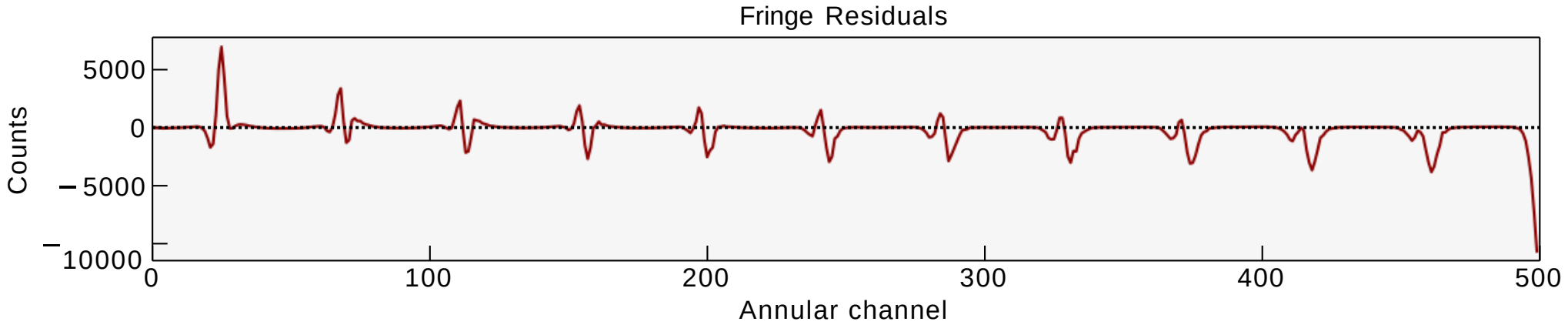

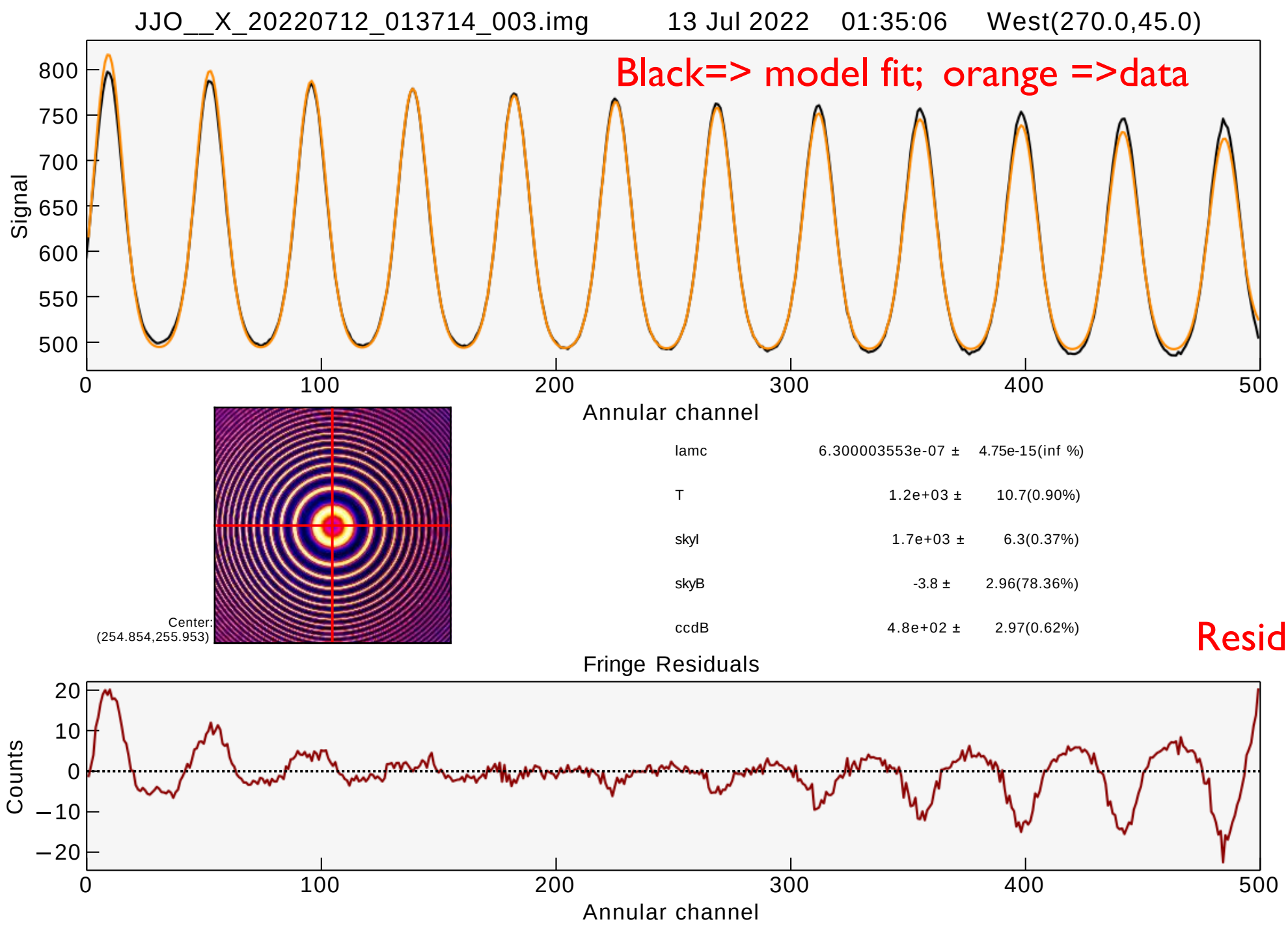
JJO__X_20220712_013714_003.img 13 Jul 2022 01:35:06 West(270.0,45.0)
Black=> model fit; orange =>data
Signal
Annular channel
Center:
(254.854,255.953)
lamc 6.300003553e-07 ± 4.75e-15(inf %)
T 1.2e+03 ± 10.7(0.90%)
skyI 1.7e+03 ± 6.3(0.37%)
skyB -3.8 ± 2.96(78.36%)
ccdB 4.8e+02 ± 2.97(0.62%)
Residuals
Fringe Residuals
Counts
Annular channel

Analyzed Results!

- Start with most interesting finding: vertical winds

- Will compare JJO results with results from MHO and UAO

MHO is Millstone Hill Observatory FPI – some 325 km to the north
UAO is Urbana Airglow Observatory, some 800 km to the west

WZN series of directions

Eastward and then southward

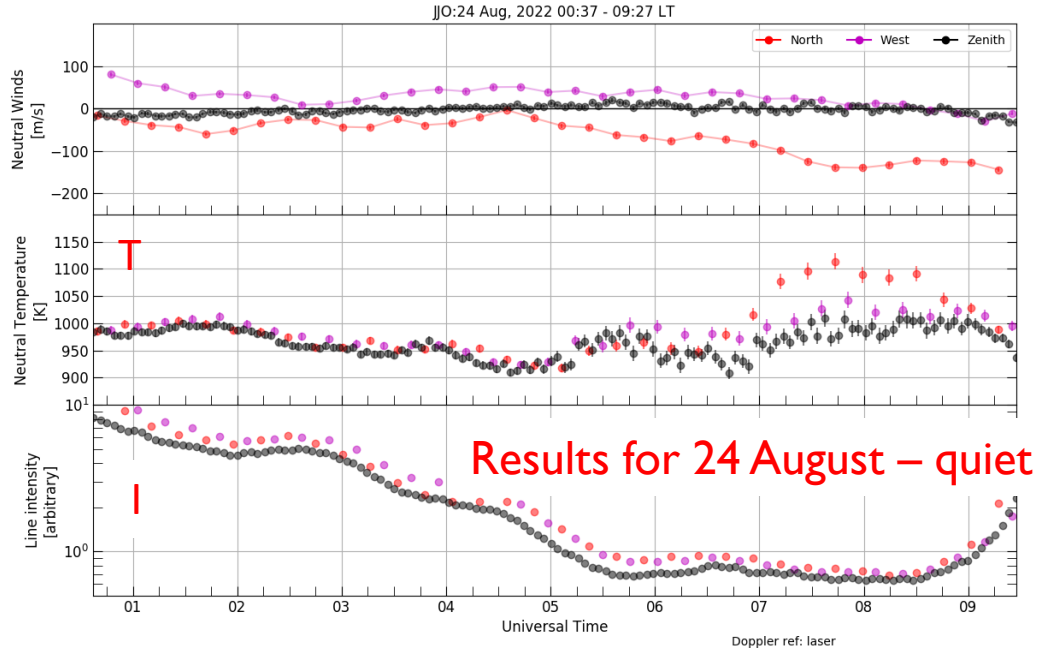

Results for 24 August – quiet day

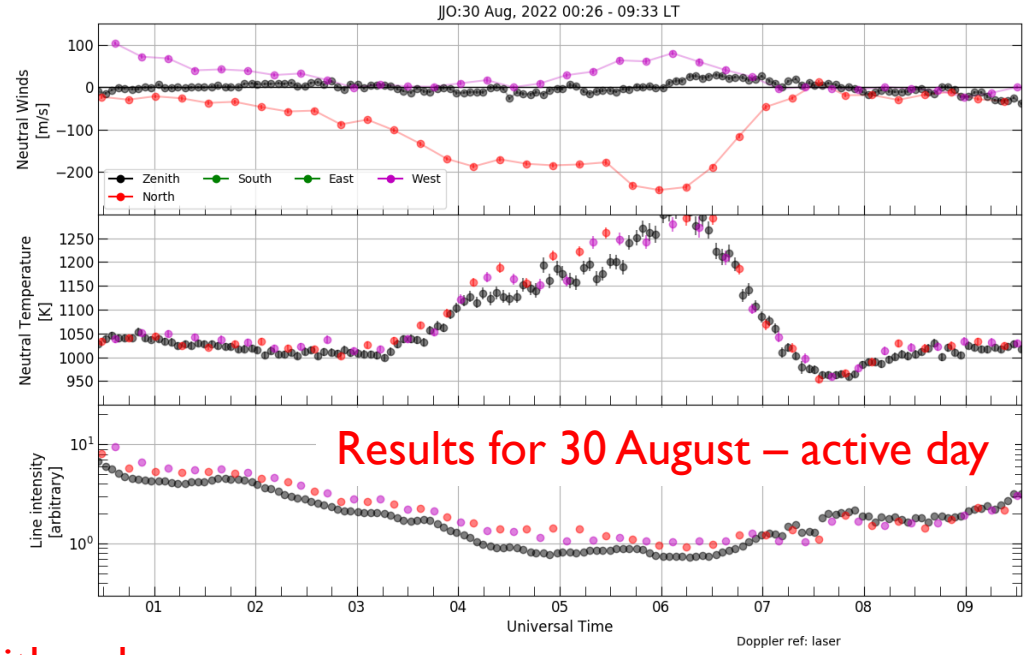

Results for 30 August – active day

Zenith only

Expanded scale

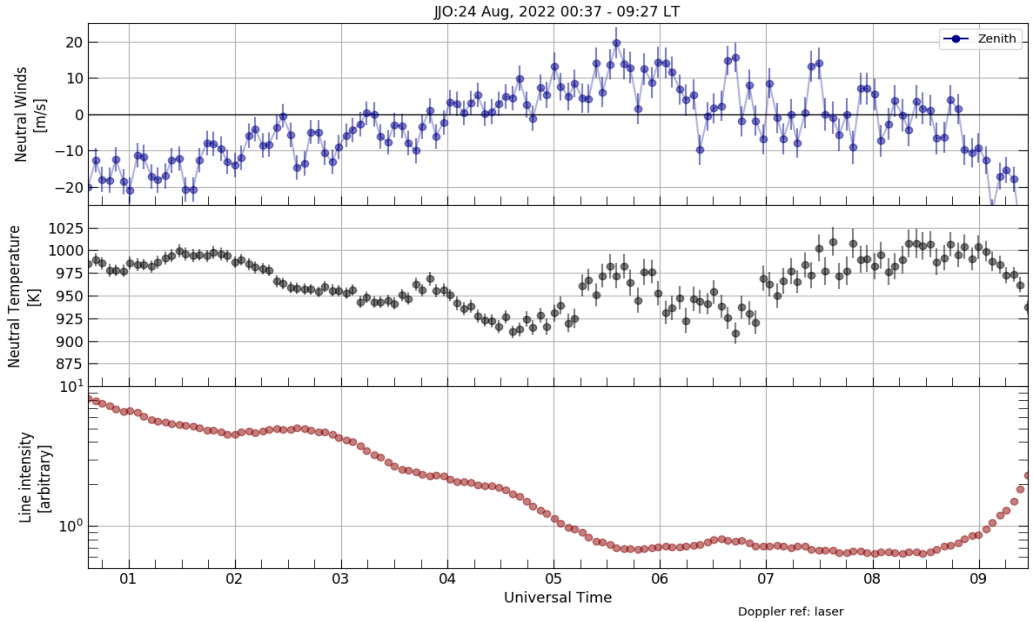

Zenith only

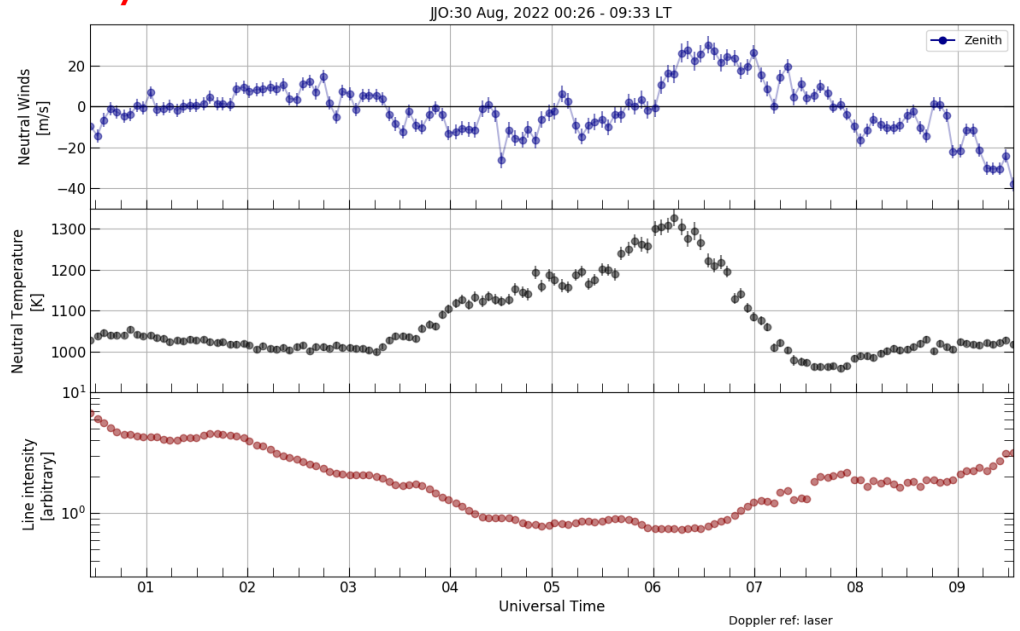

25 July 2022

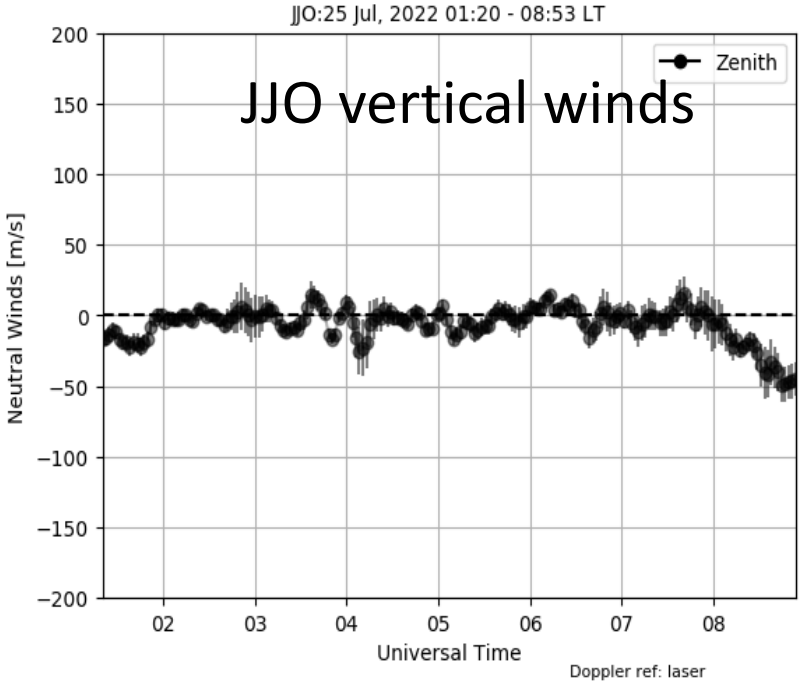

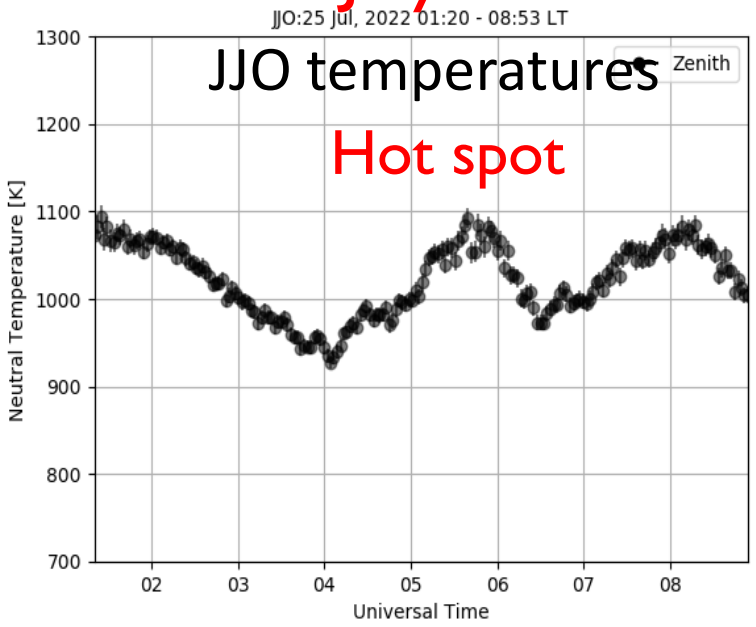

Vertical direction only

Oscillatory behavior seen in w within range of 5 to 10 ms-1

Very interesting JJO vertical wind and temperature results with "hot spot" near 6 UT.

"Who ordered this!"

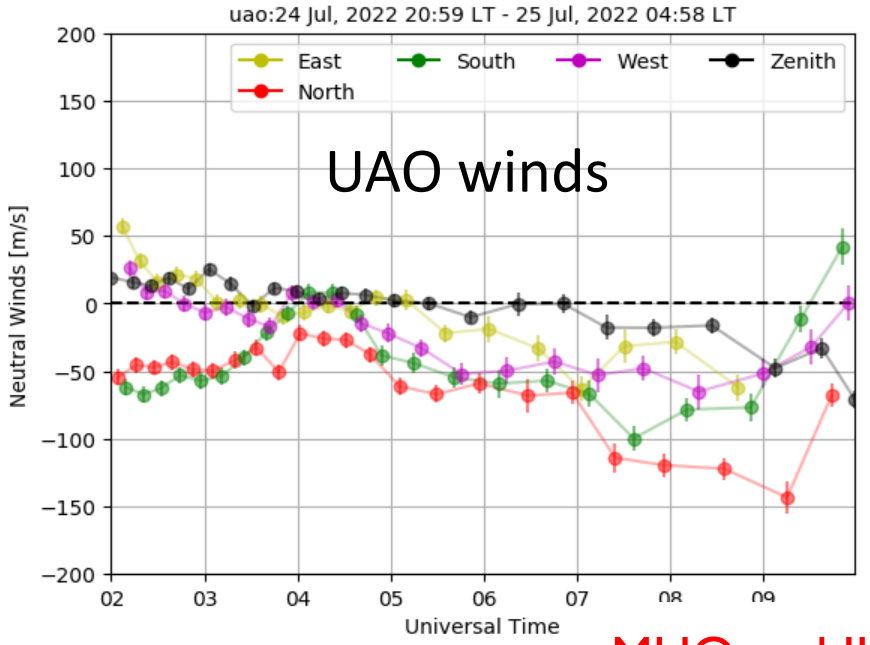

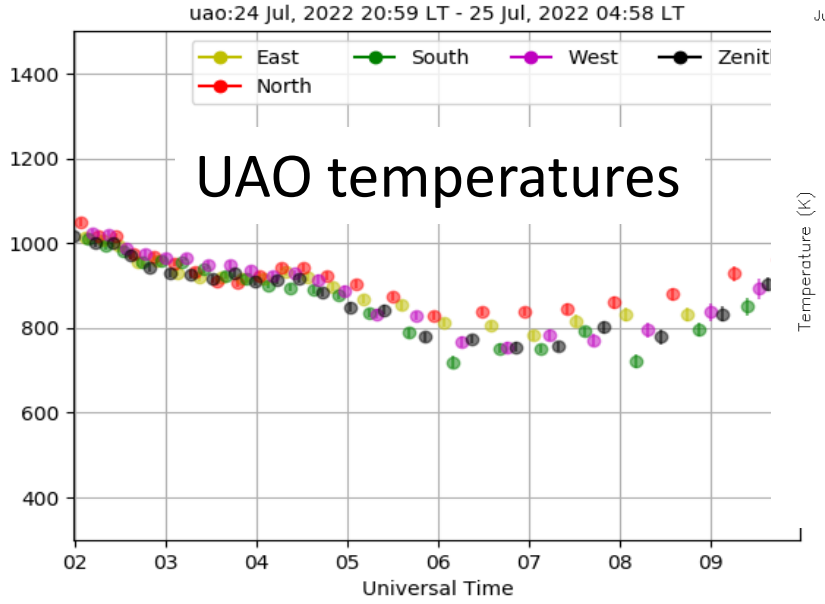

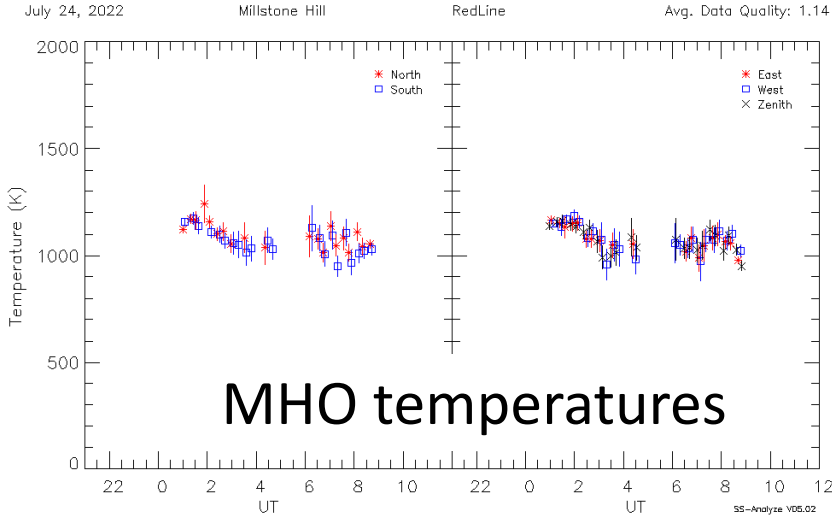

MHO and JJO temperatures similar; UAO temperatures typically 100-150 K lower

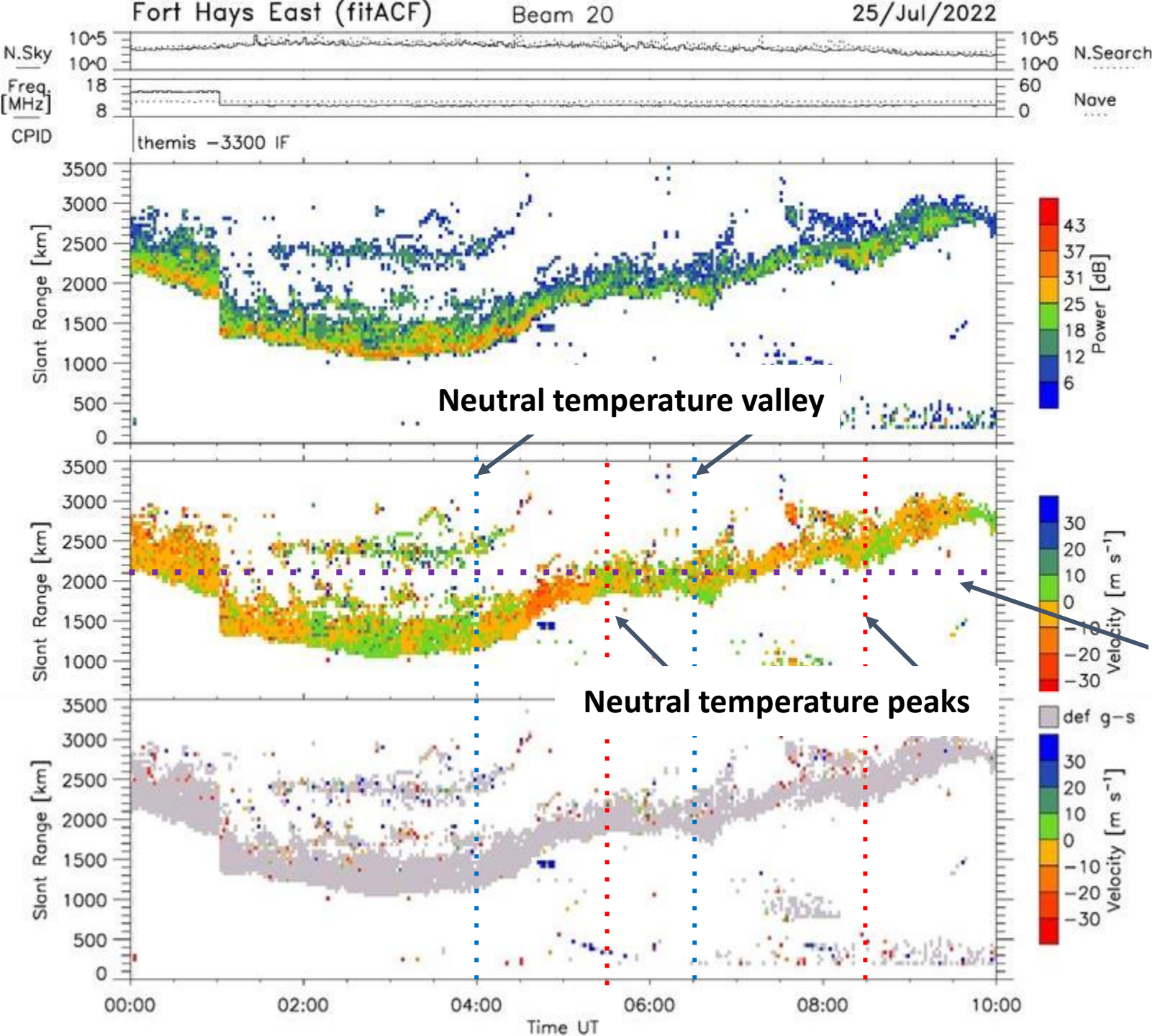

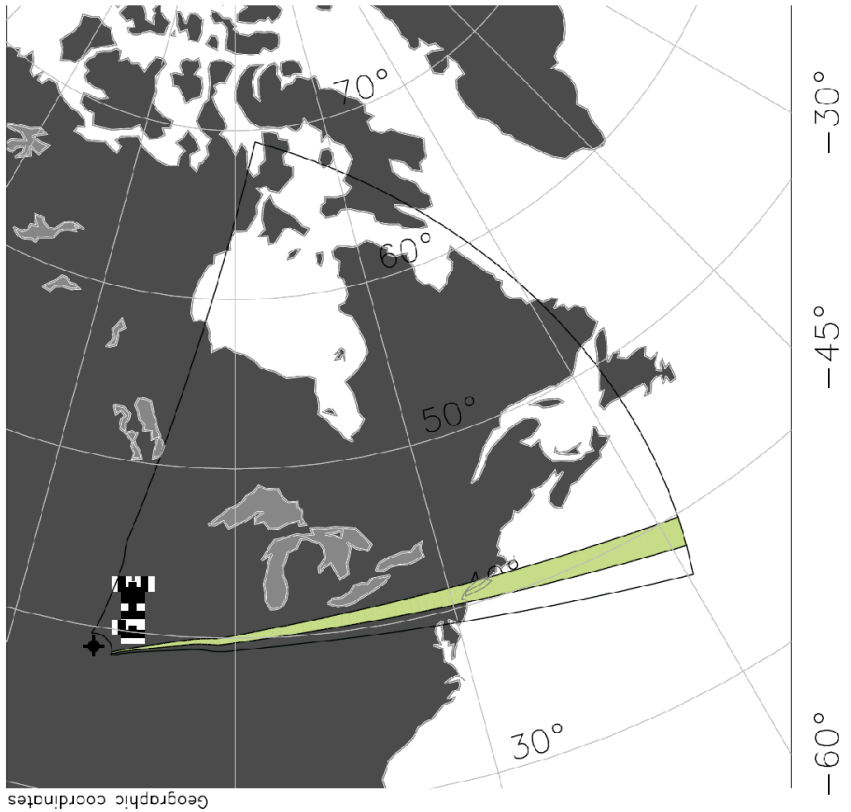

JJO Location

Eastward plasma flows seen preceding neutral T enhancements, and westward flows preceding T minimums. Possibly indicating a role of ion-neutral frictional heating in enhancing T.

Thanks to Lindsay Goodwin (NJIT) for this.

26 July 2022

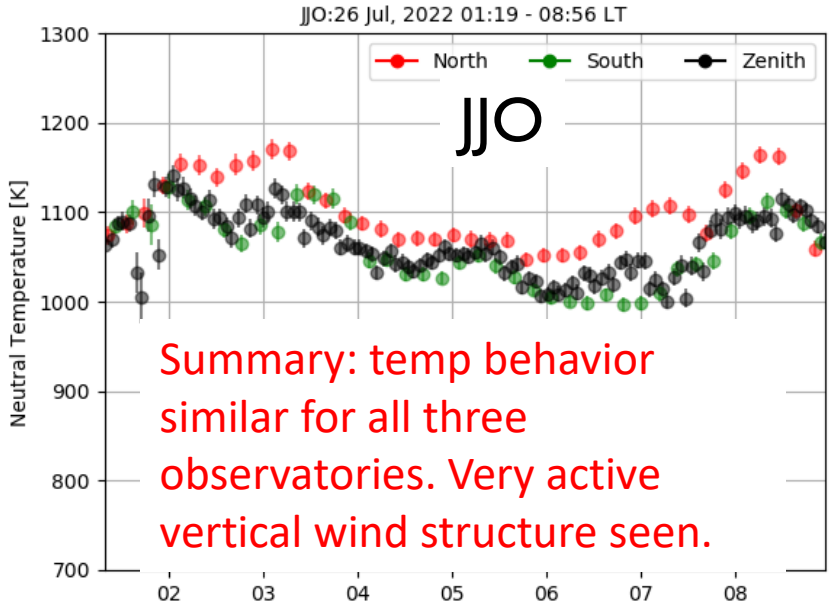

Summary: temp behavior similar for all three observatories. Very active vertical wind structure seen.

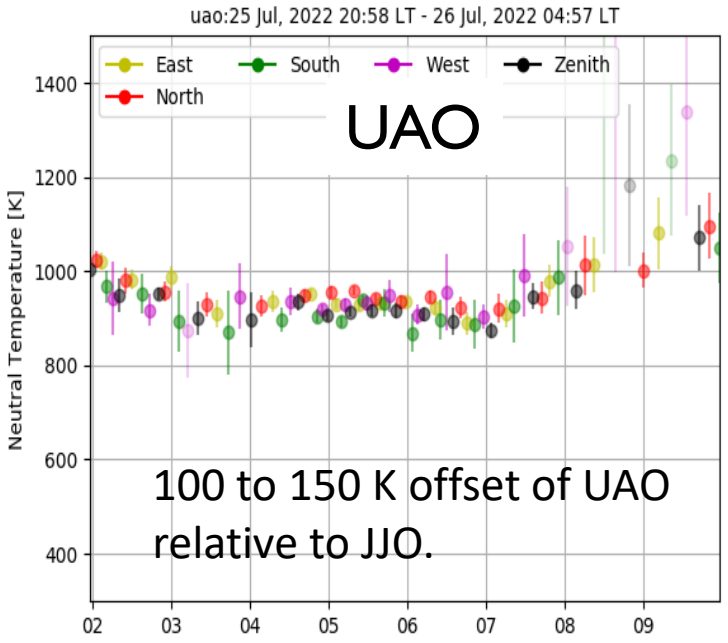

100 to 150 K offset of UAO relative to JJO.

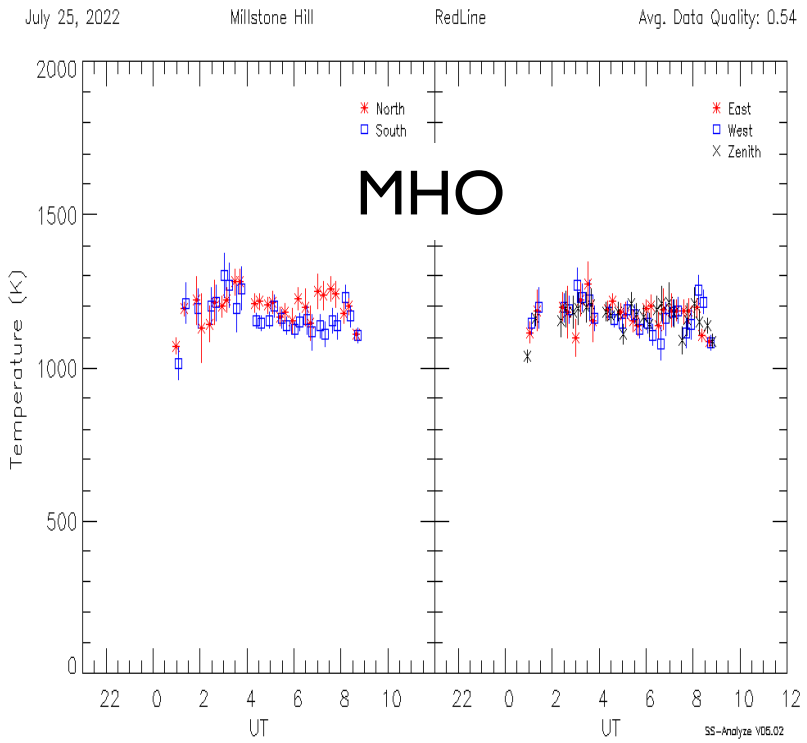

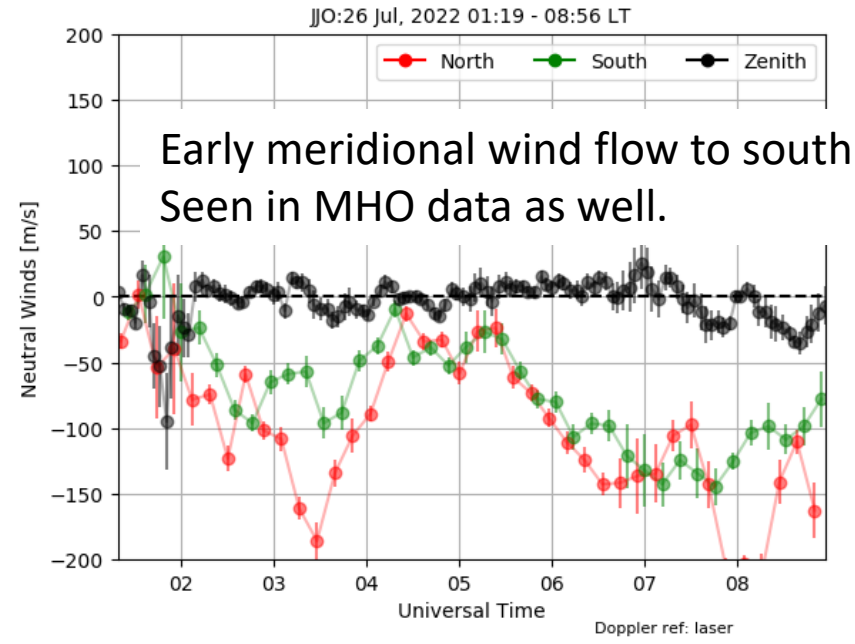

Early meridional wind flow to south. Seen in MHO data as well.

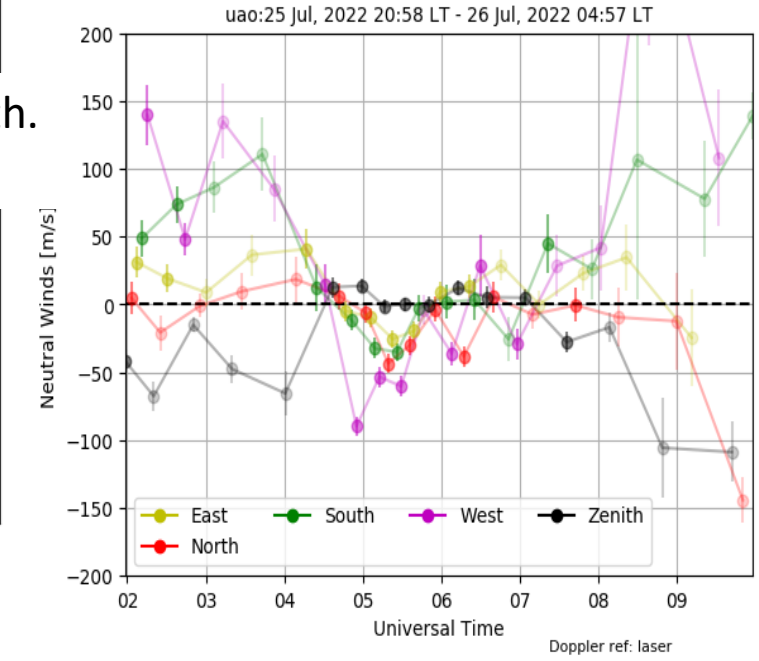

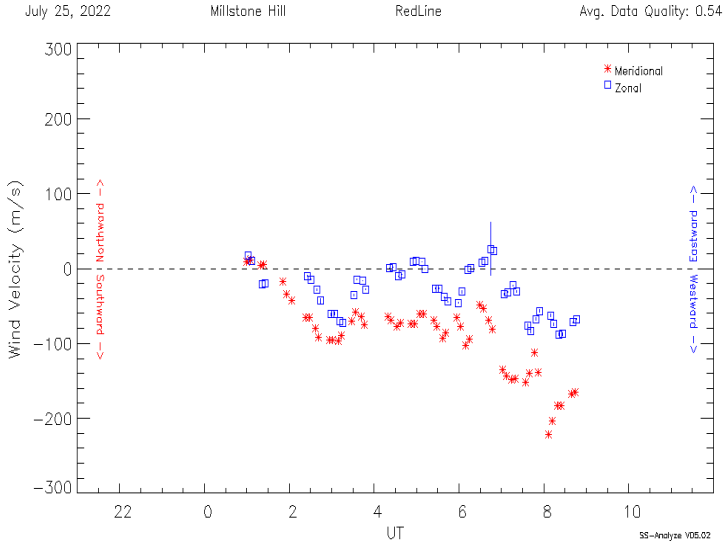

N-S-Z data only for this night

JJO results - 27 July 2022

Temperatures

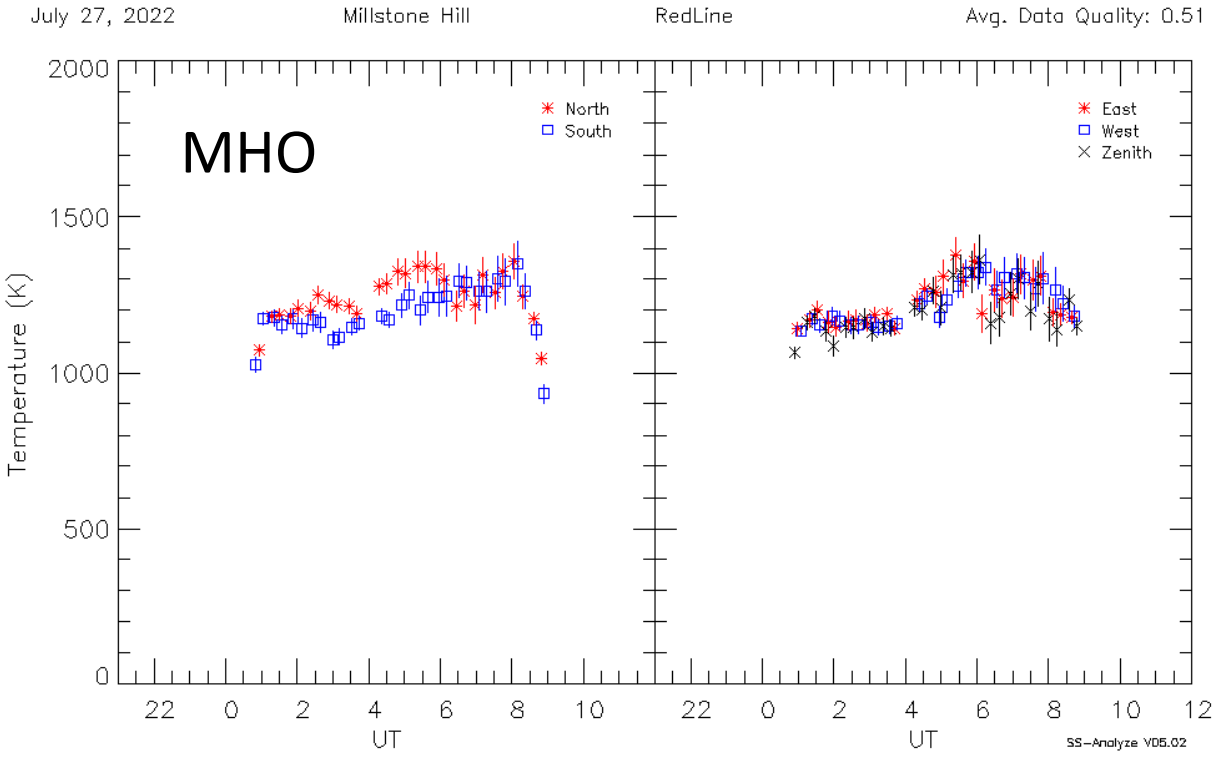

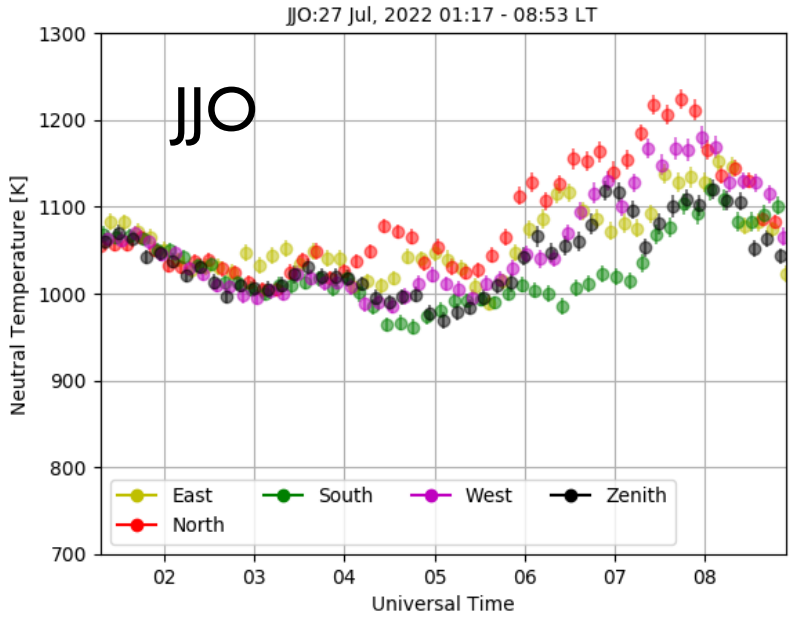

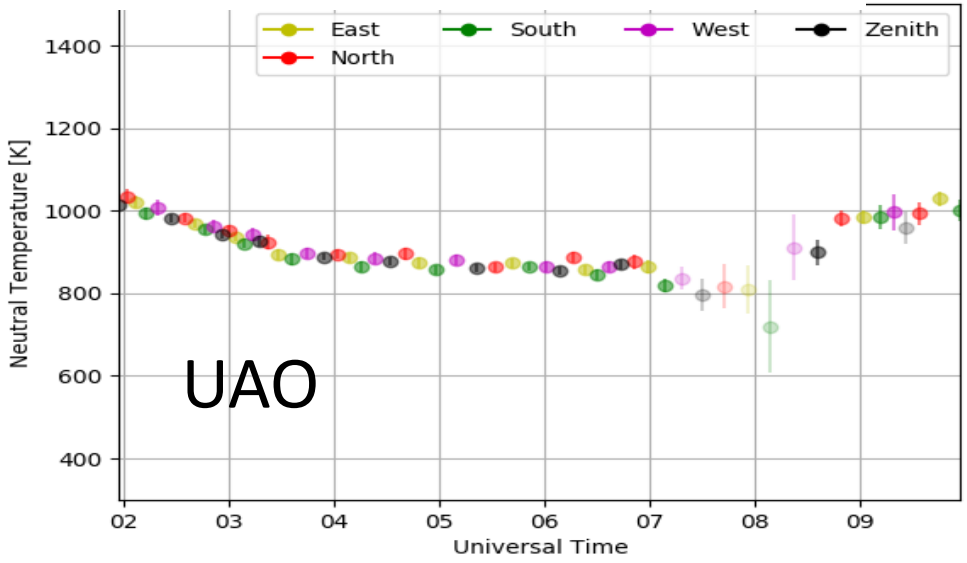

MHO and JJO thermal behavior quite similar but UAO looks to be 100-150 K lower. MHO and JJO data analysis procedures are quite different. UAO and JJO similar.

27 July 2022

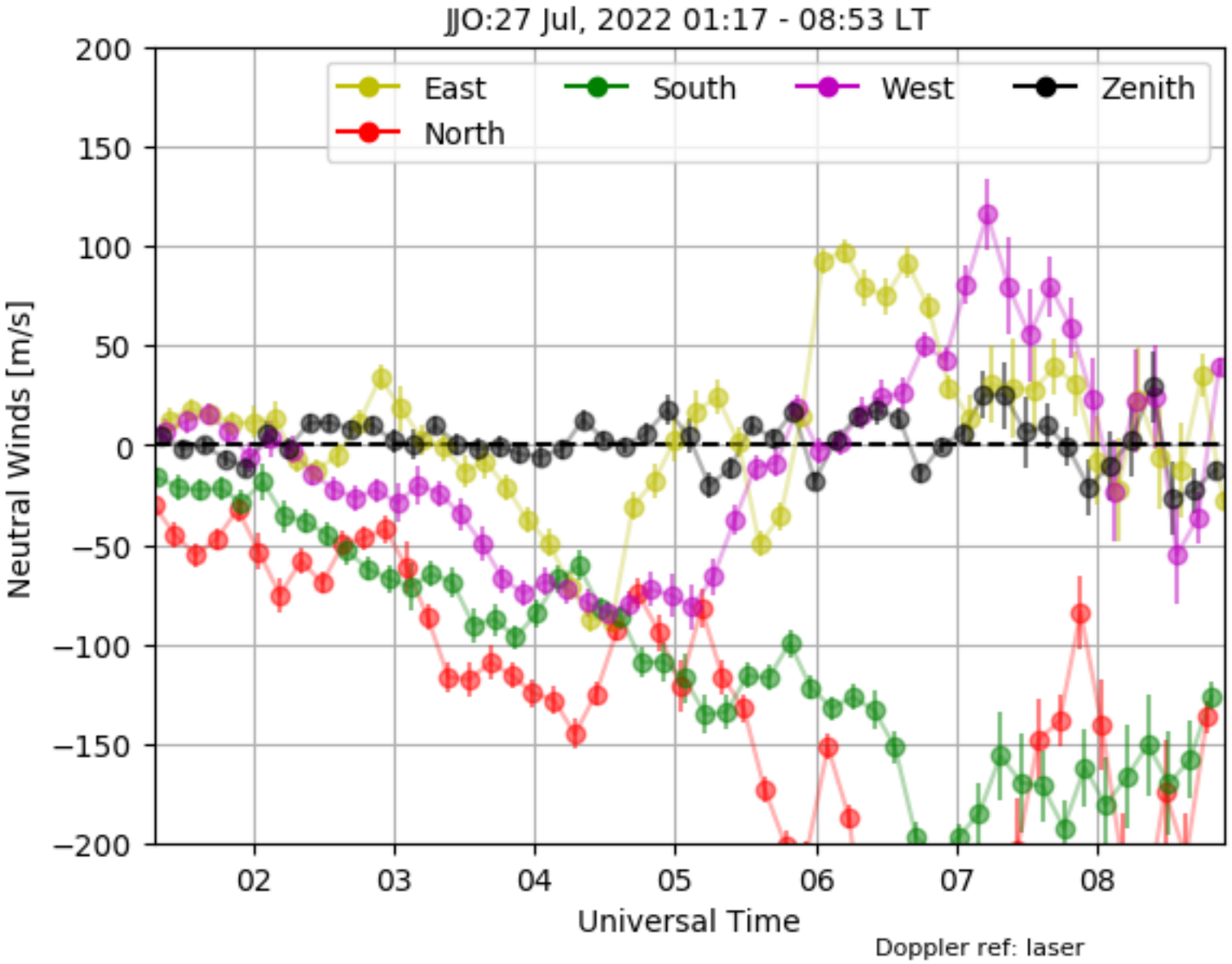

Wind results for JJO on this night are quite interesting

Typical meridional winds to the south throughout the night

Zonal winds to the west during evening period of 02 UT to 04 UT. Quite unusual and suggest response to ion drag caused by westward moving plasma as in the auroral zone.

Results for the last night from JJO

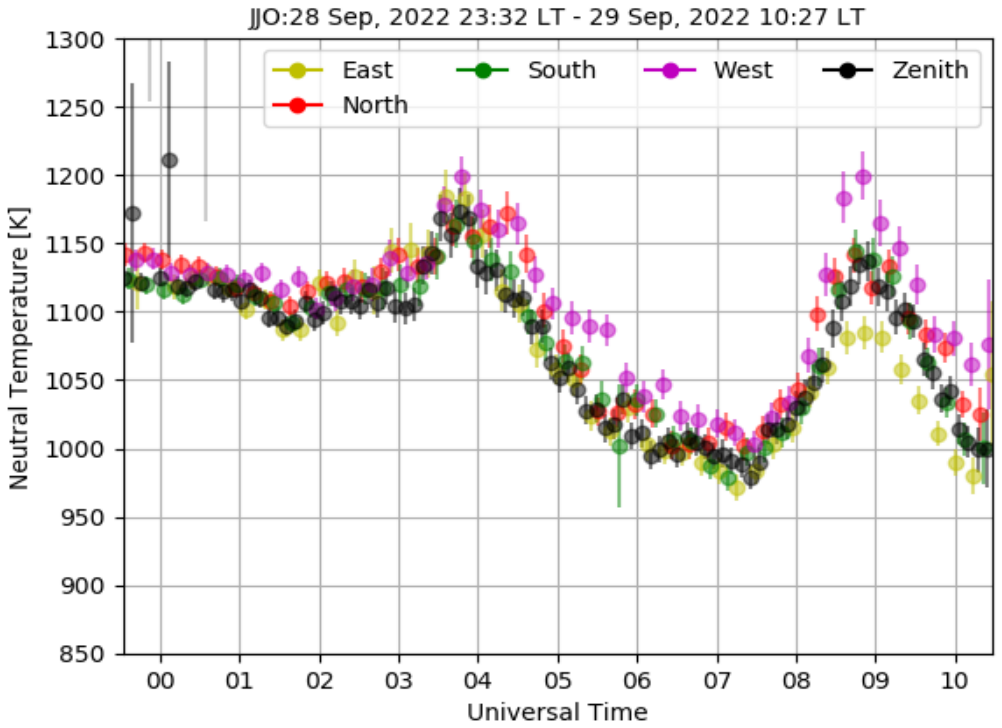

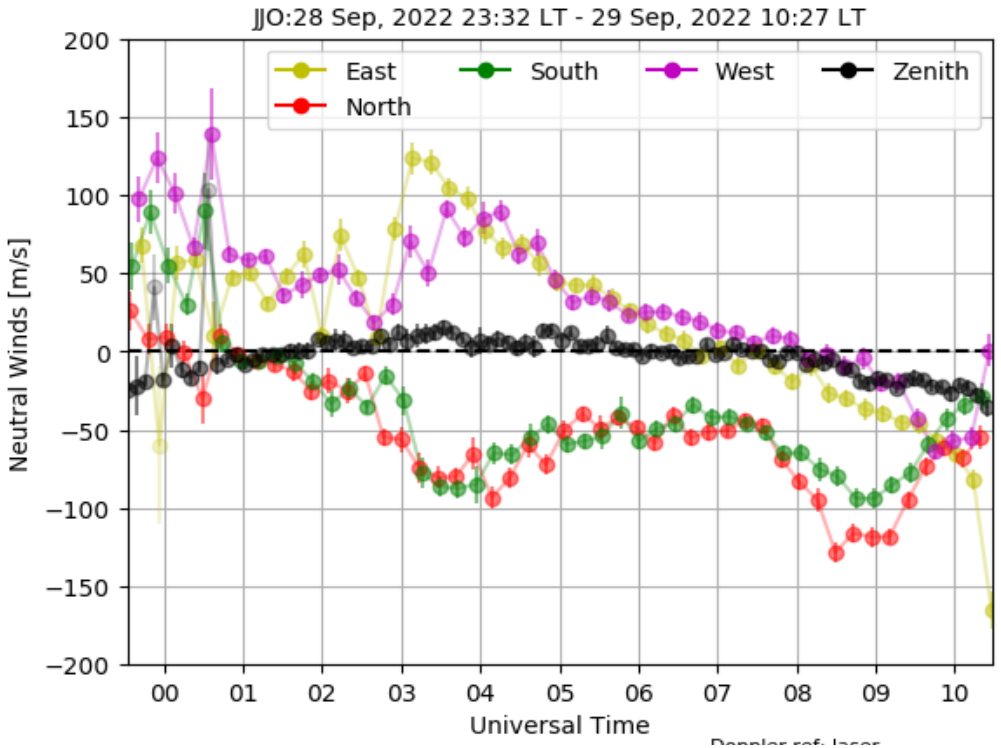

Significant eastward winds seen the whole night until just before dawn

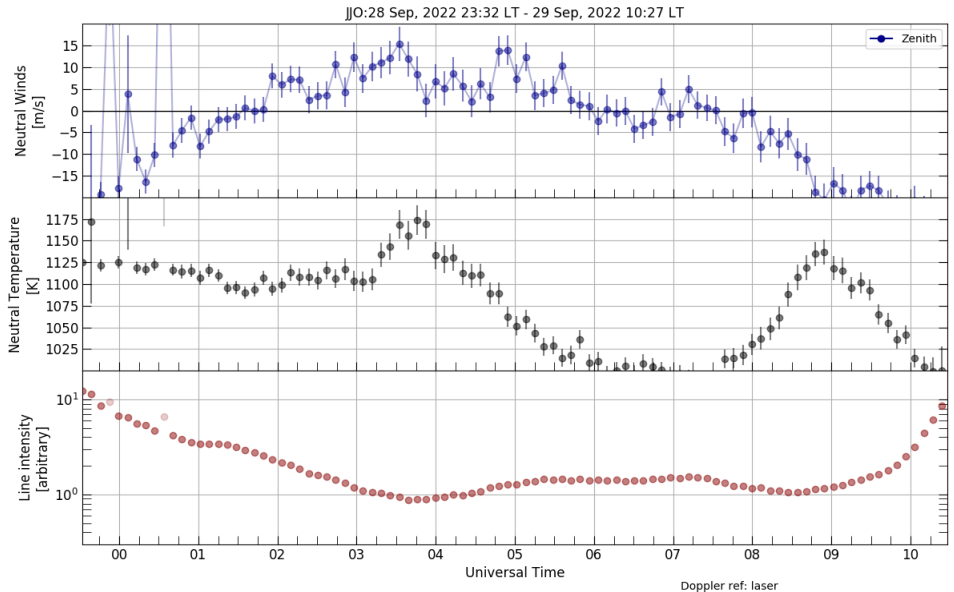

Summary - JJO 630 nm observations

- Much more exploration of vertical winds at JJO to be done, especially to explore whether the Burnside relation holds for mid-latitude locations.
- JJO has successfully detected what looks to be gravity wave features in the zenith for at least two nights.
- Tentative plans are for JJO to return to JJ next year during the spring

JJO was also successful in obtaining 732 O^+ spectra by using the filter wheel to observe the O^+ metastable emissions of this doublet auroral feature during twilight.

The sensitivity proved also to be sufficient to observe the OH 731.6 nm emission – doing mesospheric winds with OH is feasible

Will provide background review before showing spectra.

Introduction to 732 O^+ studies

- Twilight observations of 732-nm emission intensity of O^+ (^2D-^2P) doublets provide remote sensing means of observing *F*-region [O].
- Excitation of $O^+[^2D]$ state occurs during twilight by photo-ionization of [O] by EUV radiation with λs below 67 nm. In aurora, excitation would be by soft energetic auroral electrons. Production by conjugate photoelectrons also possible.
- Primary loss process is radiation via 732-nm and 733-nm emissions
- Radiative life time of O^2P ~ 5 s
- Quenching takes place by collisions with molecular nitrogen
- High resolution measurements of O^+ spectral profile can be applied to determine:
  - ion drifts (ions immediately move according to EXB forcing)
  - ion temperatures
  - intensities (area under spectral profiles)

Meriwether Search for the Holy Grail in Aeronomy

Interest in 732 nm O^+ emission extending over 50 years

Early beginnings
Ester Dome, Ak

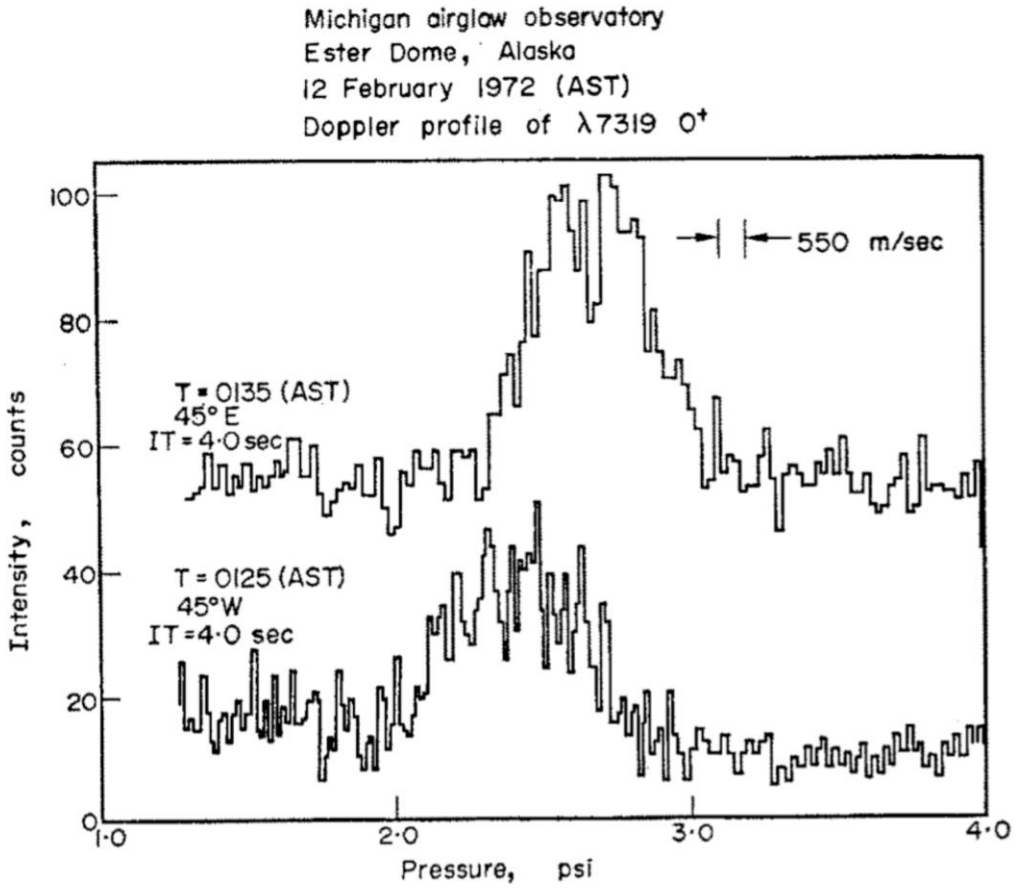

Figure 8. Pressure scanning FPI measurements of the 732-nm emission at Ester Dome in February, 1972. (From *Meriwether et al.*[1974]).

Production of $O^+(2D)$ by two pathways:

- Photo-ionization by EUV photon
- Photo-ionization by energetic electron impact

The OH 731.6 nm emission is a case of good news and bad news.

The bad news is that it contaminates the O^+ emission that we are trying to observe. We can, though, remove the OH contamination.

The good news is that the OH doublet represents a means of Doppler calibration re any field-aligned or horizontal drift motions.

This point will be illustrated below.

Table 2: Spectroscopic data for the two O^+ doublet emissions and adjacent OH emissions (from *Sharpie et al.*[2004]). *The normalized intensity is relative to the sum of all multiplet line intensities.

Emission feature	wavelength (nm)	Normalized intensity*
$O^+(^2P_{1/2}\text{-}^2D_{5/2})$	731.9044	0.14±0.05
$O^+(^2P_{1/2}\text{-}^2D_{3/2})$	732.0121	0.43±0.03
$O^+(^2P_{3/2}\text{-}^2D_{5/2})$	732.9675	0.20±0.04
$O^+(^2P_{3/2}\text{-}^2D_{3/2})$	733.0755	0.23±0.03
$OH(P_{12}(1.5)$	731.621	
$OH(P_{22}(2.5)$	732.915	

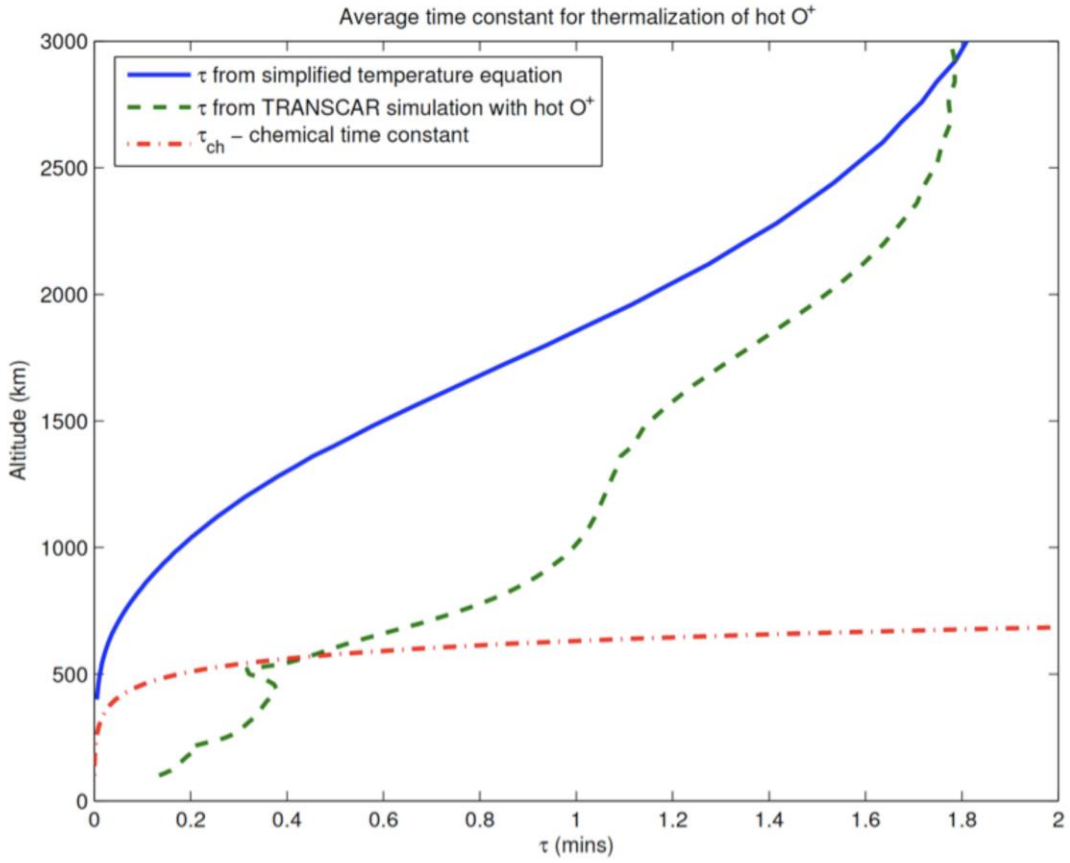

Figure 9. Height variation of the thermalization time (in units of minutes) for hot O^+ (from *Zettergren et al.*[2006]). The TRANSCAR calculations (green) represent the most accurate set of results described in this paper.

The big question is how fast does thermalization takes place given production by either production pathway.

These results suggest that the Doppler width of the O^+ 732 spectral emission would represent the broadening associated with the plasma ion temperature but this needs to be tested.

Thus, the comparison of optical Ti with the radar Ti should be conclusive.

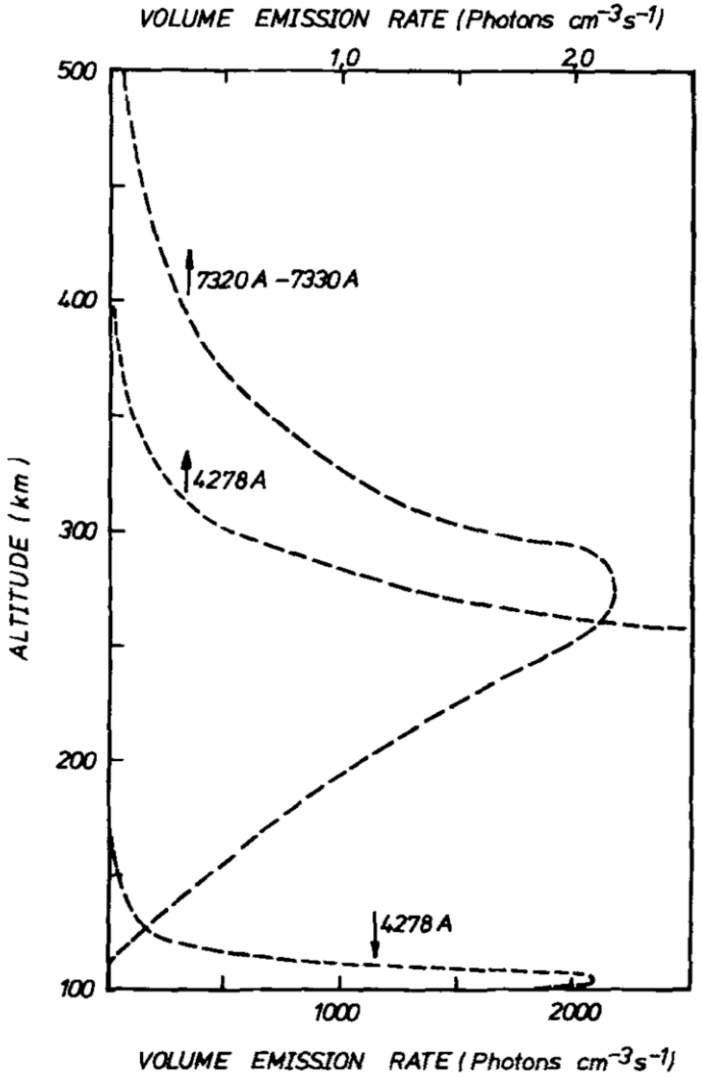

Figure 1. Volume emission profile of 732.0-nm emission in aurora (from *Cogger et al.*[1987]).

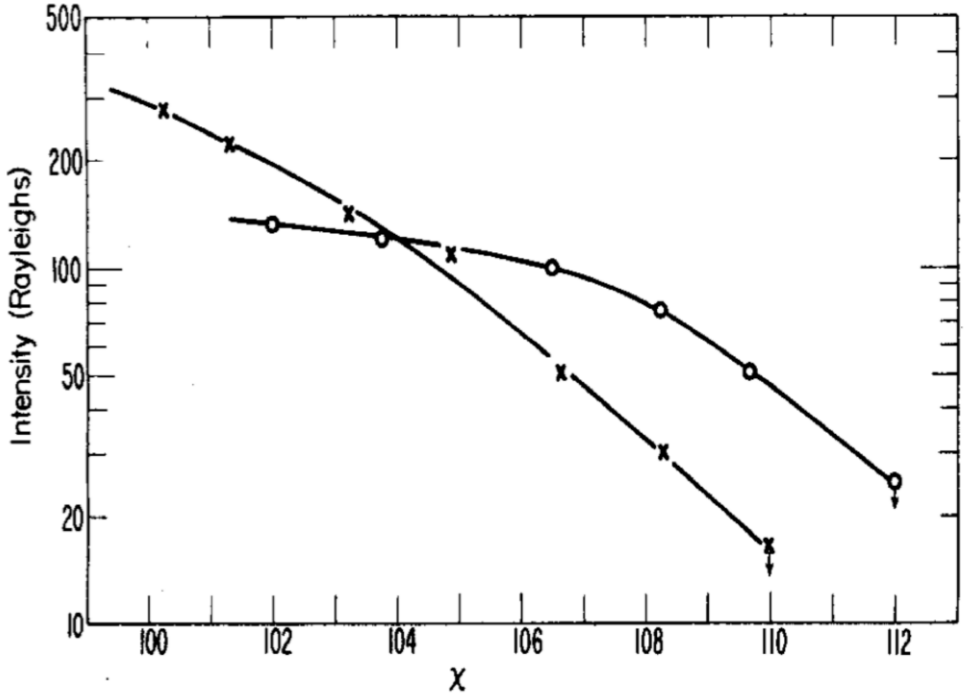

Figure 5: Twilight results at Fritz Peak, CO for a quiet night ("x"s, A<10)) and an active night (open circles, A= ~50) in fall, 1977 (from *Noxon and Norton*, 1979).

Active night implies thermal expansion of the thermosphere so that the [O] density is increased.

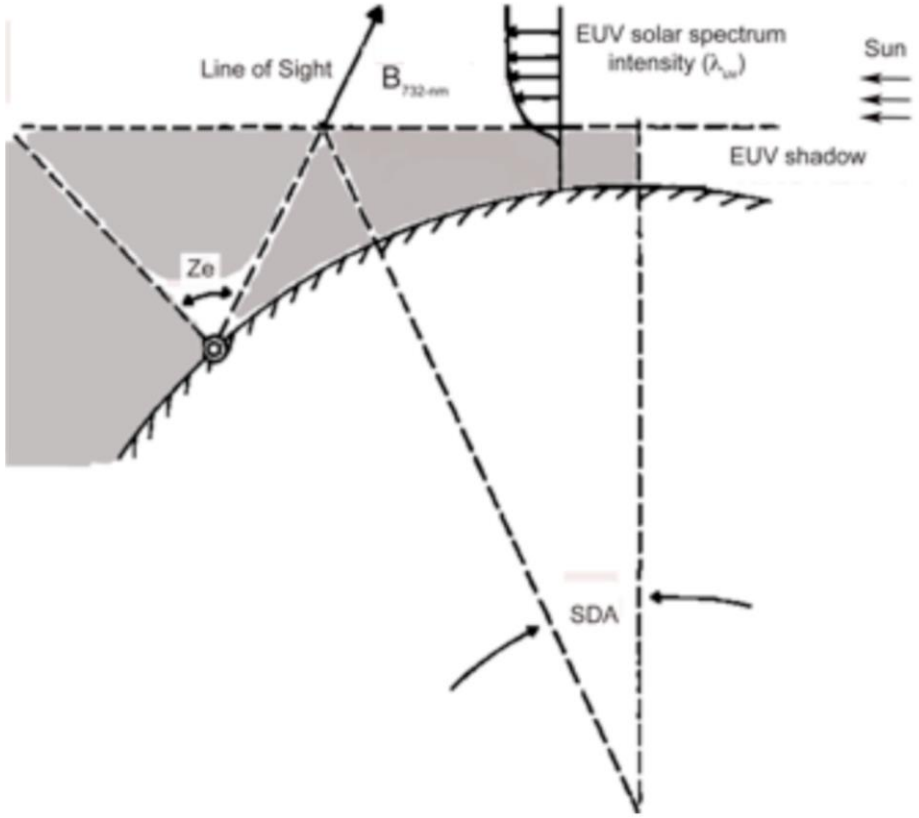

Twilight experiment geometry featuring FPI instrument pointing toward the Sun

← Sun

Svalbard location during the winter period should be quite favorable for twilight observations as the shadow height is relatively low.

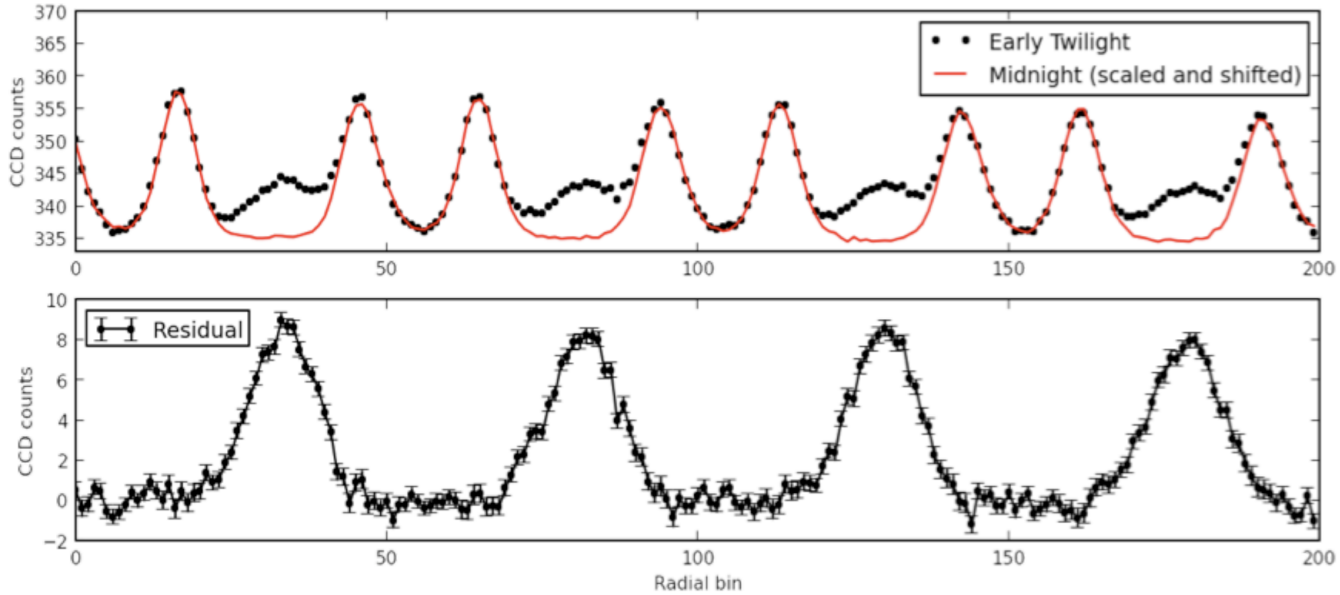

The two OH components are seen here for observations taken with 1.5 cm spacer gap. Origin is lambda splitting – a quantum mechanical effect. Separation well known and can be precisely measured in the absence of the O^+ peaks.

Figure 14: (top) An example of an early UAO twilight spectrum of 732-nm(black) and OH $P_1(2)$ doublet emissions (red) over 4 orders measured in the north direction (elevation, 30º) and zenith (red) on 08/05/2014. The abscissa and ordinate axises are spectral channel and signal after annular integration around the pattern ring center, respectively. (bottom) Residual 732-nm O^+ spectra obtained by sub-traction showing the O^+ spectral profile over four orders.

Doppler observing strategy

The position of the first OH peak in each order represents a Doppler wind marker of zero wind as determined by a separate vertical view of the zenith.

The free spectral range at 732 nm is about 7000 ms^{-1}.

For any line of sight view of aurora from KHO the OH Doppler shift relative to the vertical direction would be maybe a few tens of m/s. The OH vertical wind can be taken to be zero,

This means the offset of the O^+ emission peak relative to the OH peak can be determined relative to a Doppler zero if the Doppler zenith calibration spectrum is considered.

The use of multiple spectra might be required to determine the offset of the O^+ zero Doppler shift marker relative to the OH zero Doppler shift marker. As an example, consider both zonal directions East and West relative to the zenith. Over time the average of the red shifts in one direction and the blue shifts in the opposite direction would give an offset quantity relative to the Doppler position of OH. This would be used to determine the zonal ion drift zero Doppler marker at any other time after this period of calibration.

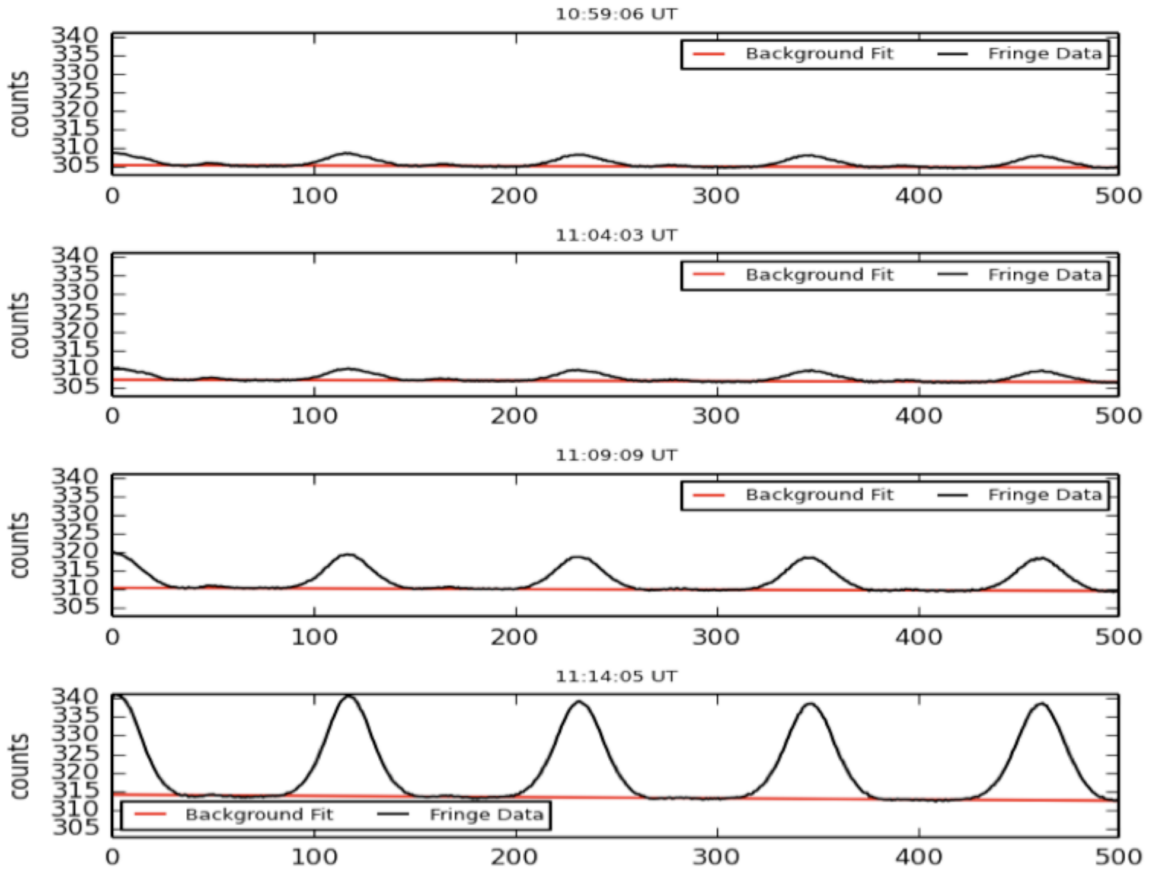

We expect that the auroral signals would be quite bright relative to the OH contamination.

Figure 17. Examples of 732-nm interferometric spectra obtained at Poker Flat in November, 2014. Five orders are shown in this figure with the ordinate indicating the average number of counts for each annular ring. The abscissa is the channel number which is proportional to wavelength. The wavelength interval between order peaks is 0.0297 nm.

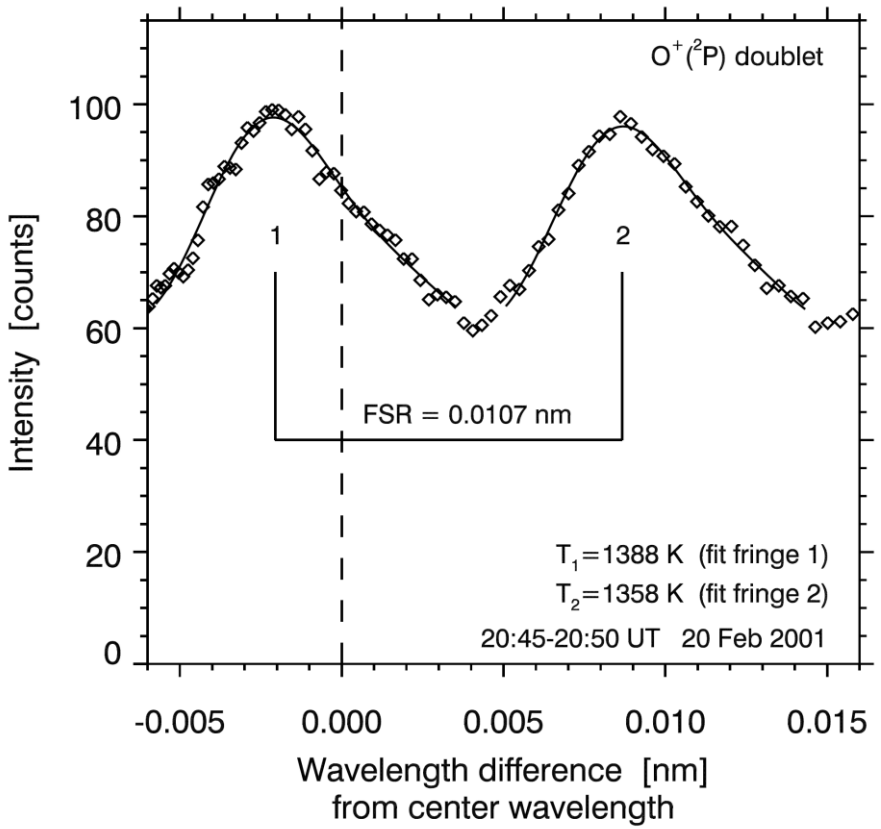

Figure 1. An example of the $O^+(^2P)$ doublet wavelength spectrum for the integration period 20:45–20:50 UT on 20th February 2001. Data (diamonds) and fitted model fringe profiles (solid lines) for first and second fringe doublets are shown.

Results from Cierpa and Kosch (2003) suggest that Ti might be somewhat higher than Tn. It appears that Ti (radar) and Ti (FPI) may be the same.

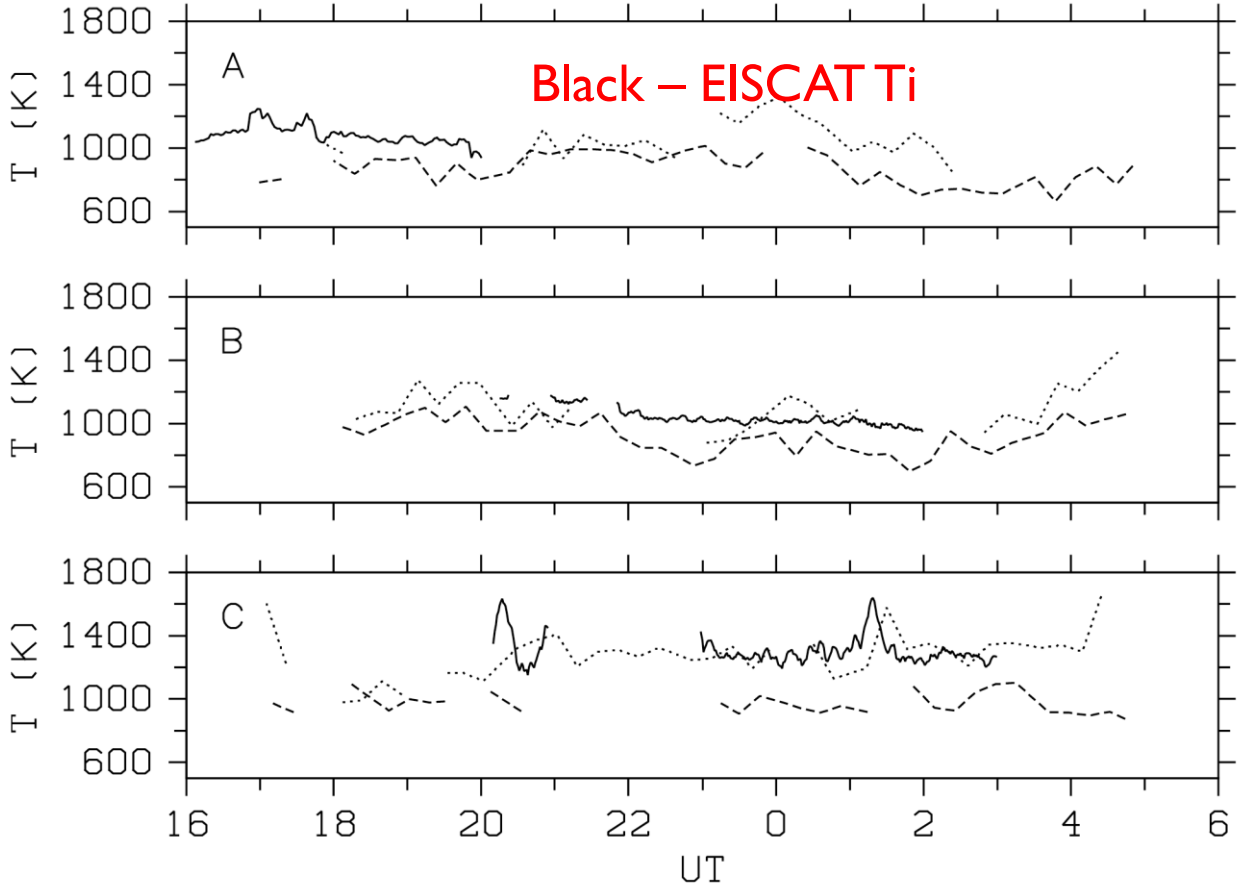

Figure 2. Results from 17th (panel A), 19th (panel B) and 20th (panel C) February 2001. The dashed and dotted curves show the F-layer neutral and ion temperatures from the IFPI, respectively. The solid curve shows the EISCAT ion temperature data for an altitude of 284, 335 and 423 km on the 17th, 19th and 20th February 2001, respectively.

Twilight observations of the 732 doublet emission at Jenny Jump Observatory

After a bit of trial and error we got three clear nights of continual observations of the twilight emission of the O+ emission with a procedure that made the SkyScanner track the Sun. These results not yet analyzed due to need to prepare for shipment to KHO.

The FPI line of sight was maintained at 70 degrees zenith angle while tracking the solar azimuth continuously from the NW to the North to the NE over the range of 5 to 20+ solar depression angles.

Do have results for one azimuth direction that illustrate the decay followed by an increase of the twilight O+ emission.

Early twilight

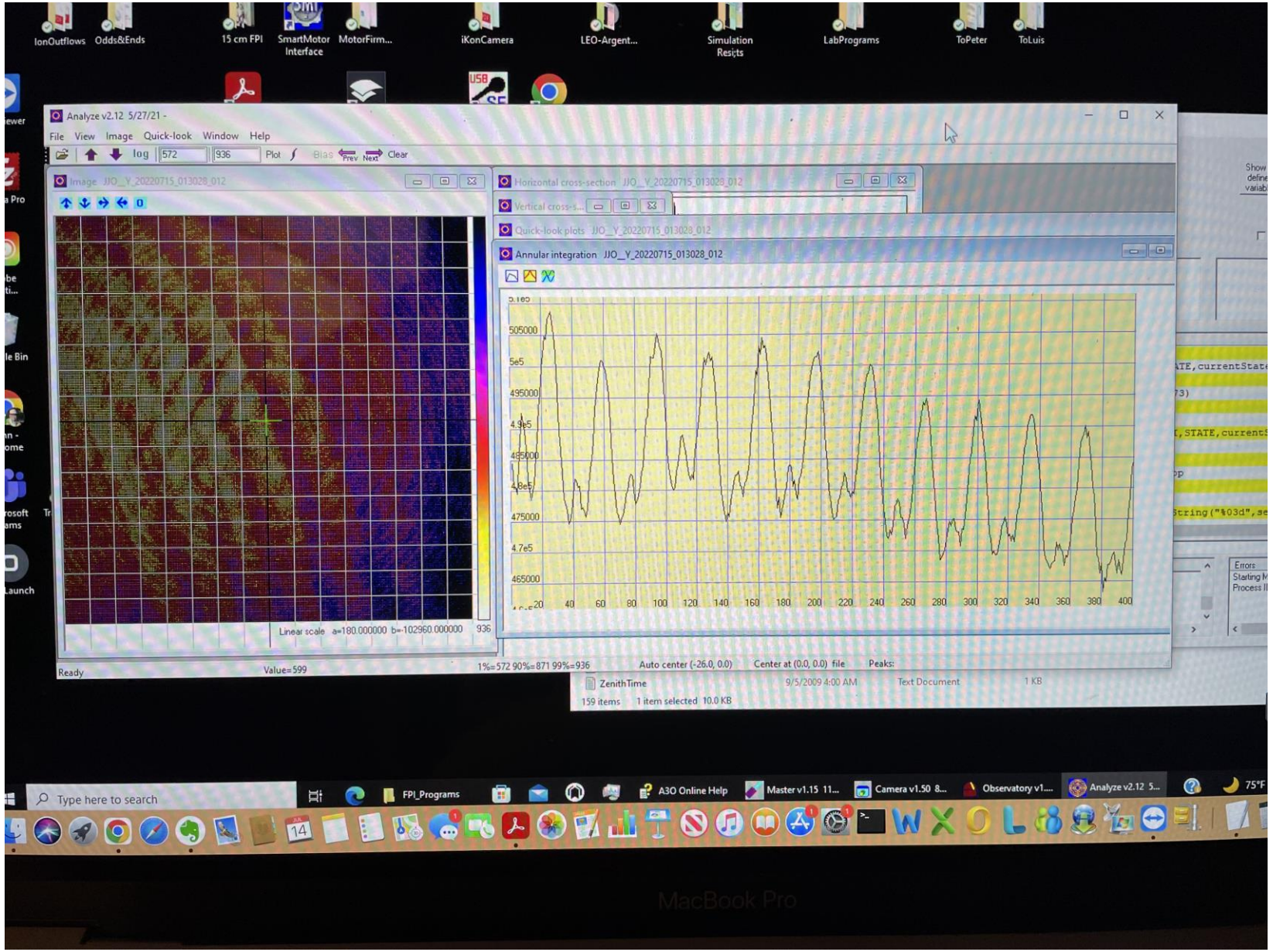

Midway

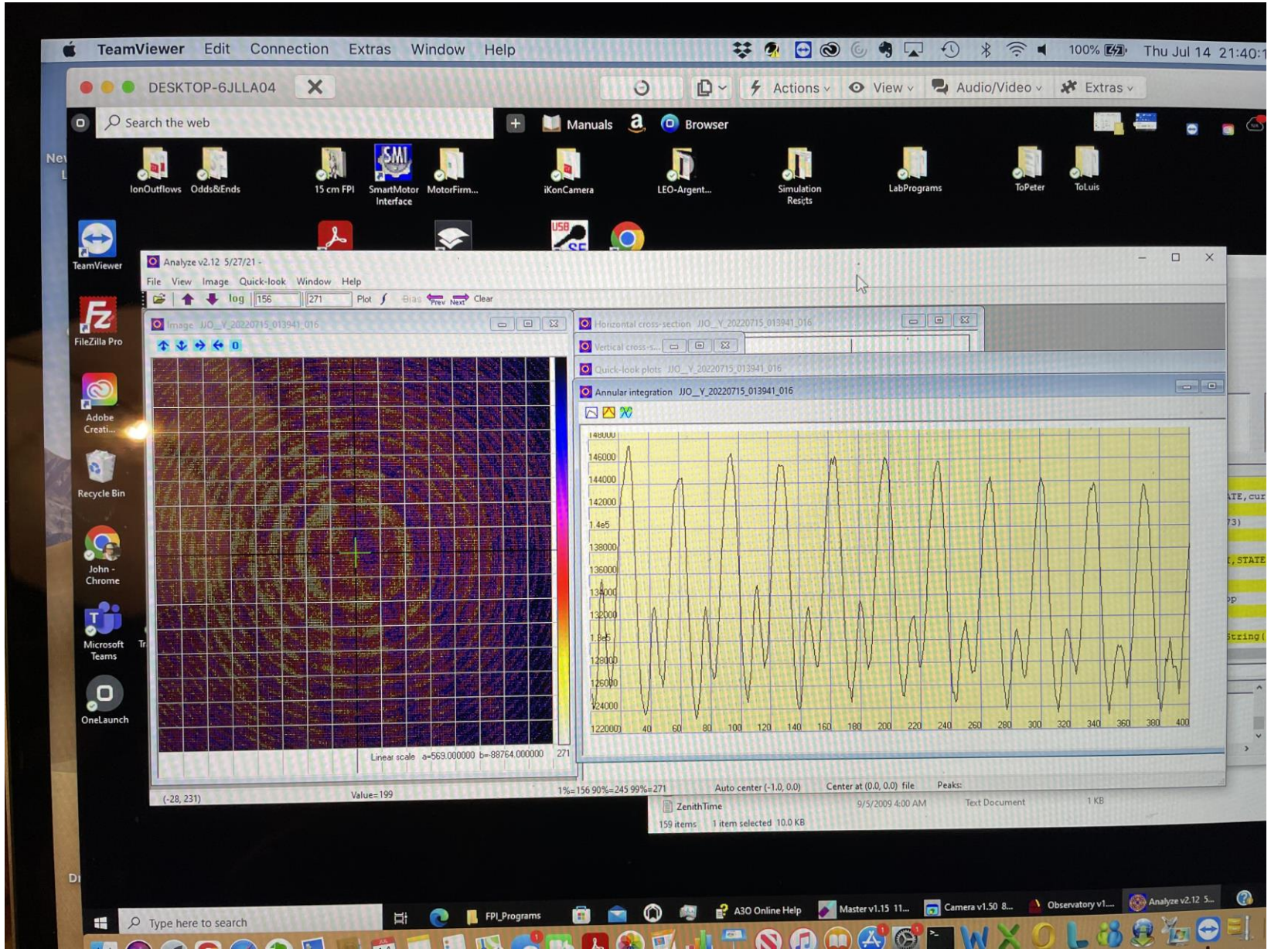
TeamViewer Edit Connection Extras Window Help
DESKTOP-6JLLA04
Actions View Audio/Video Extras
Search the web
Manuals Browser
IonOutflows
Odds&Ends
15 cm FPI
SmartMotor Interface
MotorFirm...
iKonCamera
LEO-Argent...
Simulation Results
LabPrograms
ToPeter
ToLuis
TeamViewer
FileZilla Pro
Adobe Creati...
Recycle Bin
John - Chrome
Microsoft Teams
OneLaunch
Analyze v2.12 5/27/21 -
File View Image Quick-look Window Help
Image JJO__Y_20220715_013941_016
Horizontal cross-section JJO__Y_20220715_013941_016
Vertical cross-s...
Quick-look plots JJO__Y_20220715_013941_016
Annular integration JJO__Y_20220715_013941_016
Linear scale a=569.000000 b=-88764.000000
(-28, 231)
Value=199
1%=156 90%=245 99%=271
Auto center (-1.0, 0.0)
Center at (0.0, 0.0) file
Peaks:
ZenithTime
9/5/2009 4:00 AM
Text Document
1 KB
159 items
1 item selected 10.0 KB
Type here to search
FPI_Programs
A3O Online Help
Master v1.15 11...
Camera v1.50 8...
Observatory v1....
Analyze v2.12 5...

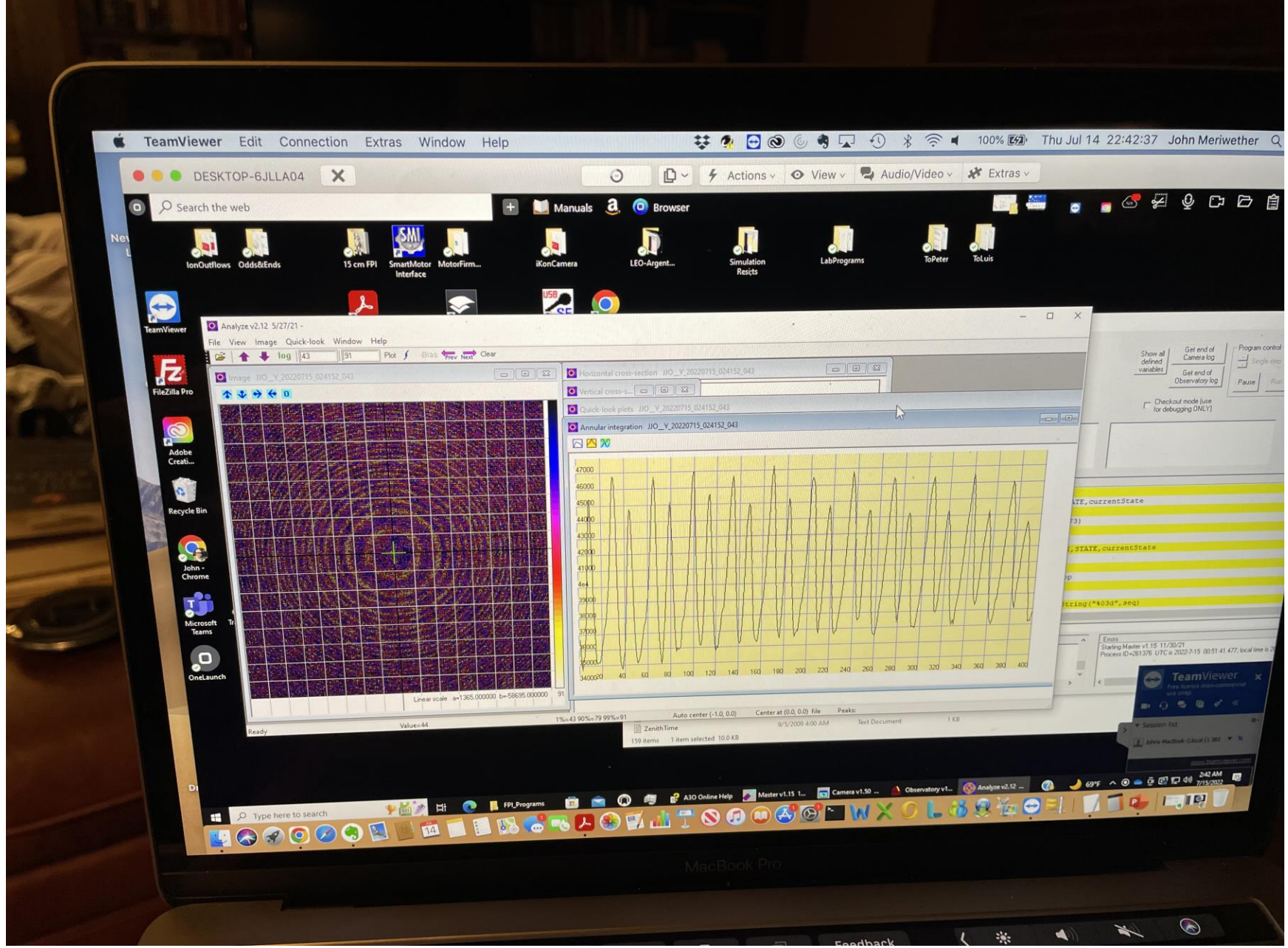
TeamViewer Edit Connection Extras Window Help
100% Thu Jul 14 22:42:37 John Meriwether
DESKTOP-6JLLA04
Actions View Audio/Video Extras
Search the web
Manuals Browser
IonOutflows
Odds&Ends
15 cm FPI
SmartMotor Interface
MotorFirm...
iKonCamera
LEO-Argent...
Simulation Resicts
LabPrograms
ToPeter
ToLuis
TeamViewer
FileZilla Pro
Adobe Creati...
Recycle Bin
John - Chrome
Microsoft Teams
OneLaunch
Analyze v2.12 5/27/21 -
File View Image Quick-look Window Help
Image JJO_Y_20220715_024152_043
Horizontal cross-section JJO_Y_20220715_024152_043
Vertical cross-s...
Quick-look plots JJO_Y_20220715_024152_043
Annular integration JJO_Y_20220715_024152_043
Show all defined variables
Get end of Camera log
Get end of Observatory log
Program control
Single step
Pause
Checkout mode (use for debugging ONLY)
Ready
Value=44
Auto center (-1.0, 0.0)
Center at (0.0, 0.0) file
Peaks:
ZenithTime
159 items
1 item selected 10.0 KB
9/3/2009 4:00 AM
Text Document
1 KB
Type here to search
FPI_Programs
A3O Online Help
Master v1.15 1...
Camera v1.50 ...
Observatory v1...
Analyze v2.12 ...
69°F
2:42 AM
7/15/2022
MacBook Pro
Feedback

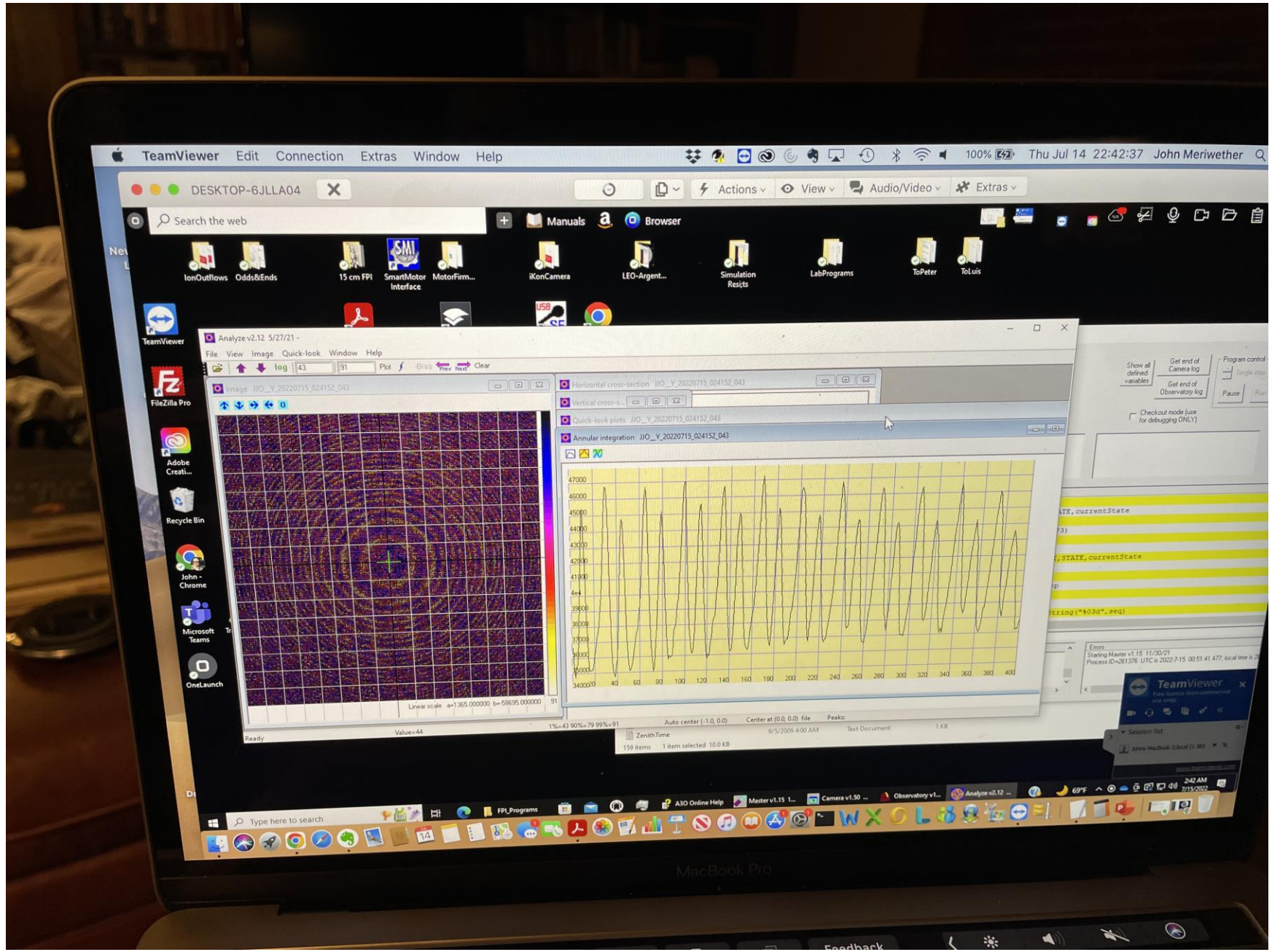
TeamViewer Edit Connection Extras Window Help
Thu Jul 14 22:42:37 John Meriwether
DESKTOP-6JLLA04
Actions View Audio/Video Extras
Search the web
Manuals Browser
IonOutflows
Odds&Ends
15 cm FPI
SmartMotor Interface
MotorFirm...
iKonCamera
LEO-Argent...
Simulation Results
LabPrograms
ToPeter
ToLuis
TeamViewer
FileZilla Pro
Adobe Creati...
Recycle Bin
John - Chrome
Microsoft Teams
OneLaunch
Analyze v2.12 5/27/21 -
File View Image Quick-look Window Help
Annular integration JJO_V_20220715_024152_043
Type here to search
MacBook Pro

Zenith direction, the O^+ emission is gone.

The OH doublet caused by lambda splitting can be clearly seen.

Exposure time is 180 s for each image.

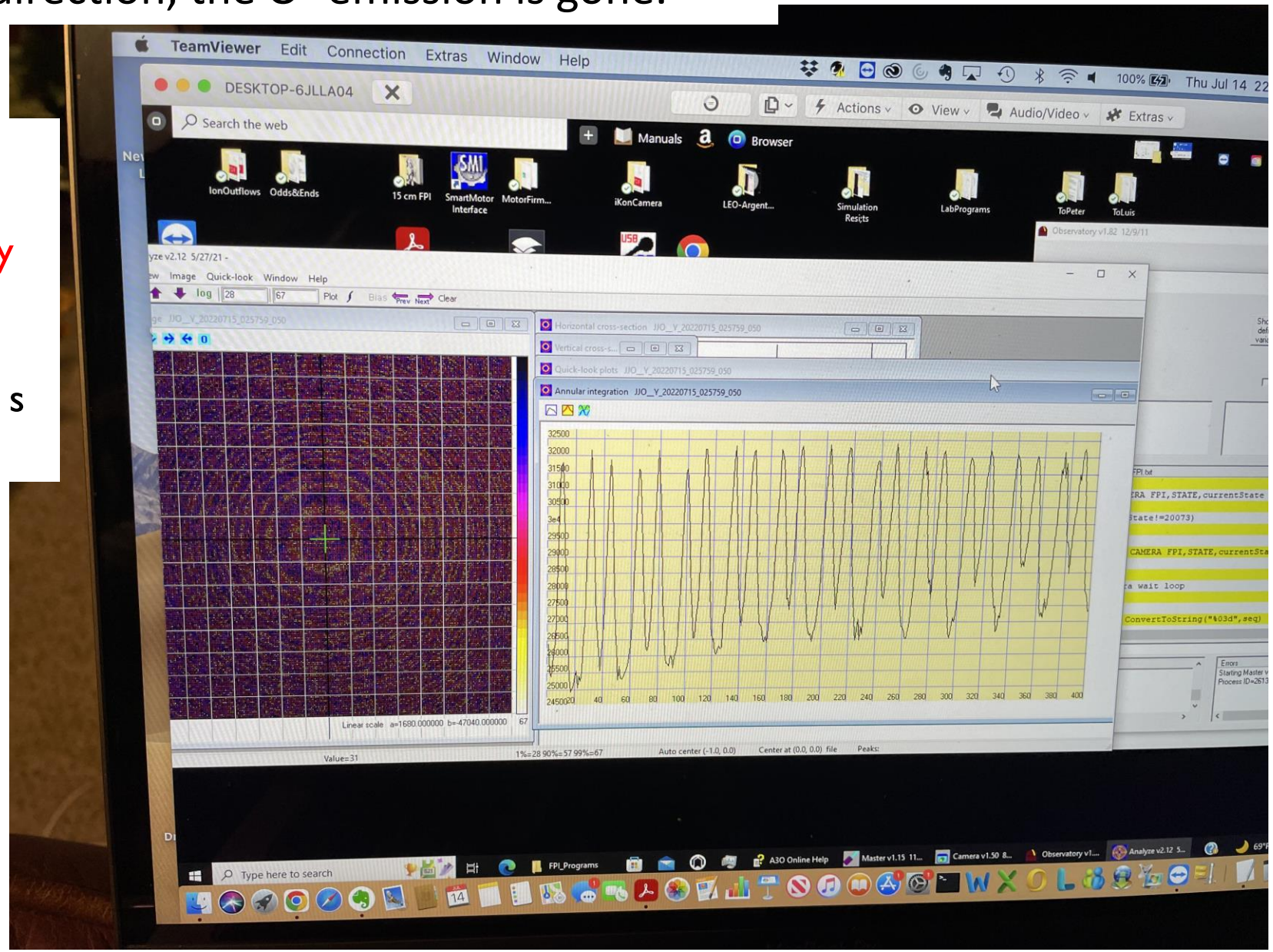

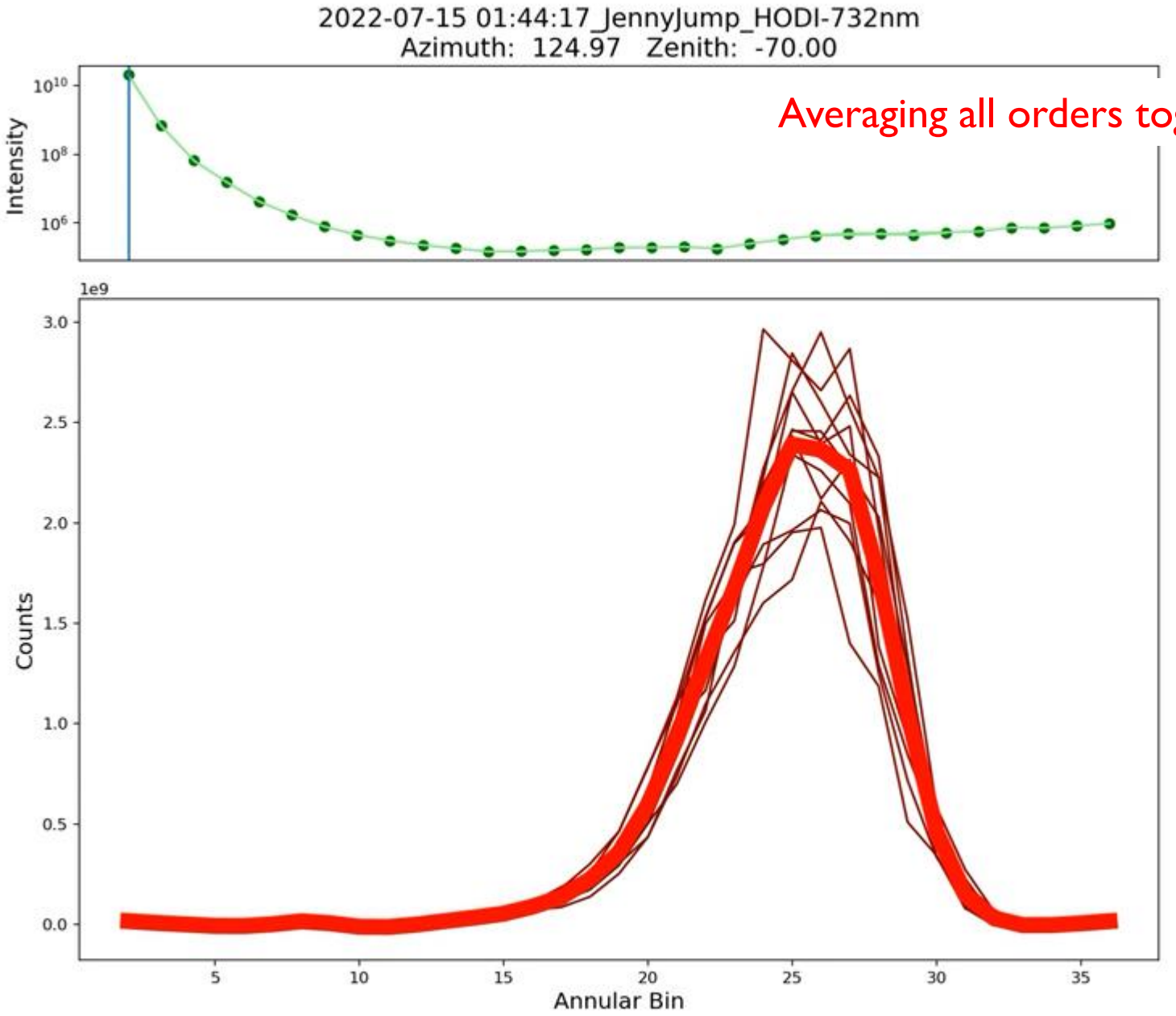

Averaging all orders together

Plans for the future

- Results presented demonstrate we are ready to send the FPI to the Kjell Hendriksen Observatory in Svalbard to observe in the magnetic zenith direction the winds and temperatures of O and the ion temperatures/ion drifts of O^+ in sequence using the filter wheel. Perhaps a cycle of successive 732 O+ images (maybe 3 with 3 min exposure times for each image) followed by 630 O image (60 s). Then, zonal and meridional observations to look for 732 O^+Doppler shifts.

- Future plans after the Svalbard experiment are to relocate back to JJO next spring and eventually to engage in simultaneous observations of 630 nm thermospheric dynamics with observations of exospheric dynamics using a separate FPI designed to observe the Doppler profile of the 1083 nm He emission.

- New MRI award will cover expense of building the He FPI that would be carried out by Keo Scientific, Ltd. A few slides are presented here summarizing these plans.

MaxFPI – instrument designed to observe the He 1083 nm spectral profile

Major Research Instrument proposal was submitted to NSF last January and was selected for funding after receiving excellent reviews.

Instrumental concept organized to achieve FPI maximal sensitivity by two means:

- by increasing the receiving area of the etalon by factor of two, i.e. increase the diameter from 15 cm to 20 cm.

- by using a large format CCD camera (deep depleted) so that we go from 1024 x 1024 (1.27 cm x 1.27 cm) to a 2048 x 2048 pixel (2.7 cm x 2.7 cm). This allows the observations of 4 orders rather than just one.

- Otherwise, the design is much the same as that for HODI.

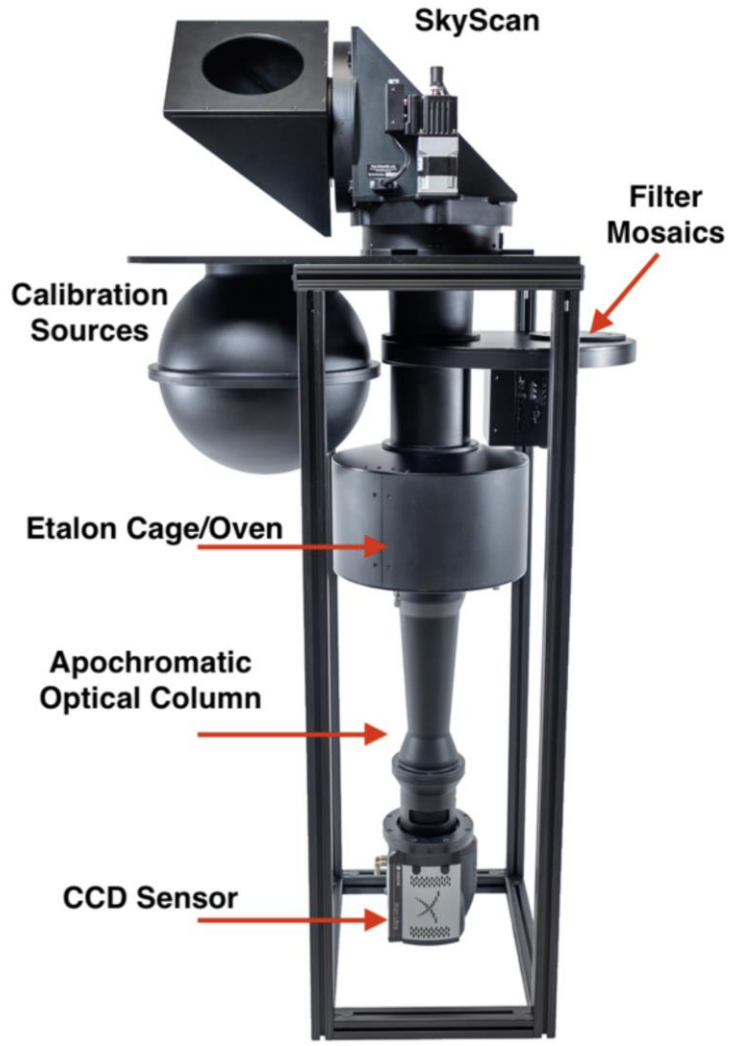

Figure 1. Optical layout of an imaging FPI instrument recently designed and constructed by Keo Scientific, Ltd.

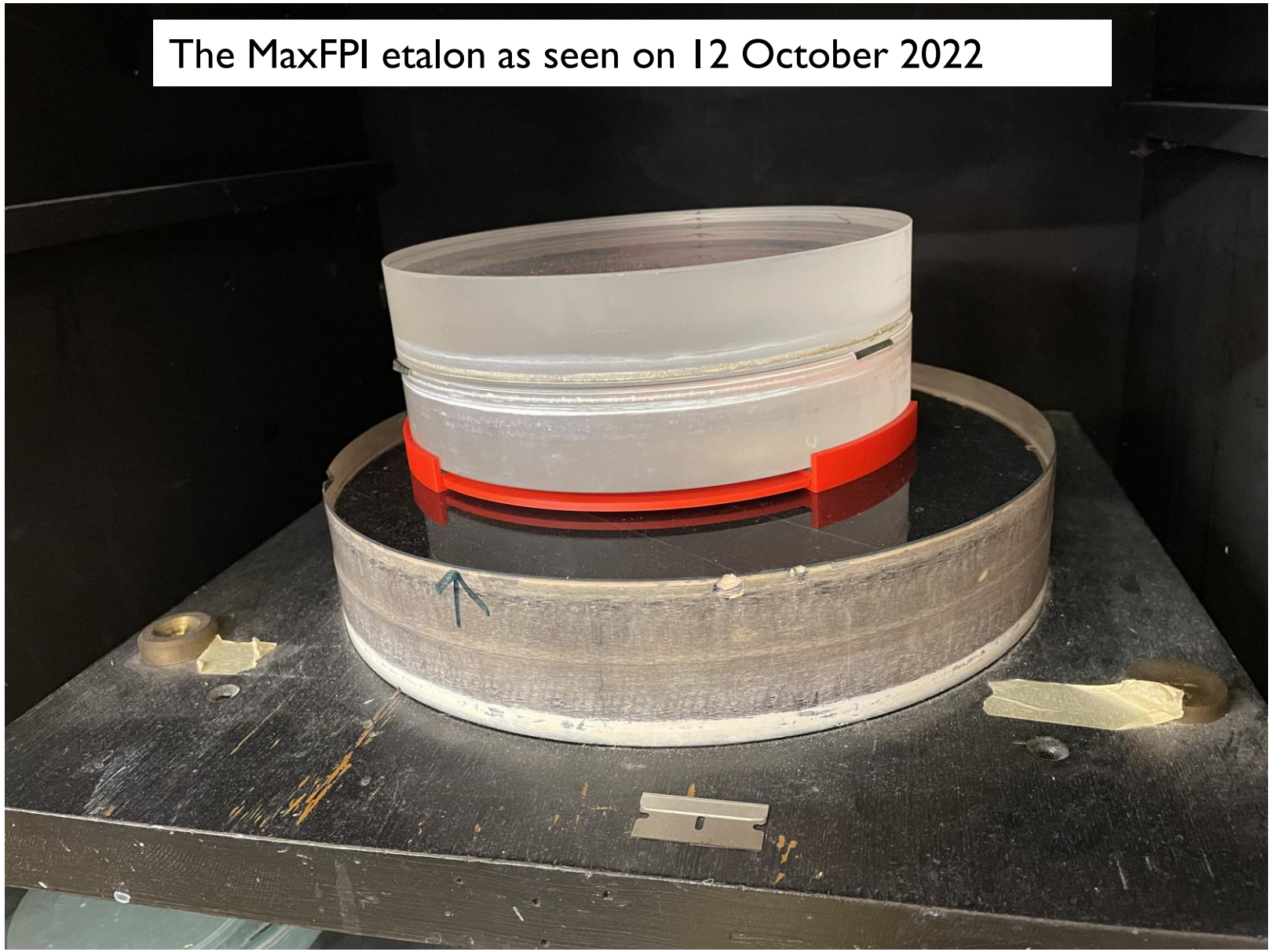
The MaxFPI etalon as seen on 12 October 2022

λ (nm)	Gap (cm)	QE	# of orders	Temp. (K)	Signal (R)	Exposure (s)	Peak (counts)	Back (counts)
He 1083	0.25	1%	3.59	1000	100	300	15,000	1,500
OH 840	0.25	90%	4.63	225	100	30	120,000	17500
O 630	0.25	85%	6.17	1000	20	30	28,000	9,000

Table 1. Listing of parameters used in the forward model calculations for the plots presented in Figure 2. The free spectral ranges for the three wavelengths would be 0.236 nm, 0.141 nm, 0.0794 nm, respectively.

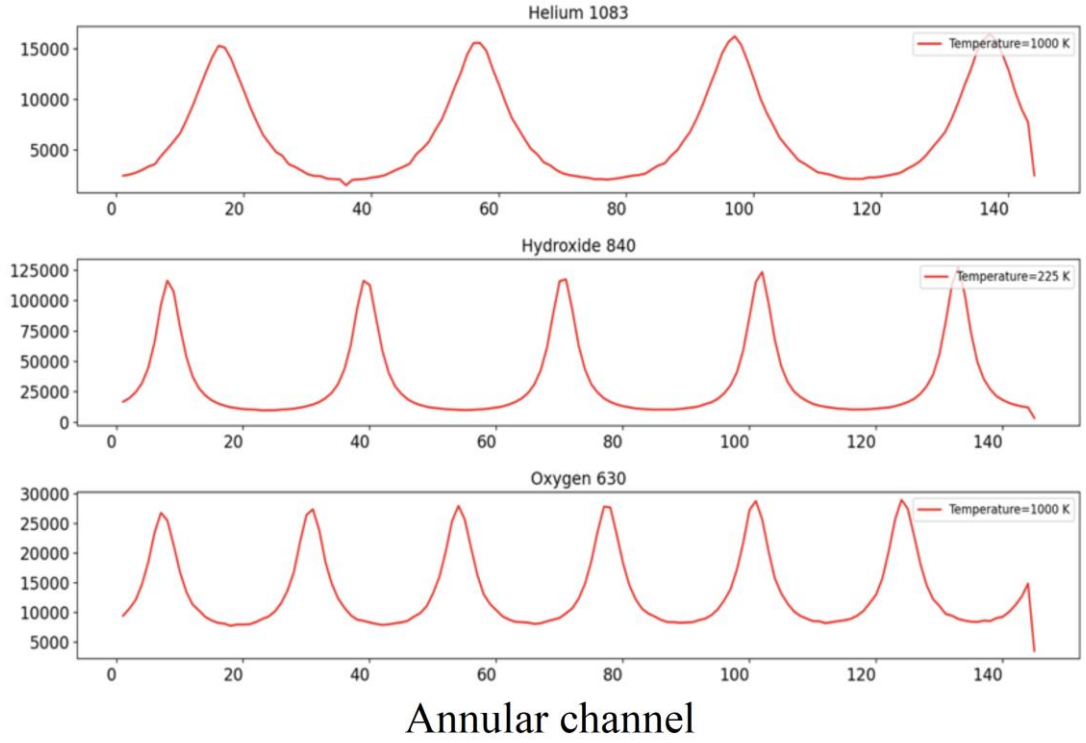

Figure 2. Simulations of He, OH, and O interferograms using parameters as specified in Table 1.

Possibly, we might get a camera that has a higher Q

Calculated spectral Interferograms for He 1083 nm, OH 840 nm, and O 630 nm

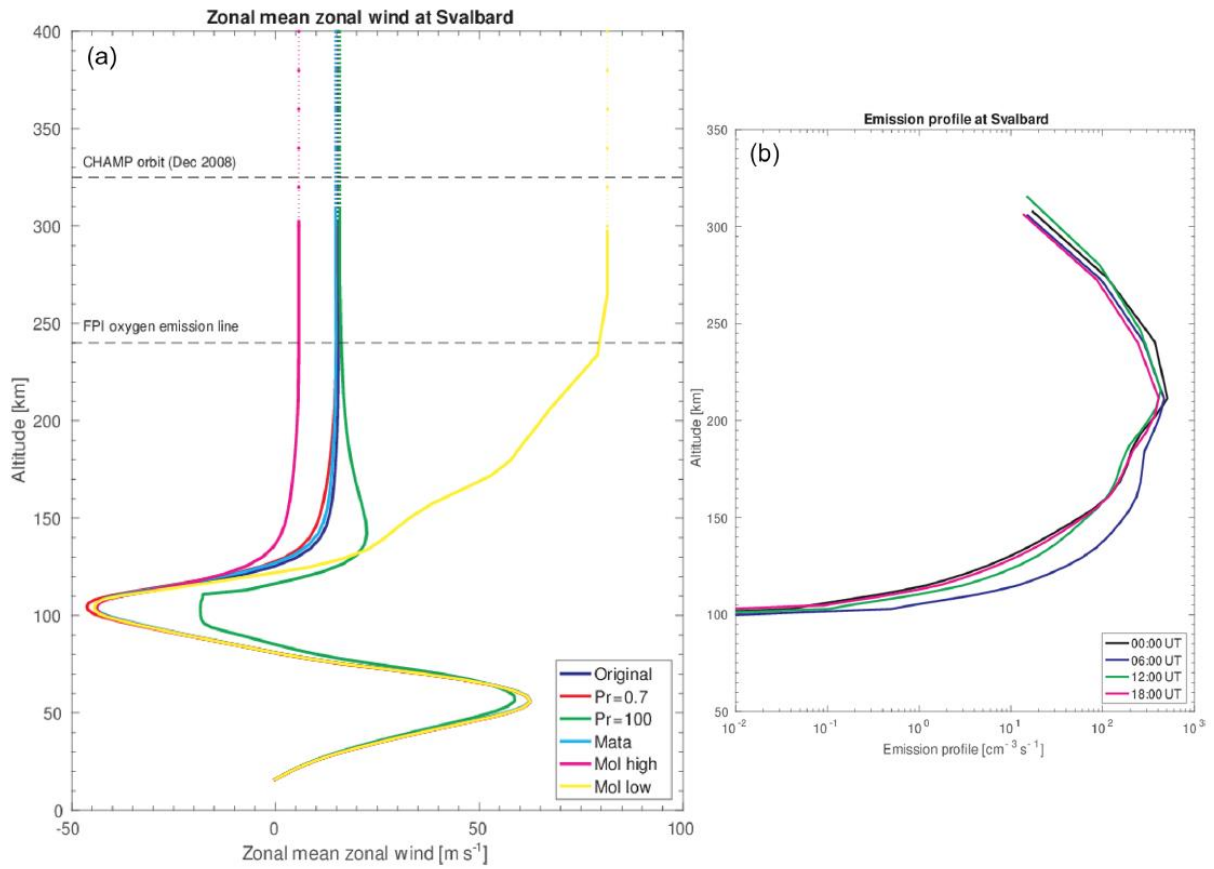

Figure 12. (a) Height profile of CMAT2 zonal winds at Svalbard. (b) Height profile of the red line emission intensity profile from the Vlasov et al. (2005) model.

One motivational factor for MaxFPI was to confirm the finding by Aruliah et al. (2018) that the CHAMP winds are significantly faster than the 630 nm winds for altitudes near 325 km as compared with altitudes near 240 km.

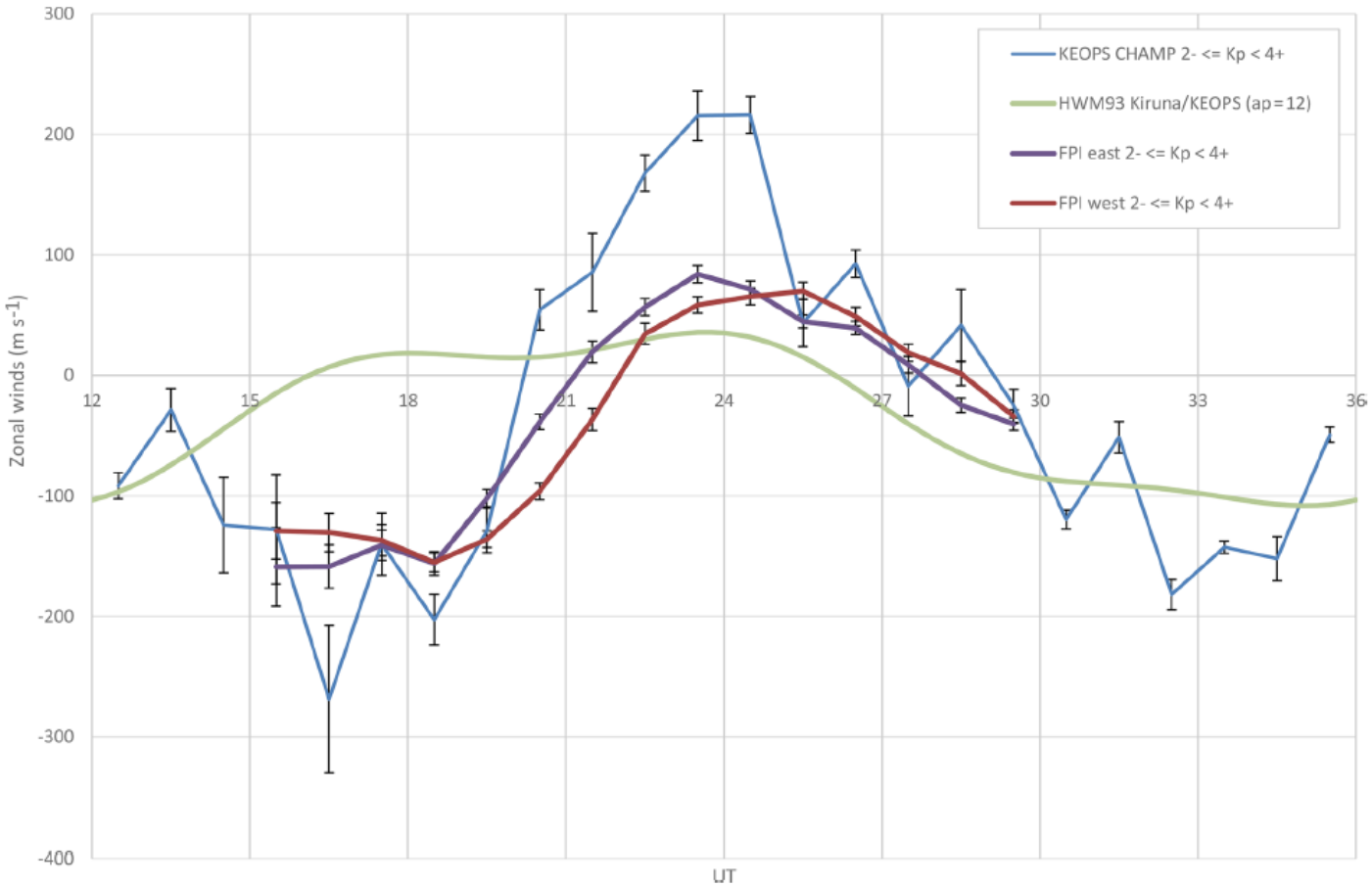

Figure 9. Comparison of CHAMP and FPI measurements of KEOPS zonal average winds to the FPI east and west volumes, including standard errors of the mean, for the winters of 2001–2003. These are compared to the HWM93 model winds.

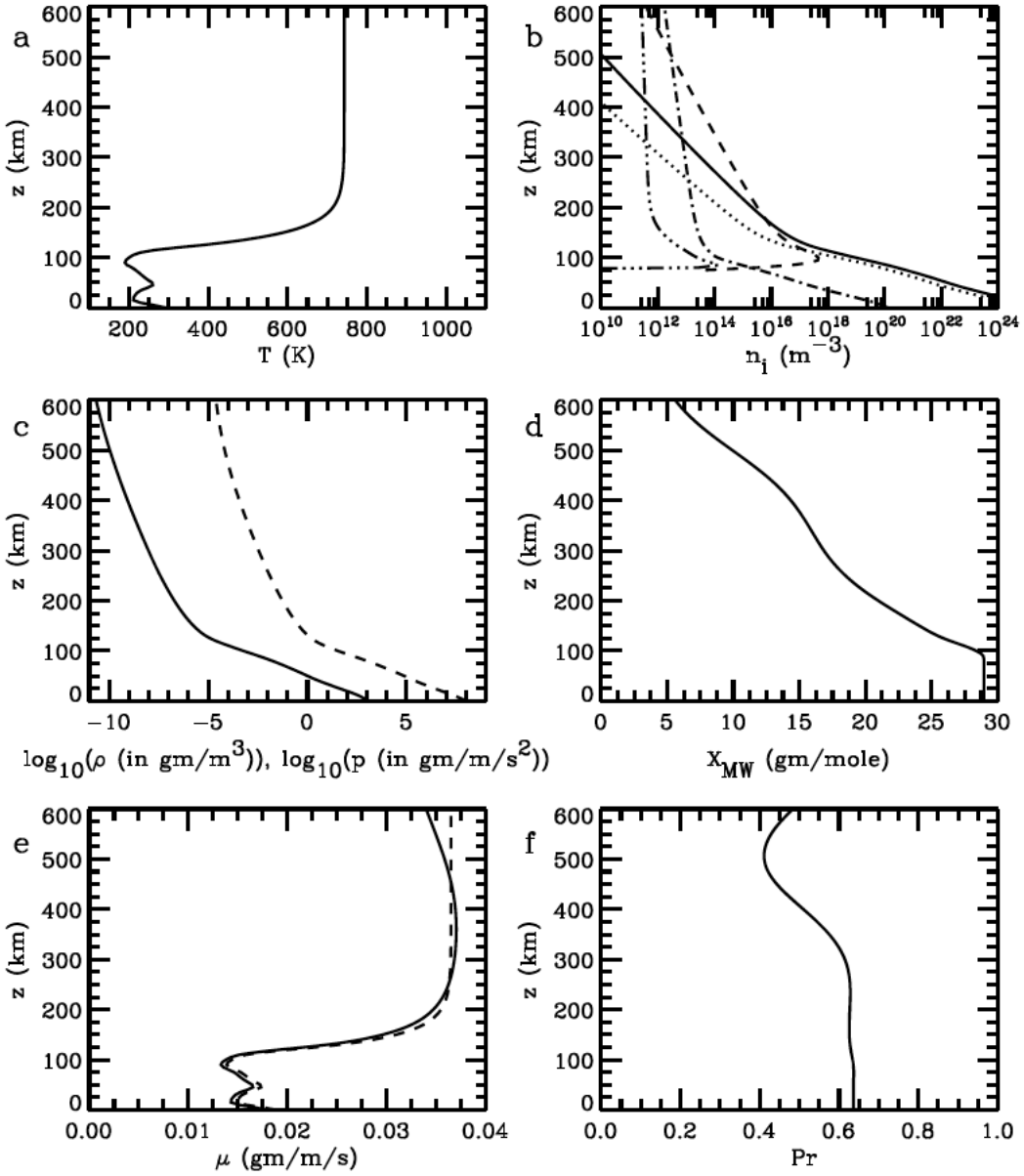

gure 15. (a) MSIS temperature profile on 30 October 2007 at 0415 UT. (b) MSIS number densities of the major spec... $_2$ (solid), n_{O_2} (dot), n_O (dash), n_{He} (dash-dotted), and n_H (dash-dot-dot-dot). (c) $\log_{10}(\bar{\rho})$ (solid line) and $\log_{10}(\bar{p})$ ashed line). Here $\bar{\rho}$ is in gm/m^3, and $\bar{p}$ is in gm/m/s^2. (d) Mean molecular mass X_{MW} in gm/mol. (e) μ from equation (55) sing MSIS number densities (solid line), and μ from equation (46) (dashed line). (f) Prandtl number, *Pr*, calculated from quation (58).

Another motivational factor is the strong indication that the viscosity of the region above 400 km is significantly less than it is for the region below 250 km. Therefore, you would expect faster winds.

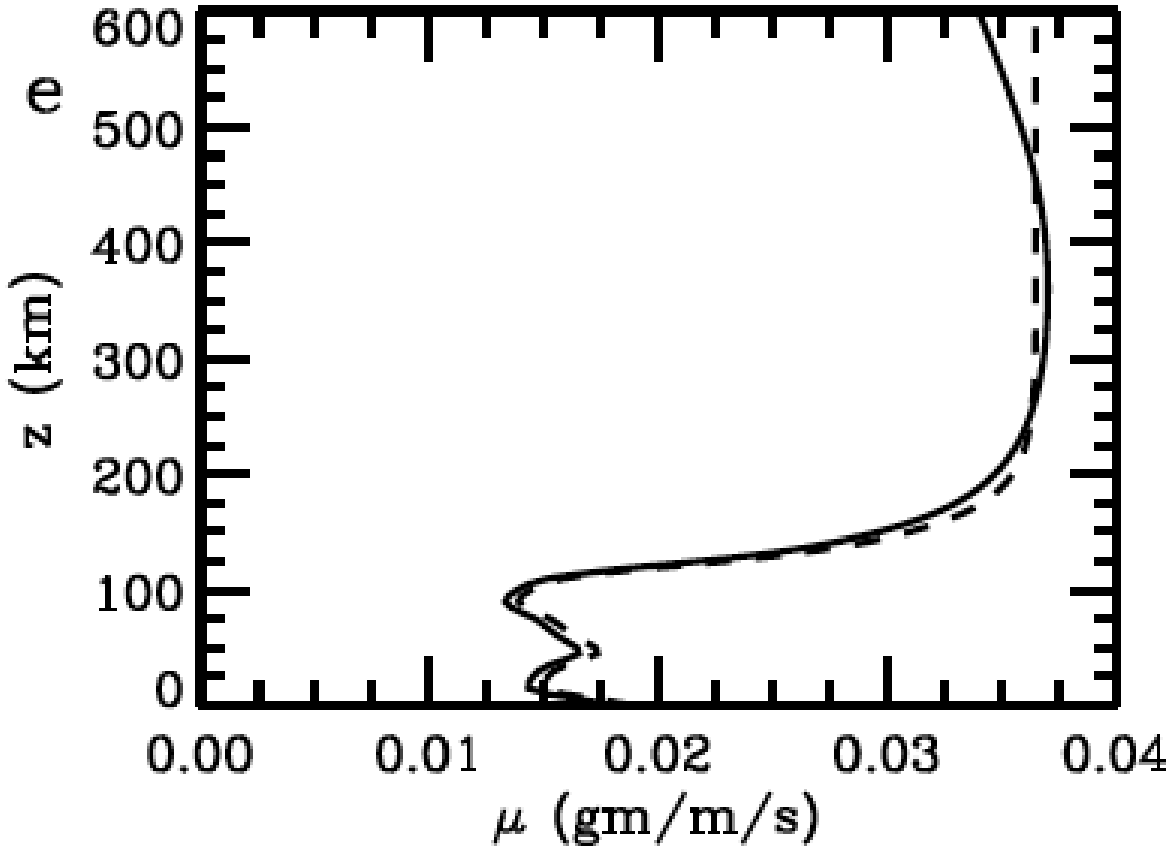

Vadas and Crowley, 2017

Finally, we investigated the possibility that μ might be too large because the *Dalgarno and Smith* [1962] formula for μ only takes into account atomic oxygen. We therefore included all molecular species in the thermosphere using the formula for μ from *Banks and Kockarts* [1973b]. Here we used the number densities calculated from MSIS. We found that the profile for μ was essentially the same up to $z \sim 500$ km, although the Prandtl number *Pr* decreased somewhat at $300 < z < 400$ km. We ray traced the TIDDIBT GWs with this *Banks and Kockarts* [1973b] formula and a slightly smaller *Pr* with and without the the MSIS $\bar{T}$ and $\bar{\rho}$ and found that the results were essentially unchanged from the original results. Therefore, we concluded that including all of the molecular species could not explain the serious discrepancy between GW dissipative theory and the TIDDBIT/rocket data.

In conclusion, we have found that the molecular viscosity, μ, is too large in the middle to upper thermosphere using the standard formulas for μ from *Dalgarno and Smith* [1962] or *Banks and Kockarts* [1973b]. We have found that using these formulas leads to a serious discrepancy between GW theory and the TIDDIT/rocket data. (Note that this conclusion does not rely on the origin of the TIDDBIT GWs (i.e., thermospheric body forces).) We found that implementing an empirical formula with μ decreasing via $\mu \propto \bar{\rho}^q$ with $q \sim 0.67$ (i.e., $\mu \propto 1/d^2$, where d is the average separation distance between molecules) for $z \geq 220$ km yields results that agree much better with the observations. This implies that the kinematic viscosity, $\nu = \mu/\bar{\rho}$, increases less rapidly with altitude for $z \geq 220$ km: $\nu \propto 1/\bar{\rho}^{0.33}$. For $z > 200$ km, $\bar{\rho} \propto \exp(-z/H)$, where H is the neutral density scale height. Therefore, our result implies that $\nu \propto \exp(z/3H)$ for $z \geq 220$ km. Because ν increases less rapidly in the middle to upper thermosphere as compared to μ = constant, it is possible that our result implies that the tidal amplitudes might be different in the middle to upper thermosphere; however, because the tides do not change appreciably for $z > 200$ km when μ = constant, and the decrease in μ only occurs for $z \geq 220$ km, we do not expect the tidal amplitudes to change significantly. Future works will investigate the theoretical understanding and implications for GWs and tides caused by a decreasing molecular viscosity in the middle to upper thermosphere.

Vadas and Crowley, 2017

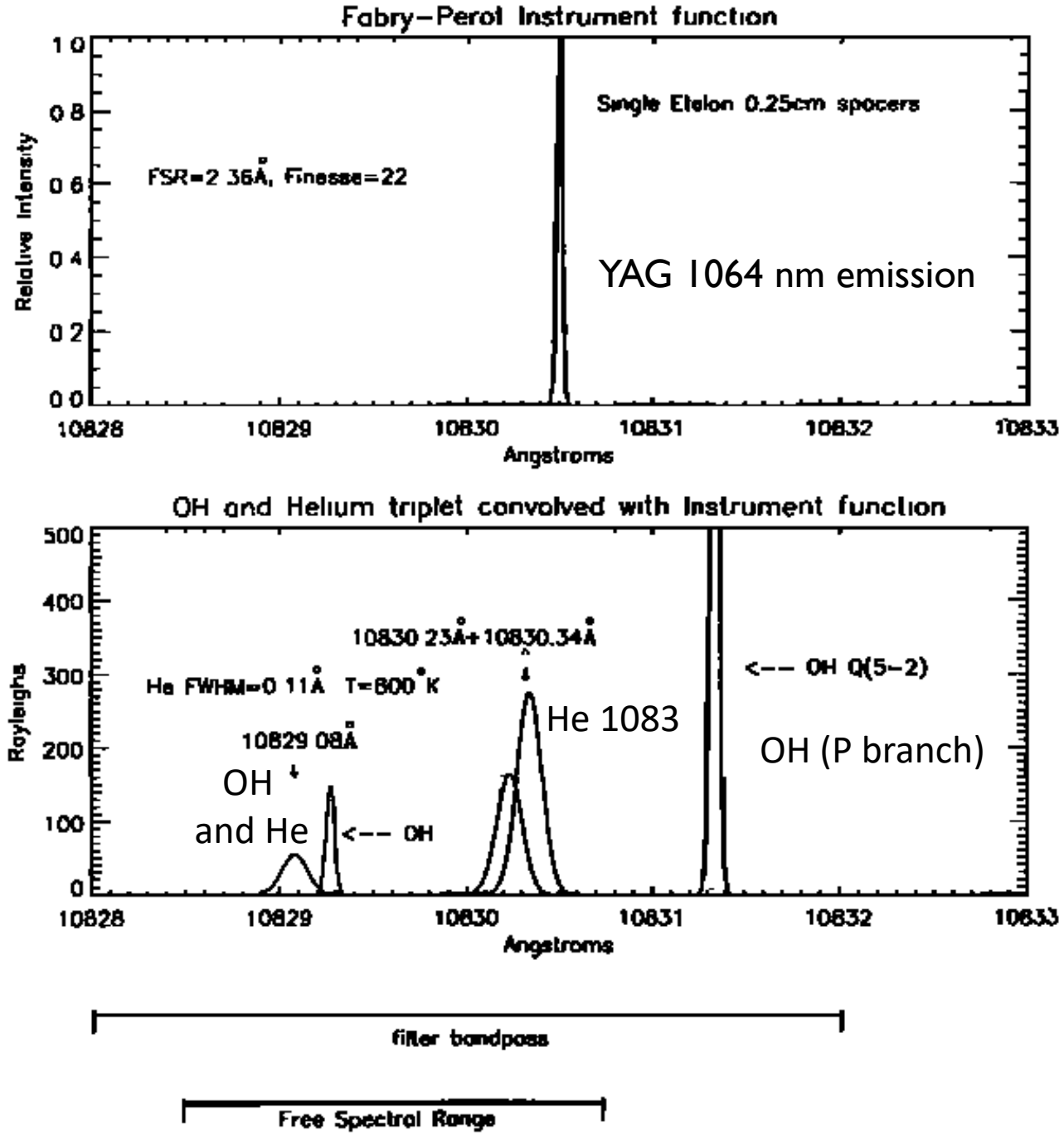

Kerr et al, 1993

Conceptual diagram illustrating the spectral features for the He 1083 nm application.

Spacer gap of 0.25 cm

Waldrop et al.,[2005]

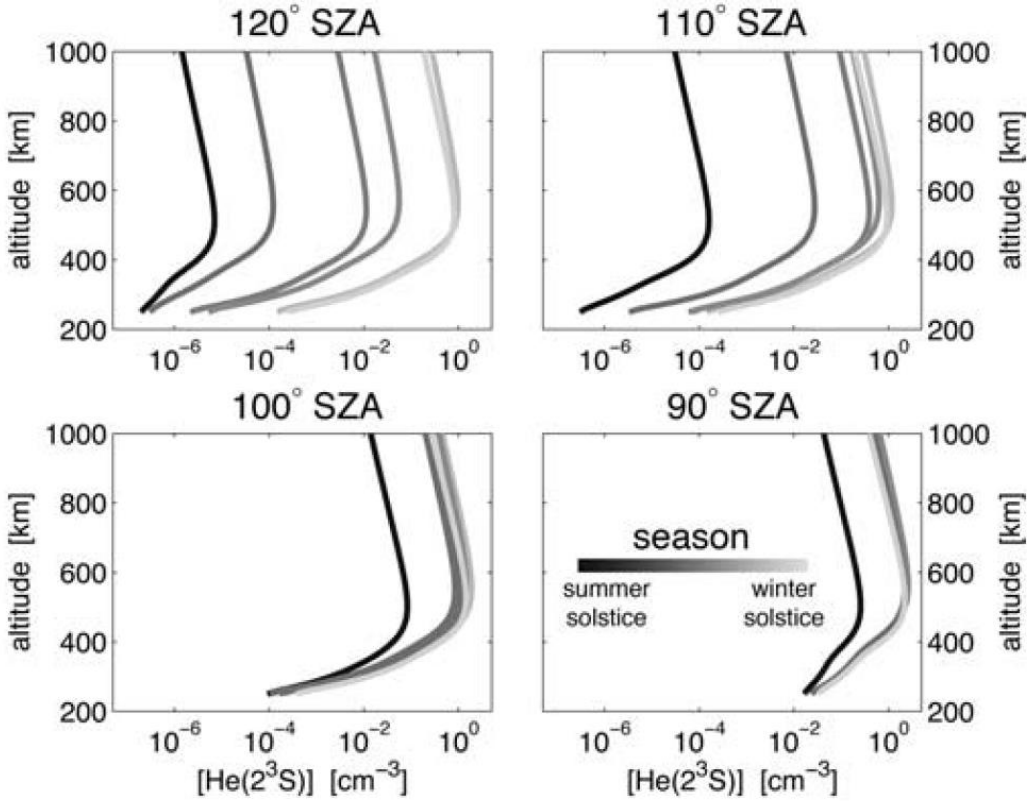

Figure 12. Morning twilight altitude profiles of metastable He density [He(2^3S)] created via photoelectron impact on He as a function of local solar zenith angle and season during the six representative examples of solar maximum conditions listed in Table 1.

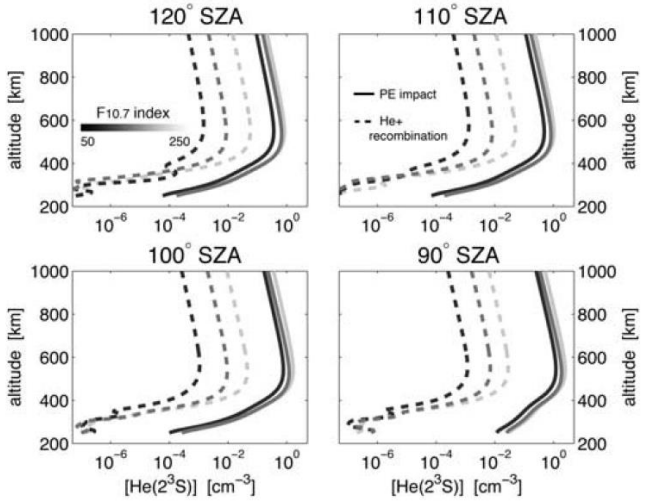

Figure 13. Altitude profiles of metatable He density generated from He^+ recombination only (dashed lines) and photoelectron impact only (solid lines) during morning twilight in January. These three intervals are described in Table 2. Solar $F_{10.7}$ index is indicated by the line color of the altitude profile. The supply of conjugate photoelectrons at large local solar zenith angles ensures the predominance of the photoelectron production source throughout twilight, regardless of solar activity.

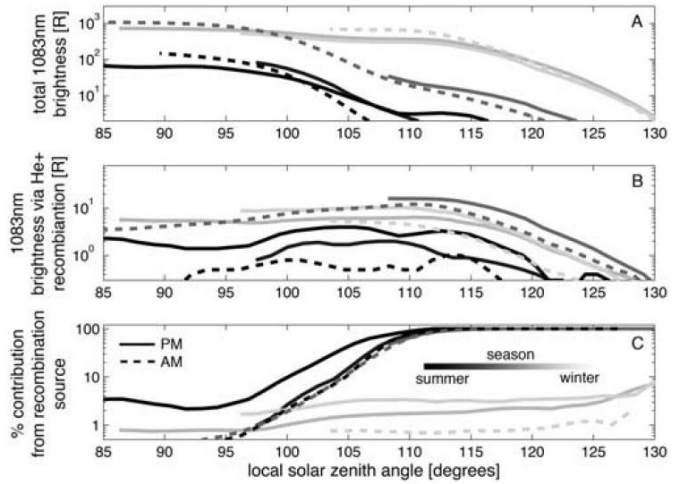

Figure 16. As a function of local solar zenith angle: (a) total 1083 nm brightness, (b) 1083 nm brightness via He^+ recombination only, and (c) percent contribution of recombination source to total 1083 nm brightness. All model calculations shown use ISR data taken in 1998 and listed in Table 3. Line color represents season, defined symmetrically around the solstices. Dashed lines correspond to morning twilight observations, and solid lines show evening twilight results.

Tn_{1083} ESTIMATION

early work:

- assumed Gaussian shapes for the instrument response function and the doublet source profile in order to derive "effective" neutral temperature

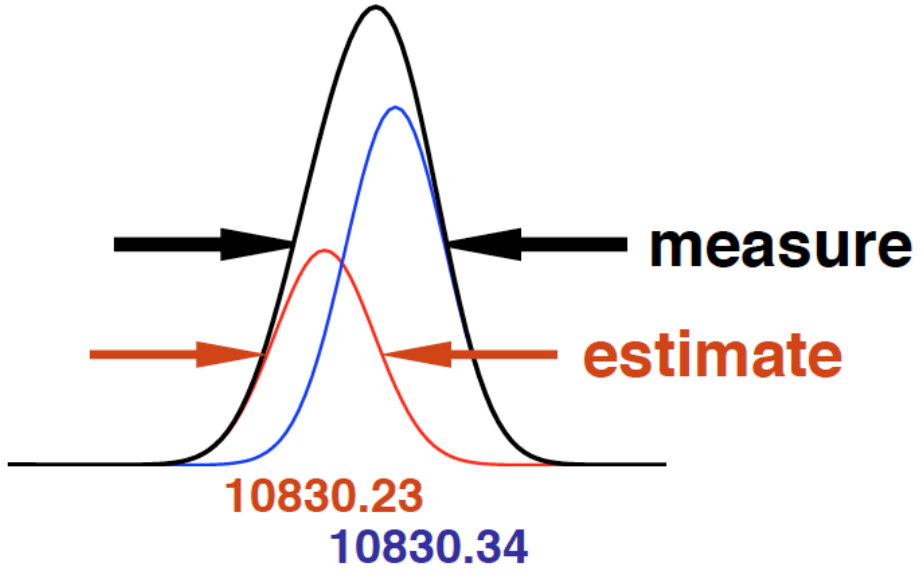

recent work:

- incorporated using Arecibo ISR measurements of [He+] and Ti
- compiled a climatological description of 1083 nm brightness sources

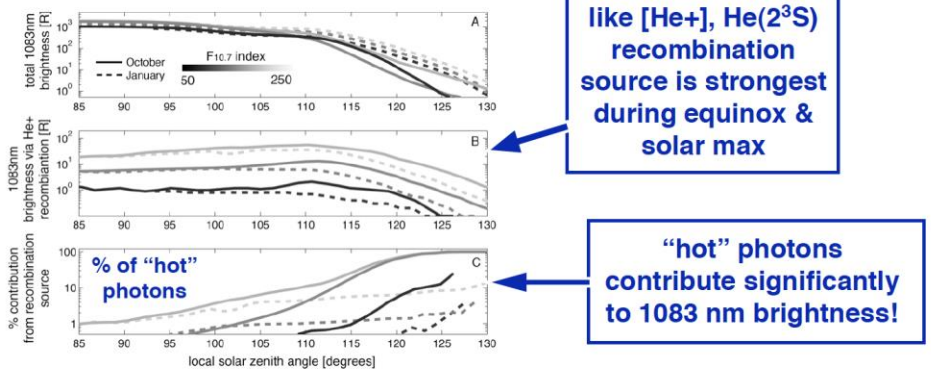

like [He+], He(2^3S) recombination source is strongest during equinox & solar max

"hot" photons contribute significantly to 1083 nm brightness!

Waldrop et al., JGR, 2005

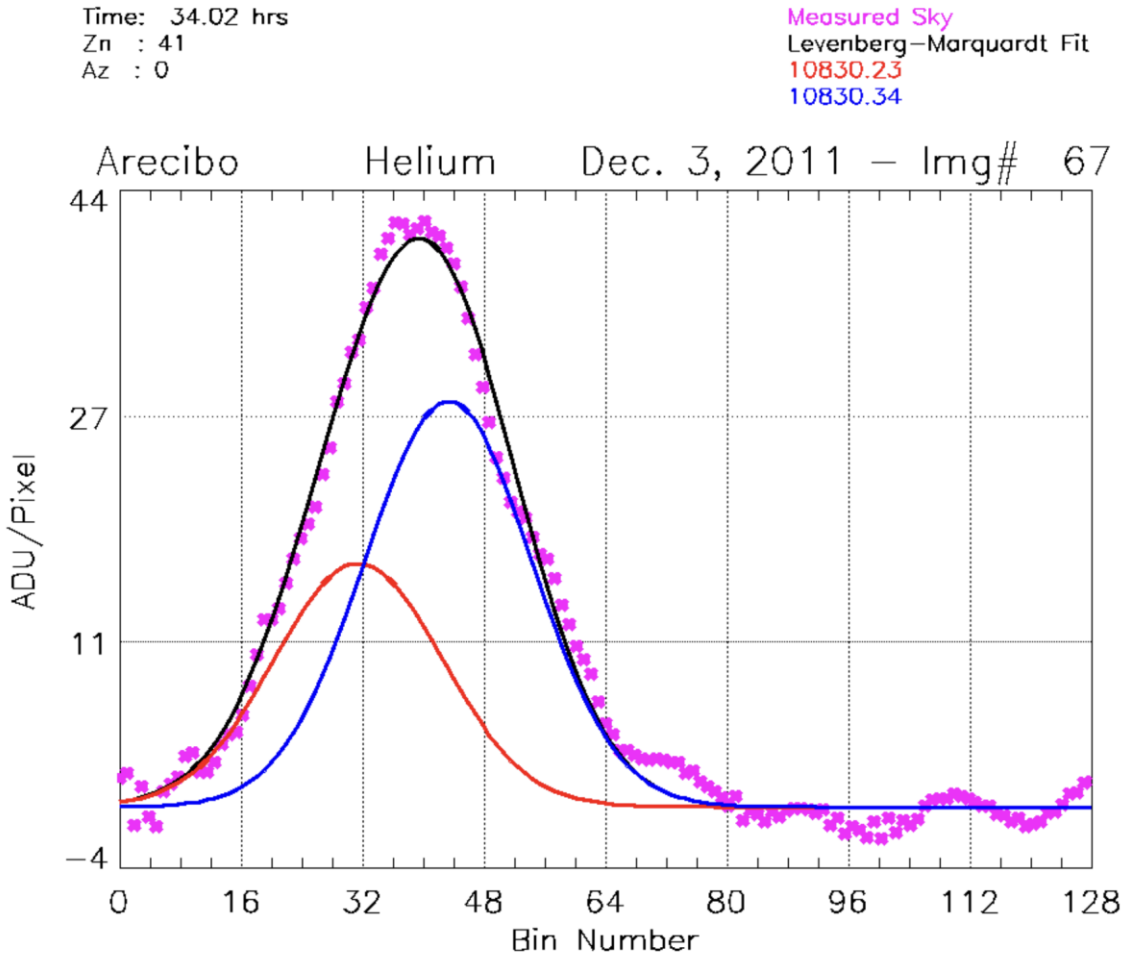

Figure 7. Arecibo FPI 1083 nm spectrum obtained during morning twilight, 3 December 2011. [Kerr, private communication, 2021]. The red and blue curves illustrate the two He triplet components that contribute to the spectral blend observed (pink).

Illustration of the He spectral region observed using a germanium detector.

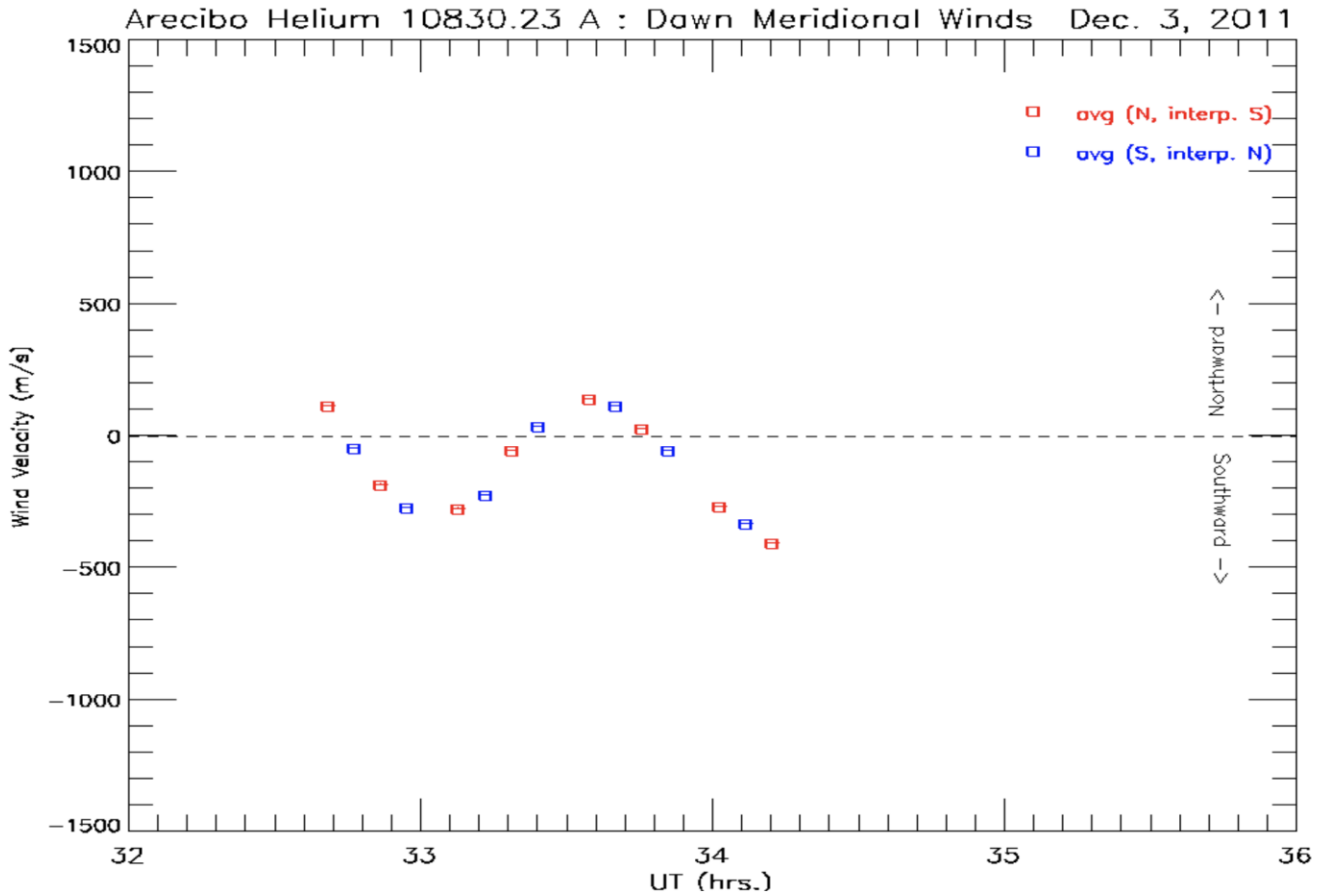

Figure 8. Meridional wind results seen in the morning twilight period of 3 December, 2021 [Kerr, private communication, 2021]. Positive values are northward.

Preliminary results obtained by Kerr (private communication) do suggest fast winds in the exosphere region.

Concluding remarks

• I would argue that more needs to be done re investing in optical technology developments to study the dynamics of the geospace region.

• The application of high resolution interferometry is a powerful way of studying geospace. It is hard to beat a combination that includes winds (dynamics), temperatures, and intensities as the key data products.

• The introduction of short wave infrared (SWIR) detectors in the coming years may well change optical aeronomy in the sense of exploring new environs of the optical spectrum. Imaging the proton and electron auroras may also connect with the imaging of the He aurora. Stay tuned.

EISCAT operates the UHF (left; 931MHz) and the VHF (right; 224MHz) radars at Tromso, Norway since 1981 and 1988, respectively. The UHF radar system was capable for employing the steerable tristatic method using two remote receivers at Kiruna, Sweden and Sodankyla, Finland. However, the remote receiver systems were converted to receive the VHF signal instead of the UHF because of interference from telecommunications. The UHF radar is now operated as the monostatic system.

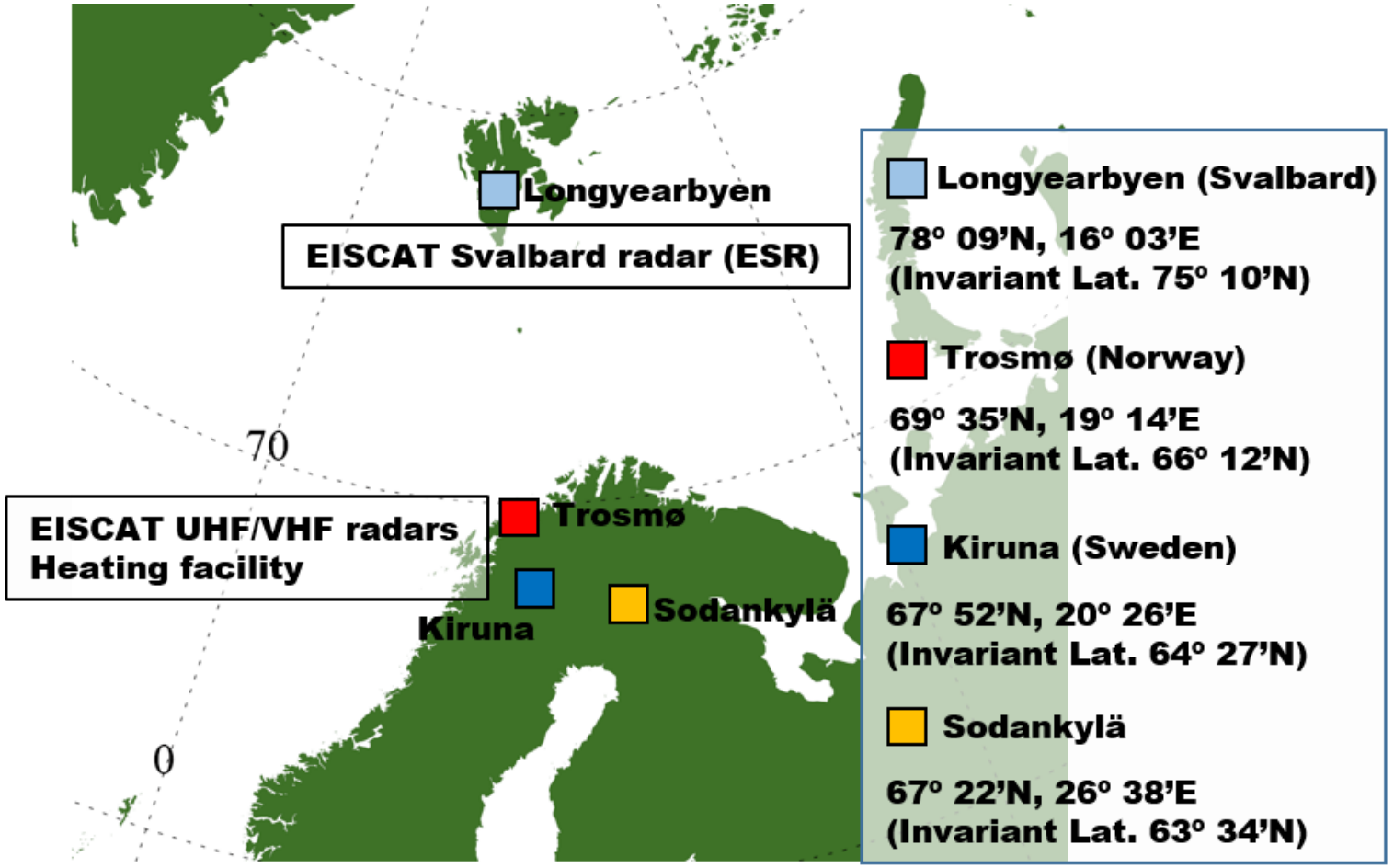

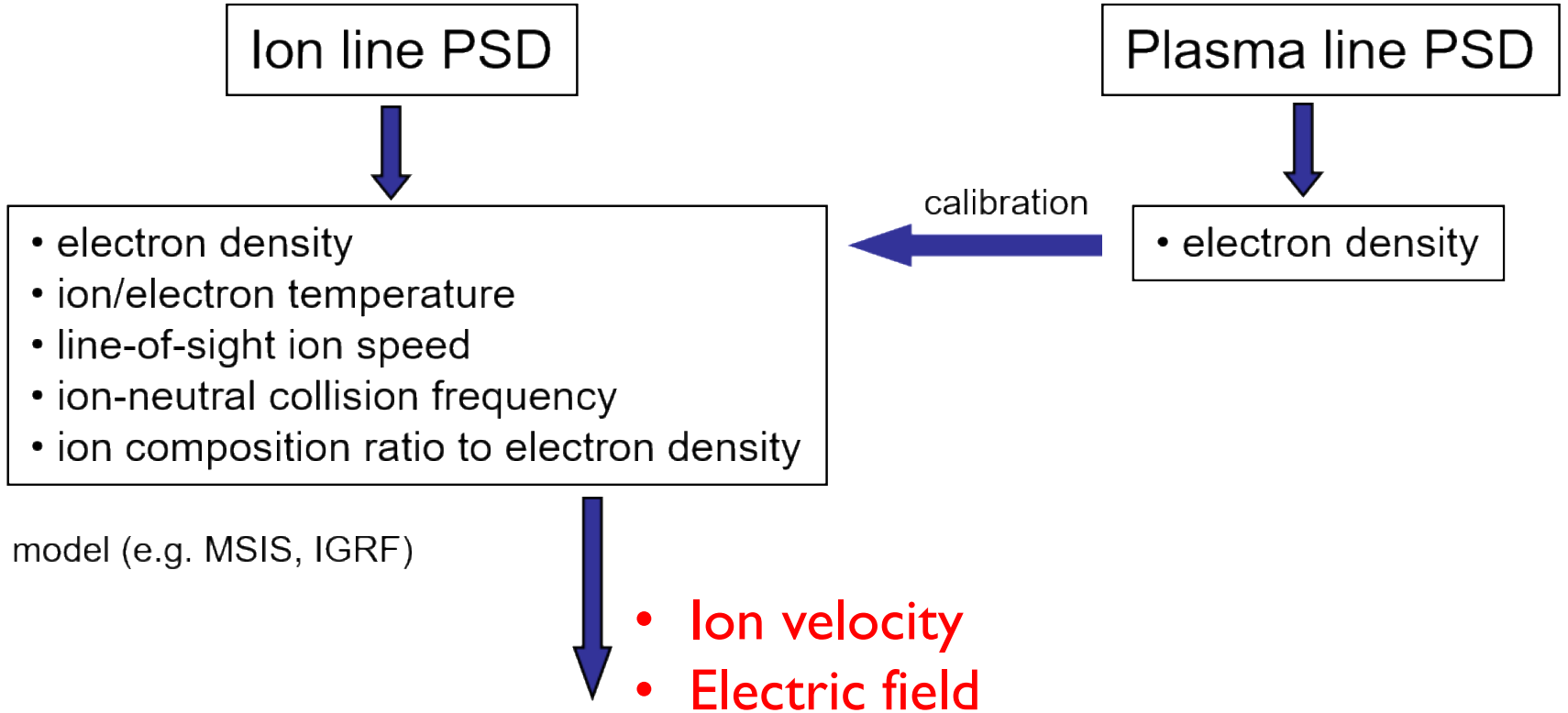

- Ion velocity
- Electric field
- Conductivity
- Ionospheric current
- Joule heating rate
- Particle heating rate
- Neutral temperature

Following slides taken from talk given by Dr. Y. Rinne (2009)

Mesoscale transient flow channels observed in the cusp ionosphere by the EISCAT Svalbard Radar

by

Y. Rinne
J. Moen
H. C. Carlson
K. Oksavik

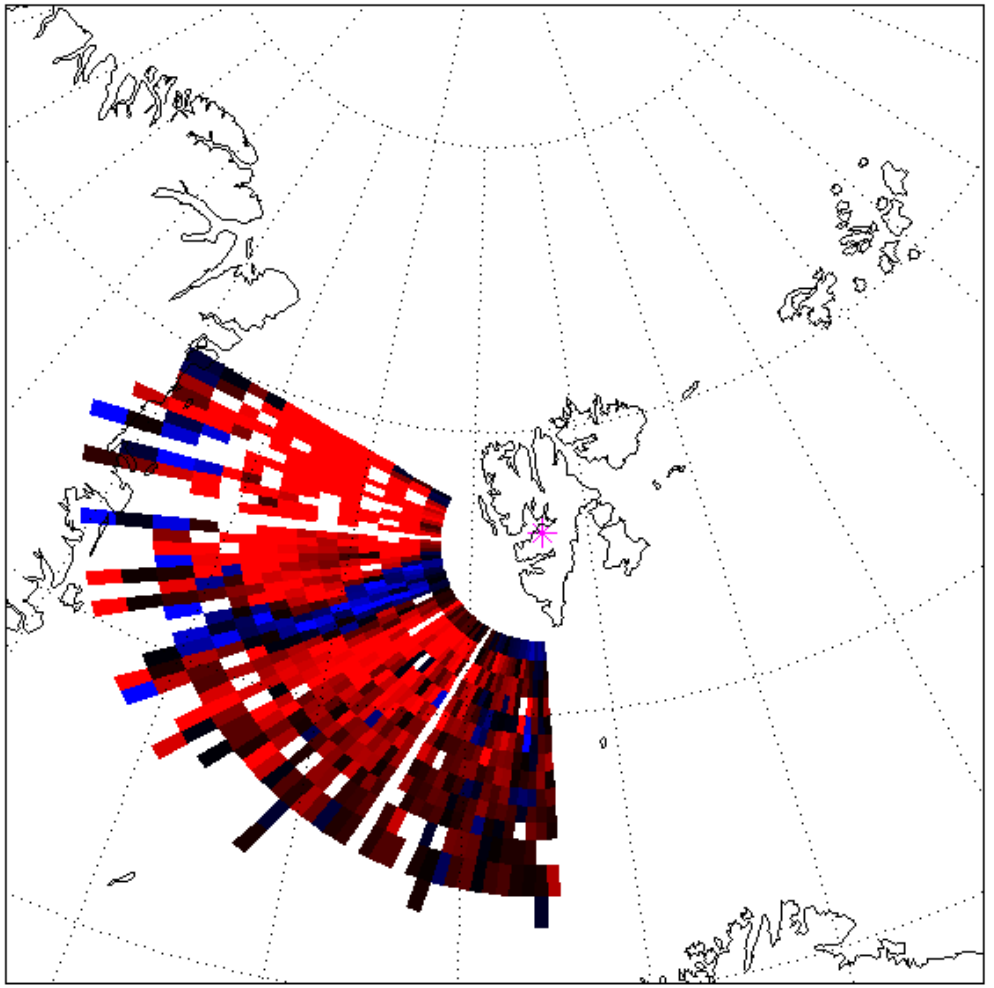

Rinne Definition of Reversed Flow Events (RFEs)

- **A Reversed Flow Event is an elongated segment of enhanced ion flow in the opposite direction of the background flow**
- The RFE has to be evident in more than one radar beam azimuth (this criterion eliminate bad measurements).
- The line-of-sight ion velocity inside the RFE must be greater than |250| m/s for at least one scan.
- The RFE has to have a longitudinal extent of at least 400-600 km in the radar field– of-view.
- The RFE has to stay in clear contrast to the background, i.e. the background flow must exhibit uniform opposite velocities higher than |250| m/s in the area surrounding the RFE.
- The RFE has to be embedded within the background flow for at least one scan (this criterion avoids large-scale convection reversals being detected as RFE).

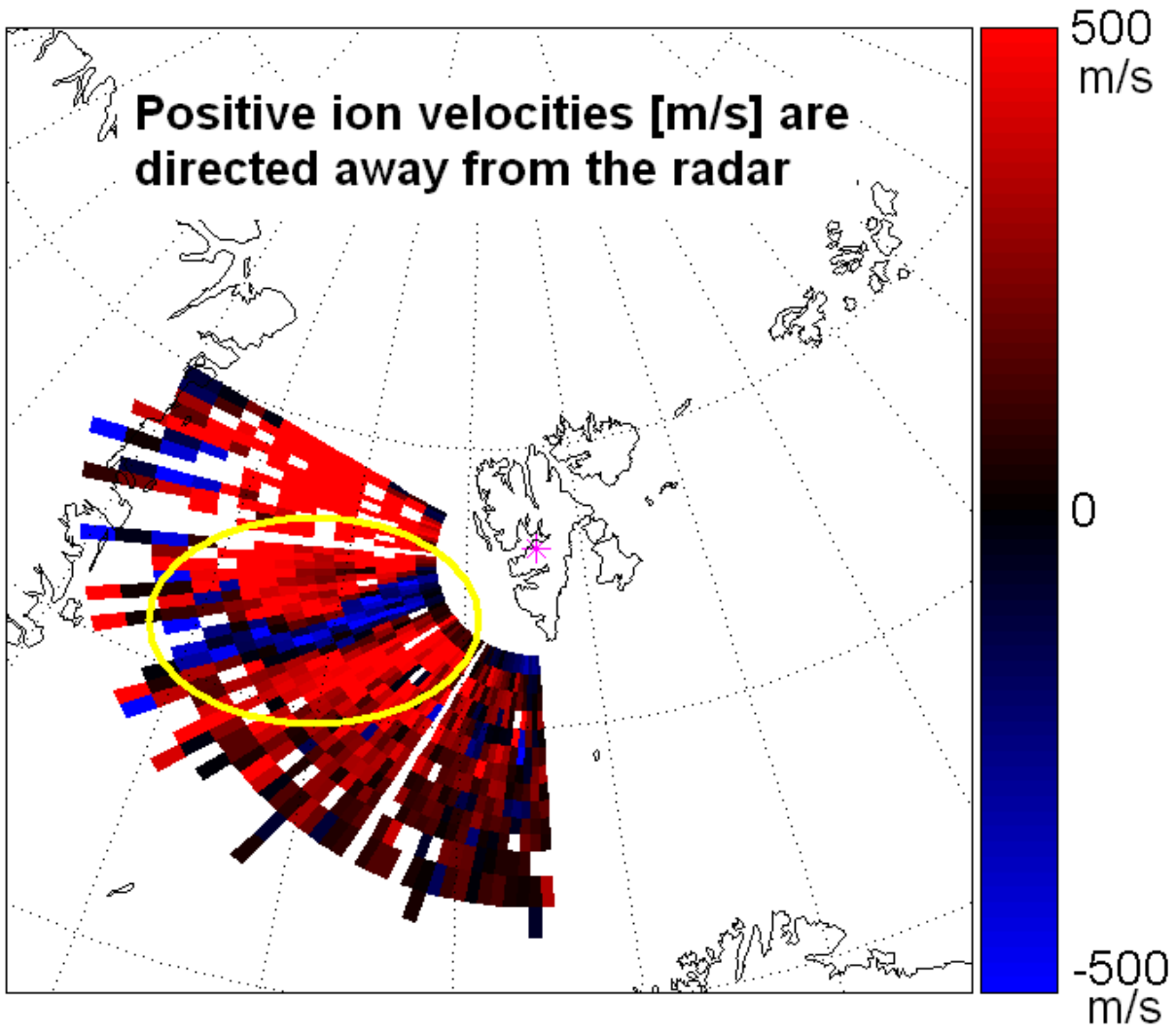

RFE occurrences versus MLT

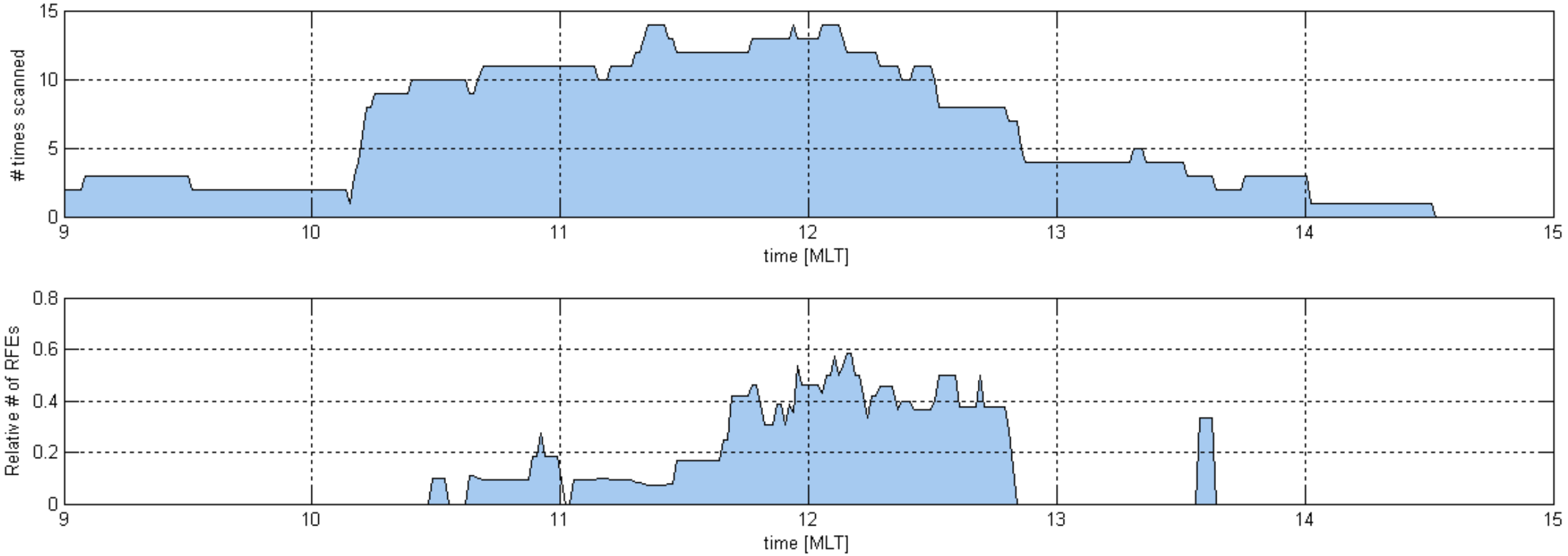

Occurrence of RFEs

- RFEs seen 16% of the time throughout the dataset
- Their average lifetime was 19 minutes
- They exceeded the field of view in length (> 400-600km) and are around 100-200km wide
- No preference was found for the IMF B_z polarity
- It seem as if flow channels are IMF B_y independent

→ RFEs appear to be a regular feature of the active cusp

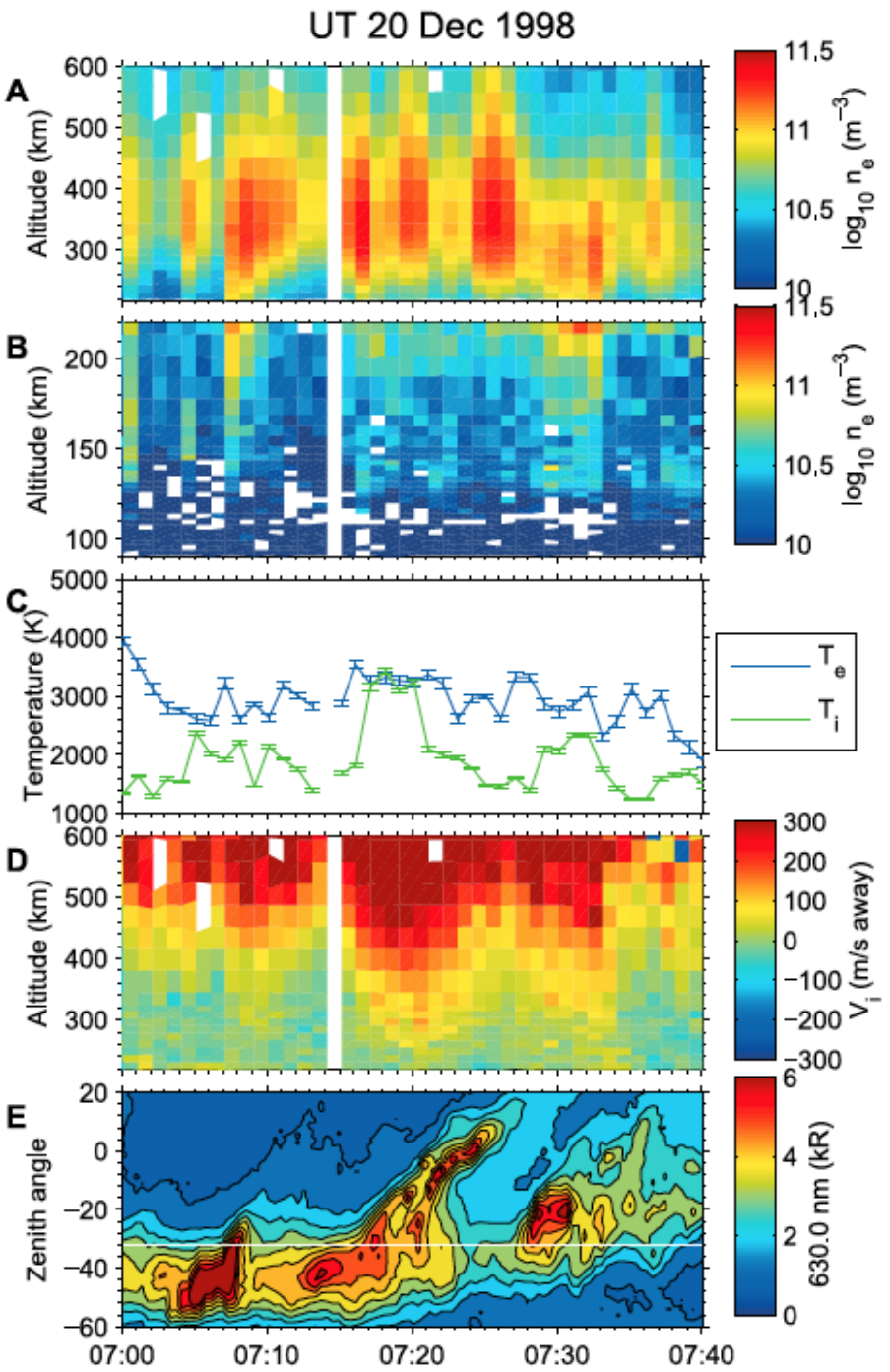

Figure 1. (a–e) EISCAT Svalbard Radar (ESR) observations up the Earth's magnetic field line from 07:00–07:40 20 December 1998 highlighting Electron density profiles [$n_e(h)$] below 200 km in Figure 1b, essential to realistic calculations of height discriminated energy deposition rates. Higher altitude $n_e(h)$ and ion flow up B, ion and electron temperatures at 400 km, and 630.0 nm optical emissions from an MSP (meridian scanning photometer) show three clear magnetic reconnection events. (f) The total ion production rates for 1.0 erg cm^{-3} s^{-1} incident particle flux, for100 eV-10 keV. In the right panel, observed electron density profiles detailing representative enhanced $n_e(h)$ below 200 km during magnetic reconnection events, contrasted with lower bottom-side electron density at 07:13 typical of undisturbed $n_e(h)$ values at this latitude/time.

Carlson et al. 2012

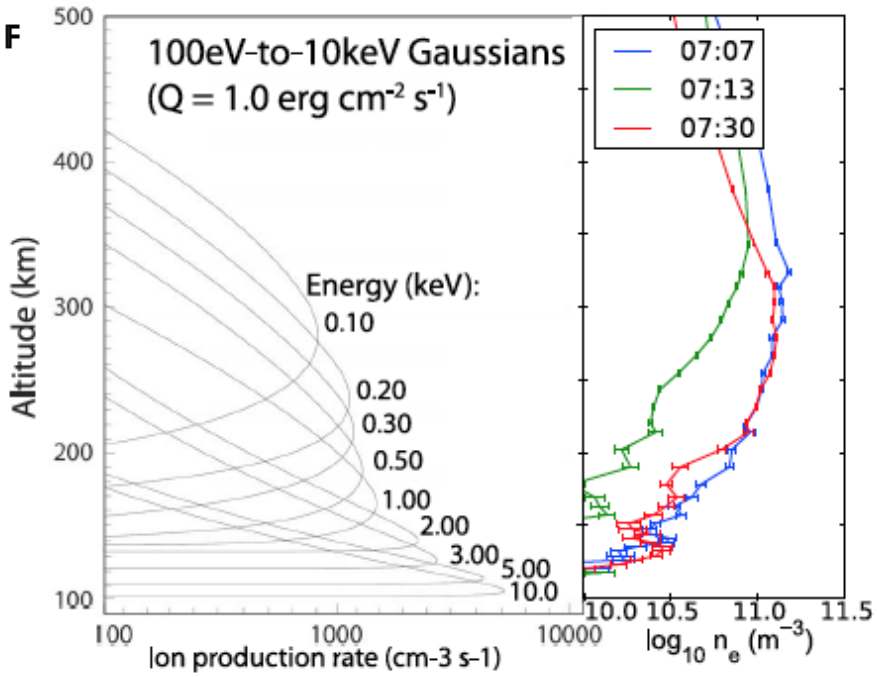

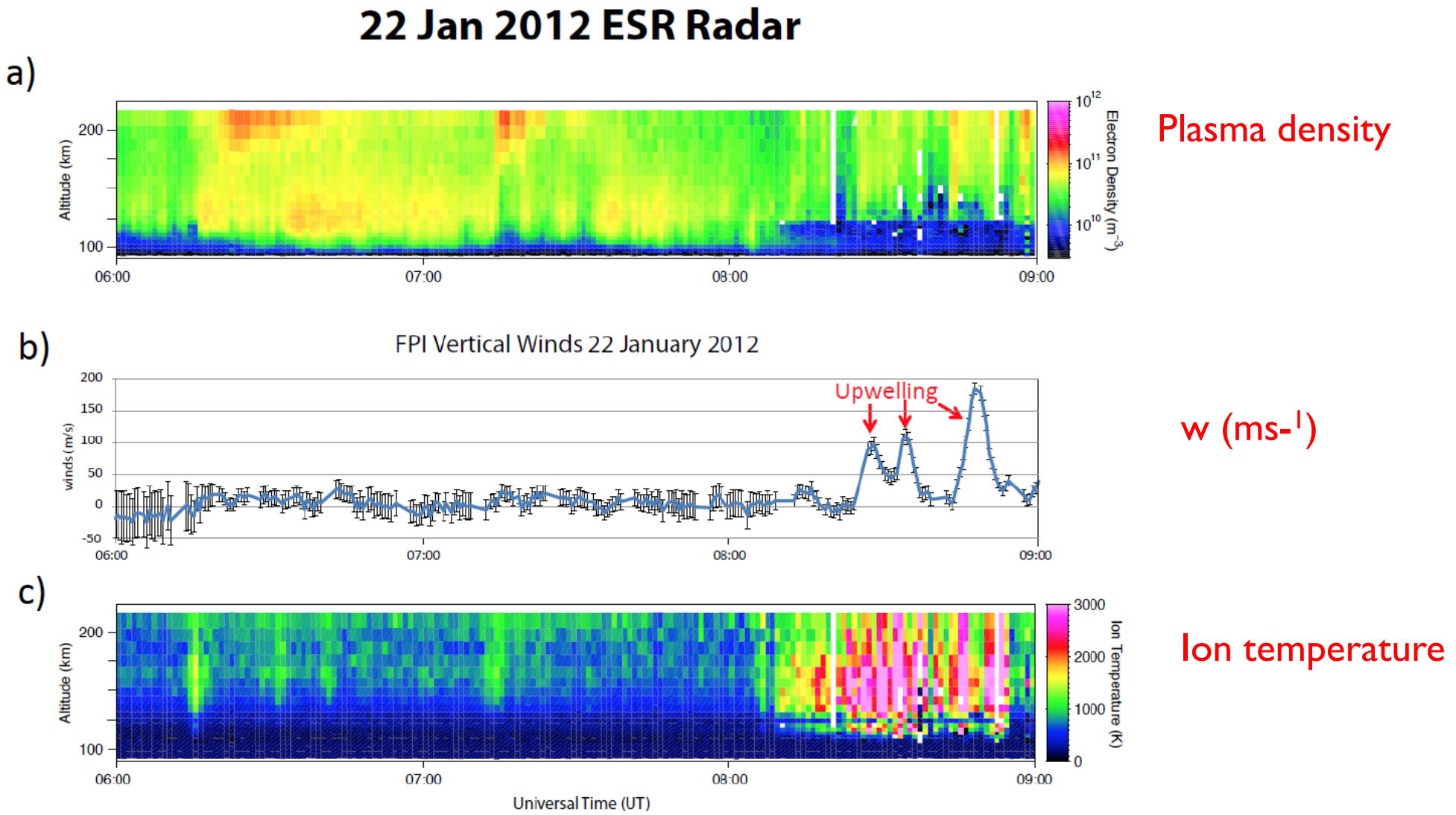

Figure 7 Jan 22, 2012 06:00-09:00 UT Top panel Electron density 100-210 km, Middle panel vertical winds from FPI, Bottom panel Ion Temperature. No upwelling events are seen for either hard or soft particle precipitation events absent flow-jets, but begin immediately upon the first ion frictional-drag ion-heating event (evidenced in *Ti*) near 200 km. These heating events recur in the data as long as the active cusp is overhead. Detailed agreement between observations and predictions is taken as strong evidence for the *Carlson et al.* [2012] mechanism tested here.